UC Berkeley
UC Berkeley Electronic Theses and Dissertations

Title

The role of cofilin-1 and other actin-turnover machinery proteins in glioblastoma cell motility through 3D matrices

Permalink

https://escholarship.org/uc/item/47t224d0

Author

Tran, Vivien Doan-Thanh

Publication Date

2024

Peer reviewed|Thesis/dissertation

eScholarship.org Powered by the California Digital Library
University of California

The Role of Cofilin-1 and Other Actin-Turnover Machinery Proteins in Glioblastoma Cell Motility Through 3D Matrices

By

Vivien Doan-Thanh Tran

A dissertation submitted in partial satisfaction of the

requirements for the degree of

Joint Doctor of Philosophy

with University of California, San Francisco

in

Bioengineering

in the

Graduate Division

of the

University of California, Berkeley

Committee in charge:

Professor Sanjay Kumar, Chair
Professor Matthew Welch
Professor Sophie Dumont

Summer 2024

The Role of Cofilin-1 and Other Actin-Turnover Machinery Proteins in Glioblastoma Cell Motility Through 3D Matrices

Copyright © 2024

By: Vivien Doan-Thanh Tran

Abstract

The Role of Cofilin-1 and Other Actin-Turnover Machinery Proteins in Glioblastoma Cell Motility Through 3D Matrices

By

Vivien Doan-Thanh Tran

Joint Doctor of Philosophy in Bioengineering
with University of California, San Francisco

University of California, Berkeley

Professor Sanjay Kumar, Chair

The actin cytoskeleton plays a major role in driving cell migration. As cells navigate the surrounding matrix, the actin cytoskeleton dynamically adapts and transduces the geometrical cues into phenotype. The resulting cytoskeletal reorganization drives activation of mechanotransductive signals and has been shown to govern many aspects of cell biology. Studies using 2D platforms have produced many insights into the mechanisms of actin dynamics during cell migration, but how these mechanisms and broadly how the actin cytoskeleton contributes to motility through 3D matrices is not well understood. To increase understanding of 3D motility, we utilized an *in vitro* model of glioblastoma (GBM) invasion in engineered hyaluronic acid (HA) matrices to investigate the contributions of actin turnover proteins.

We employed a CRISPR knock-out (KO) screen to examine the contributions of core actin turnover proteins to 2D versus 3D motility. We first quantified cell speed and persistence in random single cell migration on 2D HA and then fold area change and farthest cell traveled of cell spheroids in 3D HA. Surprisingly, we found that only cofilin-1 (CFL) KO had differing effects on 2D versus 3D motility, and that CFL KO enhanced 3D motility. Further investigation revealed that CFL KO uniquely increased both the length and number of actin-based protrusions. With this data, we hypothesized that CFL KO stabilized actin filaments within the protrusions, allowing for better penetration of the surrounding matrix and thus increasing 3D motility.

Through targeted shRNA-induced knock-down (KD) of CFL, we validated the 2D and 3D motility results from the screen. Additional studies with Boyden chamber inserts, PDMS

microchannels, and 2D scatter assays indicated that CFL suppression only enhanced protrusion stability and did not improve other mechanisms of 3D migration. Invasion assays in 3D collagen gels revealed that this effect is seemly HA-specific, as CFL KD cells did not have significantly increased fold area change or farthest cell traveled compared to NT control. Immunofluorescence staining demonstrated that CFL suppression did not alter protrusion architecture and that the protrusions expressed markers reminiscent of microtentacles and filopodia. Collectively, this work highlights the differing contributions of CFL to 2D and 3D motility and points to actin stabilization as a driver of GBM cell motility through HA matrices.

Table of Contents

List of abbreviations ..... **iv**

Acknowledgements ..... **v**

Chapter 1: Introduction **1**

1.1 Thesis overview 1

1.2 Cell motility and the actin cytoskeleton 1

1.3 The cofilin pathway 3

1.4 Glioblastoma 4

Chapter 2: Transduction of cell and matrix geometric cues by the actin cytoskeleton **5**

2.1 Abstract 5

2.2 Introduction 5

2.3 New mechanistic insights from two-dimensional culture systems 6

2.4 Control of cell and matrix geometry in three dimensions 8

2.4.1 Nanotextured surfaces *8*

2.4.2 Microtopographical confinement *10*

Chapter 3: Identifying the contributions of actin-disassembly factors to 3D migration through HA matrices **15**

3.1 Introduction 15

3.2 Results 16

3.2.1 CFL is unique among actin-disassembly factors in driving 3D migration through HA matrices *16*

..... *20*

3.2.2 CFL KO drives 3D motility by favoring greater actin polymerization and stability in cellular protrusions. *20*

..... 22

3.3 Discussion and conclusions 22

3.4 Methods 23

3.5 Acknowledgements 27

Chapter 4: Suppression of cofilin-1 increases migration speed of GBM cells through 3D HA matrices 28

4.1 Introduction 28

4.2 Results 29

4.2.1 CFL KD confirms 2D motility phenotype from CRISPR screen 29

4.2.2 CFL KD accelerates 3D motility through HA matrices 29

4.2.3 Deconstruction of CFL contributions to 3D invasion 31

4.2.4 Protrusions contain markers of microtentacles and filopodia irrespective of CFL status 35

4.3 Discussion and conclusions 36

4.4 Methods 39

4.5 Acknowledgements 43

Chapter 5: Conclusions 44

5.1 Summary 44

5.2 How do the actin turnover proteins contribute to 3D migration in HA matrices? 45

5.3 What are the contributions of CFL to 3D GBM motility? 47

Chapter 6: References 49

Appendix A – Supplementary Information for Chapter 3 and 4 66

List of Figures

Figure 1.1. Diagram of the cell motility cycle. 2
Figure 1.2. Overview of core actin turnover proteins. 3
Figure 1.3. A schematic of the cofilin activity cycle 3
Figure 1.4. A diagram of GBM parenchymal and perivascular invasion. 4
Figure 2.1. Mechanisms of cell sensing of 2D substrate geometric cues. 9
Figure 2.2. Effects of 3D geometry on cytoskeletal organization and cell behavior. 13
Figure 3.1. Random single cell motility of CRISPR KO cells on 2D HA-RGD gels. 18
Figure 3.2. 3D spheroid invasion assay of CRISPR KO cells in 3D HA gels. 20
Figure 3.3. 3D protrusion formation assay of CRISPR KO cells in HA gels 22
Figure 4.1. Validation of CFL KO results with shRNA KD in 2D. 31
Figure 4.2. Validation of CFL KO results with shRNA KD in 3D. 32
Figure 4.3. Contextualizing the effects of CFL KD on aspects of 3D motility 35
Figure 4.4. Cells in the HA matrices display F-actin-based protrusions with both McTN and filopodial markers. 38
Figure 5.1. What role does actin turnover play in 3D (GBM) motility? 44
Supplemental Table A1 66
Supplemental Table A2 70

List of abbreviations

2D	two dimensional
3D	three dimensional
CAP	Srv2/cyclase-associated protein 1
CFL	cofilin-1
CRISPR	clustered regularly interspaced short palindromic repeats
ECM	extracellular matrix
GBM	glioblastoma
GSN	gelsolin
HA	hyaluronic acid
HA-only	HA matrix without RGD motifs
HA-RGD	HA matrix with RGD motifs
KD	knockdown
KO	knockout
LIMK	LIM kinase
McTNs	microtentacles
MMPs	matrix-metalloproteases
MyoX	myosin 10
NC	non-coding
NT	non-targeting
PFN	profilin-1
RGD	Arg-Gly-Asp
sgRNA	single-guide RNA
shRNA	short hairpin RNA
TWF	twinfilin-1
WDR	actin-interacting protein 1 /WD repeat protein 1

Acknowledgements

I am abundantly grateful for all the wonderful people who have supported me throughout my Ph.D. Their support, both technical and personal, have been invaluable and have made this journey considerably smoother.

First and foremost, I would like to thank my advisor, Sanjay Kumar. I owe a lot of my development as a scientist to his mentorship and expertise. His thoughtful discussions during our many meetings left me with many great ideas and motivation to tackle the next steps in my project. He has given me the room and resources to learn and grow as an independent scientist. His encouragement while I was tackling intimidating tasks, such as writing a manuscript, crafting a podium talk for a conference, and putting together my qualifying exam proposal, was immensely validating and helped me hone my skills. I have enjoyed working with Sanjay and want to express my gratitude for his mentorship.

I would like to acknowledge the members of my qualifying exam and dissertation committees – Professor Tejal Desai, Professor Mohammad Mofrad, Professor Lydia Sohn, Professor Matt Welch, and Professor Sophie Dumont. Their expertise and feedback have been helpful in improving my projects and ideas and I am grateful for all of their scientific discussions with me. I would also like to thank Professor Terry Johnson for coaching me on how to teach as a graduate student instructor. His exceptional teaching was wonderful to watch and learn from and has given me invaluable tools for my endeavors in mentoring and teaching. I appreciate the time that each of these professors have invested in helping me and am grateful to have been able to work with such brilliant people.

Furthermore, I have had the greatest honor of working with an exceptional group of people in the Kumar Lab. Their camaraderie has made even the longest days in lab bearable and has brightened every day that I have worked here. I would like to express my deep appreciation to the past members of the lab for their mentorship (Joe Chen, Jason Coombes, Phil Kang, Stacey Lee, Kayla Wolf, Ruoxing Lei, Jieung Baek, Andy Lopez, Junghwa Cha, Cam Morley, and Eric Qiao) and present members for their support (Erin Akins, Emily Carvahlo, Kwasi Amofa, Erika Ding, Anna Weldy, Kahmina Ford, Camille Fulmore, Lu Ling, Dana Wilkins, Dee Cruz- Garcia, and Julio Bernal-Chanchavac). I will especially highlight the Fab Four – Erin Akins, Emily Carvahlo, and Kwasi Amofa – for being on this journey with me from year 1. I have also had the honor of mentoring 2 excellent rotation students (Kahmina Ford and Yvonne Rong) and 2 wonderful undergraduate students (Francisco Zamora and Miles Duong). Thank you especially to Katherine Patterson, who has been an extraordinary lab manager. I am grateful for the work she does in keeping the lab running and all of the members safe. I could not ask for a better group of people to work with during this Ph.D. journey.

I would like thank all the friends I have made in the UC Berkeley/UCSF Graduate Program in Bioengineering for creating an incredible community and a support structure to help me push through all of the bumps in this journey. This community is what drew me to do my Ph.D. here and 6 years later, it has been a highlight of my time here. I am especially thankful for the close friends I have made in the program – Aniket Tolpadi, Amanda Merriwether, Maria Diaz de Leon Derby, Kwasi Amofa, and Preethi Raghavan. The camping trips, ski trips, and adventures throughout the Bay Area provided welcome distractions from the Ph.D. grind and kept me grounded. I have explored so much and laughed so hard because of them, and I am forever grateful to have met them. A big thanks to my roommates during my Ph.D. – Chloe McCollum and Madison Lehmer. Living with them has been such a joy and a delightful respite from work. Their company and conversations, especially during the pandemic, ensured I always had an ear to listen to my troubles and had a plethora of crafts to work on. Thank you all so much for your friendship.

To my partner Justin Zhong – I feel very fortunate to be on this Ph.D. journey with you. While tackling a Ph.D. at the same time has its struggles, your constant support and understanding have been invaluable. Thank you for encouraging me through the tough times and celebrating my successes with me. I am excited to see you finish your Ph.D. journey and look forward to the years together to come.

Last, but not least, I want to express my endless gratitude to my family. As Vietnamese refugees, they rebuilt their lives in a foreign land and have succeeded in creating a home for following generations to flourish. I am deeply indebted to their sacrifices and hard work and I am proud to be the child of refugees. I will continue to the carry the strength of my family and culture with me. I first wish to thank my extended family, who have always expressed support and care for me, even though I don't see them frequently. I especially would like to express my gratitude to my late great-grandfather, my Ông Cố, who relentlessly championed education and learning and encouraged everyone to pursue the highest degree they could. This spirit has stayed with me and has inspired me to always continue learning. I miss him, Bà Cố and my grandparents dearly. Thank you to my parents for always being there for me and for keeping me grounded. My parents have given me so much unconditional love and support. They have always pushed me academically and motivated me to follow my passions. Their encouragement is what has it possible for me to pursue this Ph.D. To my brother Vincent – thank you for being a constant companion. We sometimes are two dum-dums in a pod and other times two smart engineers. I am forever grateful to have someone that is always in my corner. To my family - I love you all and dedicate my Ph.D. to you.

I have been supported by so many wonderful people throughout this journey. Thank you for making this Ph.D. possible.

Chapter 1: Introduction

1.1 Thesis overview

This thesis aims to deepen our understanding of the contributions of the actin turnover machinery to glioblastoma (GBM) cell motility through HA matrices. Using *in vitro* platforms that mimic tissue geometries, we investigate how the contributions of these proteins differ between two-dimensional (2D) and three-dimensional (3D) motility and further dissect the mechanisms, thereby contributing to the broader pool of knowledge of how cells navigate tissue-mimetic geometries and matrices.

Chapter 1 will serve as a basic introduction to GBM and the cell motility machinery that will be investigated in this thesis. Chapter 2 provides background on how the actin cytoskeleton integrates cell and matrix geometric cues with a literature review. Next, chapter 3 examines the contributions of core proteins in the actin turnover machinery with a CRISPR screen. We identified that suppression of the actin-severing protein cofilin-1 (CFL) resulted in faster cell motility through 3D hyaluronic acid (HA) matrices but not on 2D HA. We also found that CFL suppression uniquely increases both the length and number of F-actin-positive cellular protrusions. With the findings from the screen, we proposed that CFL suppression stabilizes F-actin within the cellular protrusions, allowing cells to penetrate the surrounding matrix and thus facilitating invasion. Chapter 4 is a follow-up study that further dissects the contributions of CFL suppression to 3D GBM motility and suggests that the effects of CFL suppression is mostly through stabilization of protrusions, rather than through additional mechanisms.

1.2 Cell motility and the actin cytoskeleton

Cell migration plays an important role in many normal biological processes that include wound healing and embryogenesis. Defects in cell migration also play a large role in the progression of many diseases, such as cancer or immune system dysfunction. For example, cancer invasion and metastasis involve uncontrolled cell migration [1–3]. Cell motility is a complex process requiring coordinated action of many molecular components, driven by the actin cytoskeleton [3,4]. Actin, one of the most abundant proteins in eukaryotic cells, is organized into intricate networks that dynamically cycle as monomeric G-actin into and out of filamentous F-actin [5]. This reorganization is tightly regulated by signaling networks, of which the key components are the Rho-family GTPases (Rho, Rac, Cdc42) [6]. The Rho-family GTPases act through their effectors drive cellular responses to external cues, orchestrating cellular protrusion, contraction, and adhesion during migration. Broadly, Rac and Cdc42 stimulate actin polymerization to respectively form and stabilize lamellipodia and filopodia while Rho drives the assembly

and contraction of actomyosin bundles that provide the traction force for forward movement [7,8].

Many cells migrate via an adhesion-dependent mode of motility, broadly classified as mesenchymal [9]. This migration mode consists of a cycle where the cell first establishes a leading edge, where the assembly of F-actin filaments provides the protrusive force to push the leading edge forward and establish front-back polarity of the cell [10] (Figure 1.1A). Next, tension builds at the rear of the cell through actomyosin filaments and is subsequently released by disengaging the adhesions at the rear of the cell, retracting the trailing edge (Figure 1.1B). Filaments at the rear of the cell are disassembled and the monomers are recycled for polymerization [11]. This cycle of protrusive forward motion followed by trailing edge retraction is repeated in directional migration (Figure 1.1C) [1]. This complex process involves many actin-binding proteins, which facilitate and regulate the rate and location which assembly and disassembly occur. The activities of these proteins are dictated by extracellular cues through signaling pathways from the Rho-family GTPases as cells interact with the surrounding ECM [7].

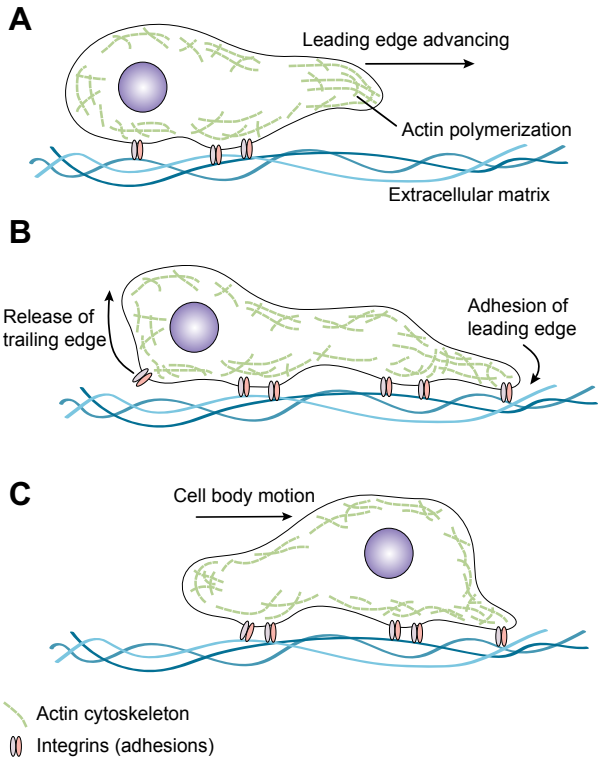


Figure 1.1. Diagram of the cell motility cycle. (A) Actin polymerizes at the front of the cell, pushing the leading edge forward. (B) Adhesions form at the leading edge, providing traction force for forward motion. The adhesions at the trailing edge release and the filaments in the back of the cell are dissembled. (C) The cell retracts its trailing edge, resulting in forward motion of the cell body. This cycle repeats as the cell undergoes directional motility.

The turnover of actin networks broadly follows a pathway of 1) capping filament growth, 2) filament remodeling, 3) filament severing, 4) filament depolymerization, and 5) monomer recycling and new filament assembly [12]. A core group of proteins are responsible for regulating the turnover of actin filaments, each playing a role in one or more roles in the pathway. These ubiquitous factors – cofilin (CFL), profilin (PFN), twinfilin (TWF), gelsolin (GSN), Srv2/cyclase-associated protein (CAP), and actin-interacting protein 1 /WD repeat protein 1 (WDR) - catalyze actin turnover to either maintain the actin network or deconstruct filaments within a retracting protrusion [12–14]. CFL severs and depolymerizes actin filaments (discussed in further detail in the next section) while CAP

and WDR both enhance CFL-mediated actin severing [15–17]. PFN1 promotes actin polymerization by recycling monomers for new filaments, TWF1 and GSN caps actin filaments and accelerates actin depolymerization, and GSN also severs filaments (Figure 1.2) [14,18,19].

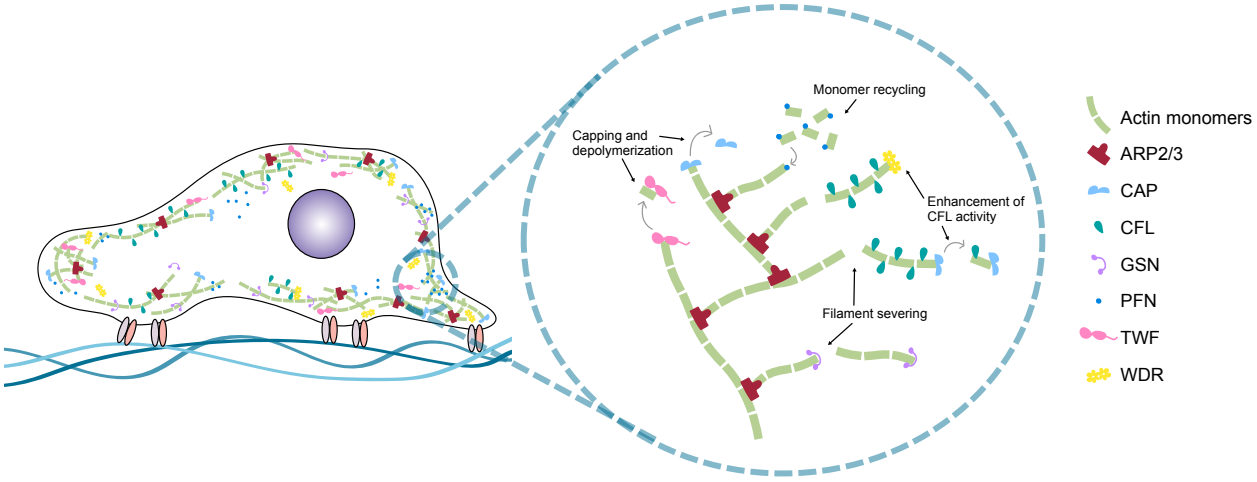


Figure 1.2. Overview of core actin turnover proteins.
A diagram showing the roles of the core proteins involved in actin filament turnover. TWF and CAP are involved in capping and accelerating depolymerization of filaments. PFN recycles monomers for filament polymerization. WDR and CAP enhance CFL activity. CFL and GSN sever actin filaments and accelerate filament depolymerization.

1.3 The cofilin pathway

The cofilin (CFL) pathway serves as one of the major regulators of the actin cytoskeleton [20,21]. The primary role of CFL is to facilitate rapid F-actin turnover by severing F-actin filaments, leading to creation of free barbed ends for sites of nucleation for actin polymerization, defining the leading edge and direction of cell motility [20,22]. Cut filaments also can depolymerize, recycling monomers for new filaments [23]. CFL is locally activated at the leading edge of cells through pH-dependent hydrolysis from binding partners at the cell membrane [24]. It is inactivated in the cytosol via phosphorylation by LIM domain kinase (LIMK) and testicular protein kinase (TESK) and reactivated through dephosphorylation by chronophin (CIN) and slingshot (SSH) (Figure 1.3) [25–28].

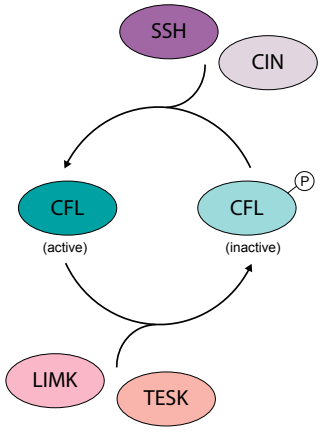


Figure 1.3. A schematic of the cofilin activity cycle.

1.4 Glioblastoma

Glioblastoma (GBM), one of the most lethal and primary malignant brain tumors, has a median survival time of 14 months, even with treatment [29,30]. GBM is characterized by rapid and diffusive cellular invasion of brain tissue, which lends resistance to traditional therapies such as chemotherapy and radiotherapy [31]. The diffuse invasion of tumor cells also makes complete surgical resection impossible, leading to inevitable recurrence [32,33]. Despite medical advances and intensive research, the median survival time of GBM has not increased dramatically over the past years [34]. Understanding the mechanisms of how GBM infiltrates into healthy brain tissue will deepen the knowledge of GBM pathogenesis and provide insight for future therapies.

The spread of GBM involves multiple and complex routes of invasion through the dense brain ECM. One such route starts with the slower infiltration through the parenchyma in a 3D mode of motility. Once the cells reach the perivascular niche, they switch to a more rapid, 2D-like mode of motility (Figure 1.4) [35,36]. To be able to switch migration modes and adapt to the varying geometries within the brain ECM, the cells must dynamically reorganize their actin cytoskeleton [3]. However, the specific mechanisms that GBM cells use to reorganize their actin cytoskeleton remains unclear [37–39]. Analyses of patient tumor genomics datasets such as REMBRANDT show that many genes involved in cell motility are misregulated or altered in GBM, including proteins involved in actin filament turnover [38,40].

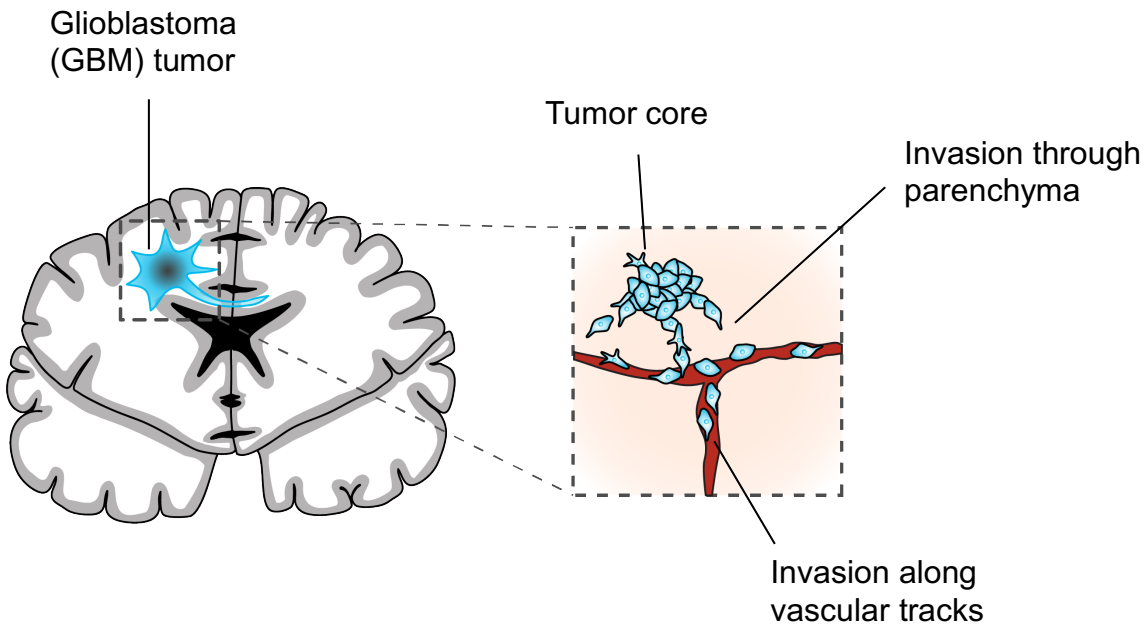


Figure 1.4. A diagram of GBM parenchymal and perivascular invasion.
GBM tumor cells utilize many routes of invasion to infiltrate healthy brain tissue; pictured here are 2 common routes of invasion. From the tumor core, cells first invade through the dense parenchymal matrix. Once the cells reach the vascular tracks, they adopt more rapid, 2D-like mode of motility.

Chapter 2: Transduction of cell and matrix geometric cues by the actin cytoskeleton

Parts of this chapter are excerpted with permission from Elsevier Ltd. from the article "Transduction of cell and matrix geometric cues by the actin cytoskeleton" by Vivien D. Tran and Sanjay Kumar in *Current Opinion in Cell Biology* 68, 61-71 (2021).

Copyright © 2021, Elsevier Ltd.

2.1 Abstract

Engineered culture substrates have proven invaluable for investigating the role of cell and extracellular matrix geometry in governing cell behavior [41–43]. While the mechanisms relating geometry to phenotype are complex, it is clear that the actin cytoskeleton plays a key role in integrating geometric inputs and transducing these cues into intracellular signals that drive downstream biology. Here we review recent progress in elucidating the role of the cell and matrix geometry in regulating actin cytoskeletal architecture and mechanics. We address new developments in traditional two-dimensional culture paradigms and discuss efforts to extend these advances to three-dimensional systems, ranging from nanotextured surfaces to microtopographical systems (e.g. channels) to fully three-dimensional matrices.

2.2 Introduction

Cells in tissue reside within a complex niche containing many components, including other cells and the surrounding extracellular matrix (ECM). The ECM biophysically instructs cell behavior through its 3D structure, mechanics, and geometric placement of adhesive sites. The resulting constraint on cell shape regulates a wide variety of processes, including proliferation and differentiation [44–46], as well as morphogenetic processes in development, wound healing, and disease [47–49]. Engineered ECM substrates have long been recognized as a powerful experimental paradigm for controlling cell shape and investigating shape-dependent phenomena, starting with the retrofitting of electron microscopy grids in the 1960s, continuing to microcontact printing in the 1990s, and progressing to today's sophisticated surface engineering technologies capable of controlling ECM geometry at the nanoscale [41–43]. Although the biological and technical details of these studies have varied widely, a remarkably common theme is the essential role of the cellular cytoskeleton – particularly the actin cytoskeleton – in transducing geometric cues into phenotype, with changes in cytoskeletal organization and mechanics driving activation of mechanotransductive signals that have been shown to influence nearly every aspect of cell biology [50–53].

In this chapter, we briefly highlight a selection of recent studies that have deepened the field's understanding of the relationships between cell/ECM geometry, actin cytoskeletal structure and mechanics, and the cell phenotypes that lie downstream. First, we discuss recent studies that have used 2D micropatterning to create new mechanistic insight into the role of the actin cytoskeleton in governing shape-dependent biology. Next, we cover efforts to extend these patterning technologies to three dimensions [54,55], starting with the introduction of micro- and nanotextured surfaces to create 3D architectures within 2D topologies, including the increasing use of microchannels to simulate tissue confinement. Finally, we discuss efforts to extend geometric control to "true" 3D environments in which cells are fully encapsulated within a 3D network such as a polymer hydrogel [54,56].

2.3 New mechanistic insights from two-dimensional culture systems

There is a rich tradition within cell biology of using single-cell micropatterning to control cell shape in 2D culture. Although single-cell patterning is sometimes viewed as a relatively recent innovation, the concept dates back to at least 1967, when electron microscopy grids were repurposed to constrain single hepatocytes within "haptotactic islands." In some cases, hepatocytes spread to adopt the geometry of the island, whereas in others, cells were observed to migrate and divide, offering the opportunity to track clonal populations [41]. Even this early study did not overlook the power of micropatterning to facilitate parallelization and standardization, with the author noting the ability to track more cells over longer periods of time than traditional time-lapse approaches. Two decades later, alkanethiol-based microcontact printing was famously applied to produce cell-sized ECM islands to constrain spreading, leading to the seminal observation that cells can be switched between proliferative and apoptotic programs by controlling spread area [46,57]. More recently, cell shape has been used to control stem cell differentiation, with lineage trajectories depending on seemingly minuscule details such as whether the cell perimeter consists of convex or concave segments [50,58].

A common and consistent theme throughout a large subset of these studies is the central role played by the cytoskeleton in sensing and integrating geometric cues, with shape-induced changes in actin cytoskeletal structure in particular altering front-back polarity, traction force generation, and placement of lamellipodia and other adhesive processes [51,52,59]. Recently, new mechanistic insight into this regulatory relationship has been gained by the integration of micropatterning approaches with other single-cell biophysical tools to more precisely dissect molecular and physical mechanisms through which adhesive geometry and cell shape regulate cytoskeletal organization and mechanics. As one example, we recently combined single-cell micropatterning, subcellular laser ablation, and mathematical modeling to investigate how actomyosin stress fiber (SF) viscoelastic properties depend on SF length. Here, micropatterning enabled us to standardize cell shape while also prescribing the location and length of specific SFs by

compelling fibers to form across defined gaps in the ECM. We then measured SF viscoelastic properties by laser-severing individual SFs and tracking fiber retraction. We found that the elastic energy stored by a SF depends not only on its length but also the degree to which the fiber is physically networked to other SFs in the cell. Our experimental measurements could be accurately predicted by a computational model depicting the SF network as connected elastic cables [60]. In a subsequent study, we combined single-cell micropatterning and laser ablation to measure viscoelastic properties of specific SF subtypes found in polarized, migratory cells (dorsal SFs, transverse arcs, ventral SFs). The use of crossbow patterns produced cells with standardized morphologies with clear front-back polarity and a tight range of SF lengths. We found that dorsal fibers bear little to no intrinsic prestress and that ventral SF mechanics depend on the mechanism through which these fibers are assembled. Specifically, when ventral SFs formed through the fusion of dorsal SFs and transverse arcs, they incorporated actin crosslinkers that function as "brakes" to increase viscous drag during retraction. This viscous drag fell significantly when ventral SFs assembled de novo from smaller actomyosin subunits, such as when cells were cultured on microlines that are too narrow to support arc assembly [61].

2D micropatterns have also been used to study the effects of geometric constraints on actin organization and dynamics during cell spreading and migration. In several past studies, cells had been observed to respond to cell-scale curvature in the extracellular environment by forming protrusions at positive curvatures and actin cables at negative curvatures [62–64]. However, it had remained unclear whether or how these principles operated at a larger, multicellular length scale. A recent study addressed this question using geometrically defined wound-closure assays and multicellular flower-shaped patterns. Notably, multicellular structures adapted their actin flow according to the sign of curvature encountered. Whereas convex curvatures promoted standard retrograde flow of actin, concave curvatures promoted an anterograde flow of actin towards the leading edge, culminating in the assembly of SFs that span nonadhesive regions and enable cells to spread across regions that lack underlying matrix [65]. In complementary work also aimed at understanding how cells spread across non-adhesive substrates, we used micropatterned rectangular frames to create defined spreading trajectories reminiscent of how cells engage 3D collagen fibers. The spreading path was found to depend both on the geometry of the pattern and the initial cell adhesive position. As cells spread, they assembled SFs that ran parallel to the leading edge and bridged non-adhesive area of the pattern. Since the trajectory of the leading edge was dependent on the initial cell adhesive position, the final arrangement of SFs in the spread cell reflected its spreading trajectory and encoded a sort of history or memory [66].

2.4 Control of cell and matrix geometry in three dimensions

While much continues to be learned from traditional 2D patterning strategies, a major acknowledged goal in the field is to define cell and matrix geometry in three dimensions, a topology that is much more representative of many tissues. The addition of a third dimension enables culture platforms to more closely mimic features of living tissue [55]. We now discuss efforts to extend geometric regulation of cell behavior in 3D, progressing from 2D nanotextured and microtopographical substrates to "true" 3D matrix environments in which cells are fully embedded within ECM.

2.4.1 Nanotextured surfaces

At the molecular scale, cells encounter many ECM components as three-dimensional, nanoscale structures, such as collagen fibers and fibronectin fibrils. Although these structures are much smaller than the cell, they can strongly influence biology by driving the assembly of supramolecular structures that govern adhesive signaling, such as integrin clusters [67–69]. Many studies have utilized patterning technologies to add nanotexture to simulate the nanotopography formed by supramolecular ECM structures. These studies have systematically varied nanotopographical patterns and characterized the resulting cellular responses, with cellular responses generally depending on pattern geometry, periodicity, and other features. For example, parallel patterns such as grating and grooves are frequently observed to induce cellular and cytoskeletal alignment with the patterned features [70,71]. Incorporation of isotropic nanopost and nanopit topographies have also been observed to influence cell spreading and adhesive complex formation [72–74]. In a particularly notable recent study, Puliafito and colleagues utilized polarized laser beams to spatially and temporally deform otherwise static nantopographies to mechanically stimulate cells. In this system, the polarization pattern of the laser deforms photosensitive polymer micropillars beneath attached cells into an anisotropic pattern. The resulting deformation pattern induced cells to orient and align stress fibers along the direction of deformation. This system showed light-responsive materials could be used to observe and study biological response to dynamic topographies [75].

Previous work has postulated that nanotopography influences cell behavior through many different mechanisms, including through increased cell-ECM interaction along the surfaces of the features and through cortical actin rearrangement from the curving of the cell membrane around nanotextured features [76]. Despite these hypotheses, the precise molecular mechanisms behind cell sensing of nanotopography have remained elusive [74]. Towards this end, one study examined cells cultured on nanopillar arrays of varying density to identify key molecular length scales. At high nanopillar densities cells attached and formed adhesions only on the nanopillar tops, as they would on a flat surface. Lowering the density led to engulfment of the nanopillars and more adhesions along the

sides of the nanopillars, resulting in increased contact area and F-actin colocalization along the sides of the nanopillars. The authors associated these regimes with length scales of integrin clustering and migratory process formation [77]. In another study, cells cultured on nanopillars were found to assemble branched F-actin along the curved membrane adjacent to the features, leading to reduced assembly of SFs and mature focal adhesions throughout the cell. The altered F-actin assembly was accompanied by localization of Arp2/3 and formin-binding protein 17 (FBP17), which has a curvature-sensing F-BAR domain, at the ends of the nanopillars (Figure 2.1A). Cells expressing a truncated FBP17 mutant lacking the actin polymerization-inducing domain did not accumulate F-actin at the nanopillars, indicating that FBP17-actin binding senses the curved cell membrane and mediates the nanotopography-induced actin polymerization [78].

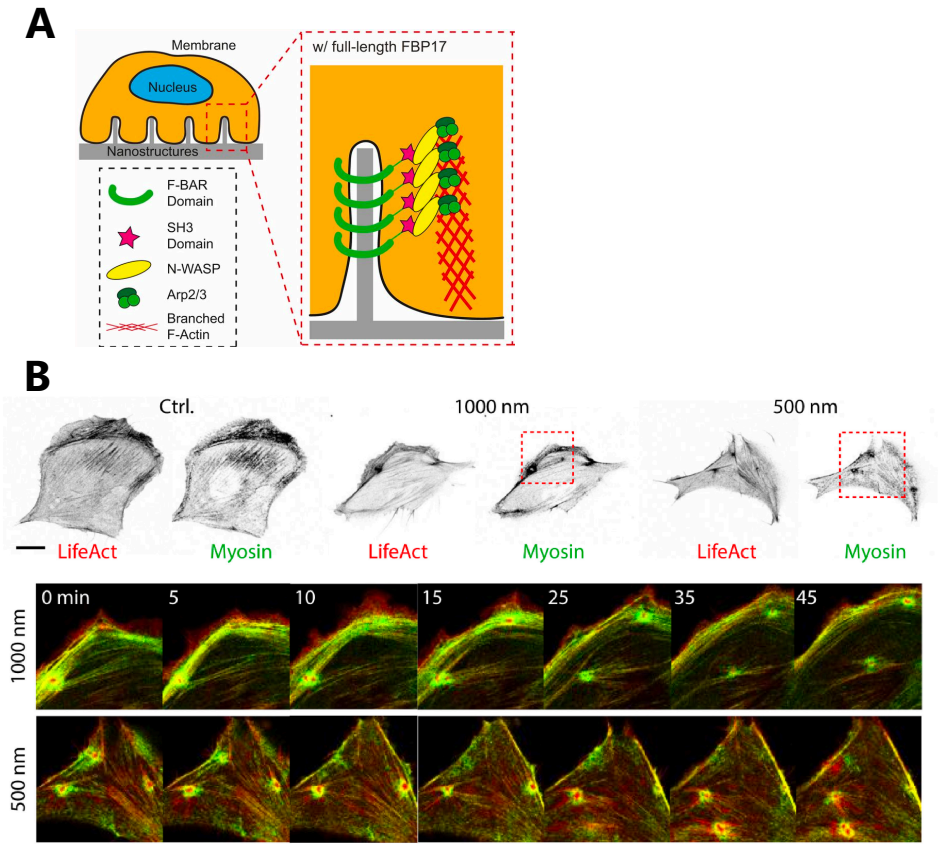


Figure 2.1. Mechanisms of cell sensing of 2D substrate geometric cues.
(A) Illustration of F-actin assembly around membrane curved by a nanotopographic feature. The protein FBP17 senses the curved membrane and recruits N-WASP and Arp2/3 to nucleate the assembly of branched actin around the feature. (B) Contractile myosin rings regulate the cytoskeleton and substrate topography sensing. Top panel: On flat control surfaces, F-actin is organized into bundles, and there are no puncta. On electrospun surfaces, myosin rings form around actin foci as cells respond to the underlying topography, visualized as puncta in the images (red boxes). Bottom panel: Time lapse imaging shows the formation and disassembly of myosin (green) and actin (red) foci. Reproduced with permission from Lou et al. [77] (A), Di Cio et al. [78] (B).

In a complementary study, cells cultured on electrospun nanofibers of varying diameters exhibited disrupted actin bundle assembly on increasingly narrow fibers. Time lapse imaging revealed that cells on narrow fibers (<1000 nm diameter) initially assembled actin bundles during early phases of spreading. However, during later, more contractile phases of spreading, these bundles coalesced into punctate actin foci as the narrowly confined adhesions failed to stably support parallel arrays of actin bundles. These foci were found to be surrounded by myosin rings and to sequester the actin-severing protein cofilin, leading to disassembly of the foci (Figure 2.1C). In other words, sensing of nanotopography is governed both globally by the cellular actomyosin network and locally by individual adhesions [79]. Combined, these studies suggest that nanotopography influences cell behavior by modulating the spatial organization of the actin cytoskeleton, through engulfment of features and curving of the cell membrane around features.

While the incorporation of nanotopographically textured substrates represents an important step towards creation of 3D architecture, such surfaces are incapable of capturing a number of defining features of 3D tissues, including steric hindrance of spreading and migration along all axes and the absence of externally imposed apical-basal polarity [54]. We now discuss efforts to overcome these limitations through the development of microtopographically patterned substrates and fully 3D matrices.

2.4.2 Microtopographical confinement

There are many physiological contexts, including development, inflammation, and cancer, in which cells must migrate through confined spaces in tissue. For example, tumor cells must squeeze through tight physical barriers imposed by cells and ECM in order to invade and metastasize. Because these confined features cannot be captured with 2D patterning tools and are challenging to standardize in 3D systems, microchannels have emerged as a valuable paradigm for studying confined migration. These devices model cells squeezing through tight spaces, with 3 or 4 walls physically confining cells and only allowing migration along the axis of the microchannel. Previous studies have shown that cells, especially tumor cells, reorganize their cytoskeleton to a primarily cortical distribution of actin in order to squeeze through the channels. The cells traversing the channels also have decreased numbers of focal adhesions and stress fibers compared to fully spread cells on a 2D surface [80–83].

Recently, new mechanistic insight into how tumor cells navigate confined spaces in tissues has been obtained by measuring cellular viscoelastic properties during confined migration. For example, we recently used an open microchannel system in which tumor cells could be subjected to confined migration while still being accessible to atomic force microscopy (AFM) measurements. Cells softened as they experienced confinement, with the actin cytoskeleton deploying away from the basal surface and towards the channel

walls, potentially to support lateral traction forces. Confinement-induced softening was also accompanied by exclusion of YAP from the nucleus [84]. Confinement-induced changes in cell mechanics were also reported in a study with optical tweezer–based microrheology. In a spheroid invasion assay in a biomimetic collagen matrix, tumor cells at the tip of invasion stalks were found to have a higher viscosity than the cells in the interior of the stalk. Inhibition of FAK or actin polymerization diminished mechanical differences between leader and follower cells [85]. Both studies directly demonstrate that tumor cells can mechanically adapt to confined geometries through coordinated cytoskeletal rearrangements that produce cell-scale changes in viscoelastic properties.

Additional microchannel studies have incorporated more complete confinement, either by manipulating channel geometry or introducing a fourth wall. Cells fully confined within collagen microtracks displayed more adhesive contacts, faster migration, and greater matrix strains than their more partially confined counterparts. The increased migration speed of fully confined cells suggests that contractility is key in migration under full confinement [86]. In narrow (3 μm width) PDMS microchannels, cells also exhibited increased migration speeds and displayed strong blebbing behavior at both their leading and trailing edges (Figure 2.2A). As cells squeezed into the channels, they underwent an ECM-induced transition from actin protrusion-driven mesenchymal to faster RhoA contractility-driven ameboid migration, accompanied by a loss of F-actin organization in the cell body (Figure 2.2A-B) [87,88]. Similarly, when *Dictyostelium* cells cultured in a sandwich paradigm were subjected to external pressure, the cells switched from actin polymerization-based pseudopod migration to myosin II contractility-driven bleb migration with recruitment of myosin II to the cortex [89]. Collectively, these studies indicate that increased confinement of cells, due to either a smaller pore size or increased mechanical pressure, stimulates cells to reorganize their cytoskeleton to a primarily cortical distribution and utilize an amoeboid, contractility-dependent mode of migration.

2.4.3 Fully 3D systems

While microtopographical systems have offered valuable insight into geometric regulation in 3D, an important goal for the field remains the development of engineering strategies amenable to “true” 3D geometries in which cells are fully encapsulated within ECM. Hydrogels composed of either synthetic or natural ECM materials allow for encapsulation of individual cells or spheroids to recapitulate the dimensionality of 3D tissues [56,90]. We conclude by highlighting efforts to extend geometric regulation of cell behavior to 3D hydrogel ECMs.

Micropatterning has recently been used to investigate the effects of 3D cell geometry and volume on cell behavior in a fully encapsulated setting. In one study, a silicon mold was

used to create different prism-shaped wells of defined geometry and size on a hyaluronic acid hydrogel. Single cells were seeded into each well, and the wells were coved with a thick slab of hydrogel to achieve 3D encapsulation. The study identified an optimal range of niche volumes that promoted clear stress fiber assembly and cytoskeletal organization, irrespective of niche projected area or height. Volumes smaller or larger than this range resulted in few stress fibers. In niches of equal volume but different geometries, cells with anisotropic geometries such triangular and rectangular prisms exhibited more stress fibers, focal adhesions, and actomyosin contractility compared to cells with isotropic geometries (cylinder, cube) [91]. In a subsequent study, the both the stiffness and volume of the niches were varied to perturb the combined effects of cell volume and substrate stiffness on cell behavior. Interestingly, irrespective of the stiffness of the hydrogel, cells cultured in the optimal volume range identified in the previous study always formed stable focal adhesions and stress fibers, while cell in volumes smaller than the optimal range did not (Figure 2.2C). In this setting, cell volume overrides substrate mechanics in guiding adhesion and mechanics [92]. Most 3D tissues are fibrous with structural heterogeneity and anisotropy. The orientation of ECM fibers affects ECM mechanics and cell-ECM interactions [93]. Hydrogels do not, in general, capture such highly structured topologies, necessitating the development of new materials to control fibril alignment and other topographies in 3D hydrogels [55,56]. A recently developed nanocomposite hydrogel system exploited embedded cellulose nanocrystals that align in response to magnetic fields to create an anisotropic topography.

Myotubes cultured in these matrices showed strong co-alignment of F-actin and the nanocrystals [94]. Using a related approach, Paul and colleagues created aligned fibrils in 3D hydrogels using ECM protein-conjugated magnetic colloidal particles to study the effects of fibril alignment on cell behavior. Under the influence of an external magnetic field, the beads aligned to create parallel fibrils. Fibroblasts seeded in aligned matrices produced longer actin-based protrusions than cells in unaligned matrices, and the protrusions were aligned either parallel or perpendicular to the fibril direction (Figure 2.2D). Inhibition of myosin II in fibroblasts in the aligned matrices abrogated the alignment of protrusions, indicating that myosin II-regulated cell contractility may play an important role in cell topography sensing [95]. Jointly, these studies provide tools for creating aligned topographies within hydrogels and highlight the importance of the actin cytoskeleton in mediating these responses.

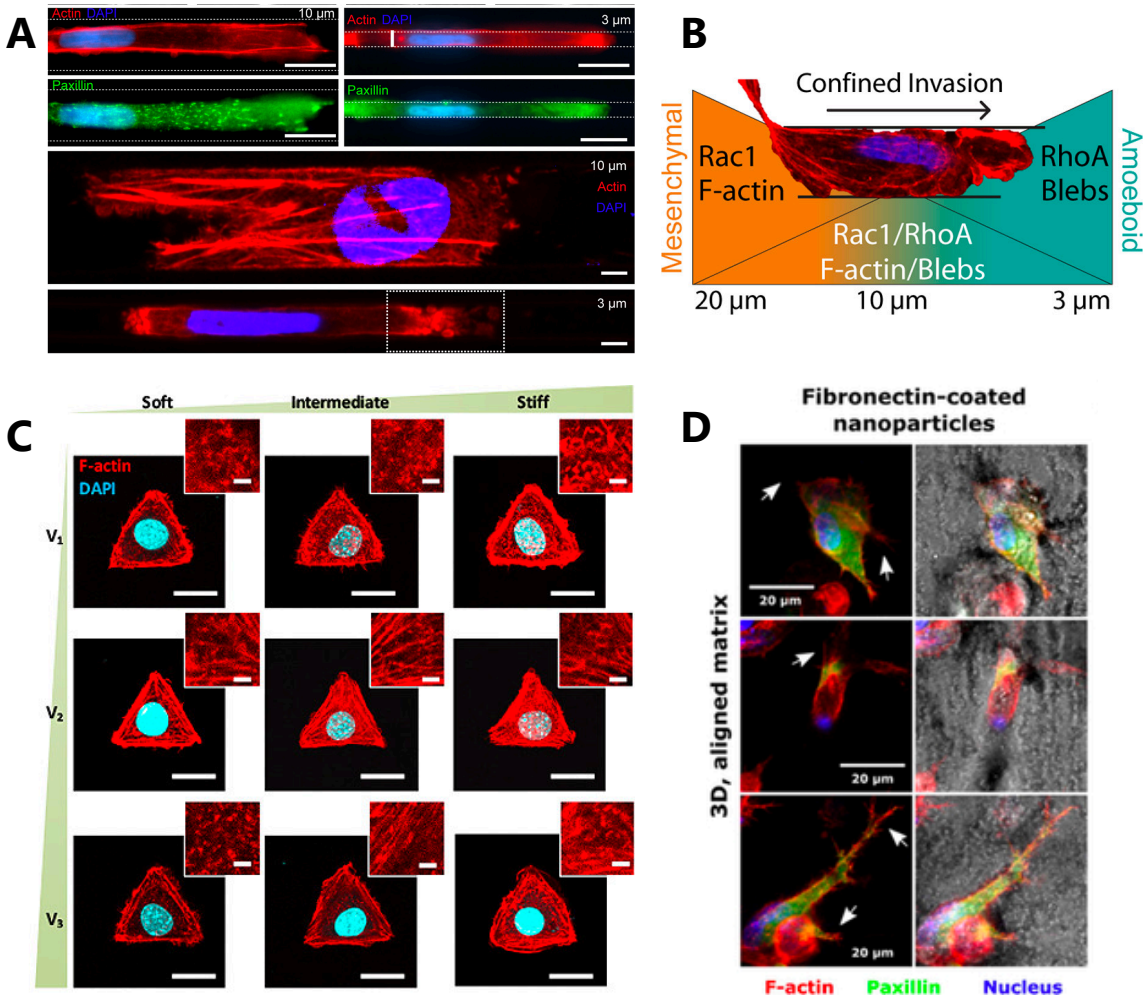


Figure 2.2. Effects of 3D geometry on cytoskeletal organization and cell behavior.
(A) Confinement of cells within increasingly narrow microchannels significantly disrupts the organization of F-actin and focal adhesions. Top 2 rows of images: Cells traversing 10μm-wide channels exhibit bundled F-actin and well-defined focal adhesions, as visualized by localization of paxillin (green) and actin (red). Conversely, cells confined within 3μm channels lack clear focal adhesions or F-actin bundles. Bottom 2 images: Higher magnification imaging of F-actin reveals an organized actin in cells in 10μm channels (Top), while cells in 3μm channels have disorganized F-actin networks and display blebs at both ends of the cell (Bottom). The dashed box in the bottom image highlights multiple blebs at the leading edge of the cell. (B) Schematic illustrating how increasingly confined geometries can trigger a transition from mesenchymal migration to RhoA contractility-based amoeboid migration. 20μm, 10μm and 3μm indicate the width of the confining microchannel. (C) In microwells of independently controlled volume and stiffness, medium volume V2 promoted robust stress fiber assembly while larger and smaller volumes (V1 and V3) did not. (D) In 3D hydrogels with aligned fibronectin-coated nanoparticles-based fibers, cells preferentially extended multiple protrusions parallel or perpendicular to aligned fibers. Left column: maximum intensity projections of confocal slices, with F-actin displayed in red, paxillin in green, and the nucleus in blue. Right column: brightfield with superimposed fluorescent images to show particle alignment. Arrows indicate cell protrusions in the plane of the fibers. Reproduced with permission from Holle et al. [86] (A, B), from Bao et al. [88] (C)., Paul et al. [91] (D).

2.5 Conclusion

Engineered culture systems continue to advance our understanding of how cell and ECM geometry controls cell behavior, while reinforcing the central role played by the actin cytoskeleton in transducing geometry into phenotype. As described in this brief review, the past several years have seen important advances in the field's mechanistic understanding of how 2D matrix geometry acts through the cytoskeleton to influence phenotype. There has also been exciting progress towards advancing these ideas to 3D. In addition to the areas discussed here, a number of other, equally interesting challenges are being pursued. As one example, significant effort is being devoted to extend geometric regulatory concepts to multicellular structures, including those containing heterogeneous cell populations [96,97]. In these settings, it will be important to understand how cytoskeletal structure and mechanics are regulated not only in a cell-autonomous fashion but as coordinated units across multiple cells [98]. When married to the advanced fabrication strategies described here, it may soon be possible to create microscale, three-dimensional tissues with a variety of component cell types positioned as they might be in living tissue. These "engineered organoids" should lend great new insight into biological processes such as development, morphogenesis, wound healing, and cancer and provide powerful new enabling tools to tissue engineering and regenerative medicine.

Chapter 3: Identifying the contributions of actin-disassembly factors to 3D migration through HA matrices

Vivien D. Tran, Kwasi Y. Amofa, Miles Duong, Sanjay Kumar (2024). Manuscript in preparation.

3.1 Introduction

Cell migration is critical to many biological processes, including wound healing, embryogenesis, and cancer progression. To navigate through three-dimensional (3D) extracellular matrix (ECM), cells must dynamically remodel their cytoskeleton to adapt to ECM characteristics, including mechanics, micro/nanostructure, and degradability [99]. This complex process requires coordinated action of many molecular components, with the actin cytoskeleton playing a central role in cell locomotion [3,4]. A core group of actin-binding proteins is responsible for driving actin disassembly and turnover within the cell [12]. These factors – including cofilin, profilin, twinfilin, gelsolin, Srv2/cyclase-associated protein, and actin-interacting protein /WD repeat protein – stabilize or modulate the actin network as needed to facilitate navigation through the ECM [12–14].

Cell migration has been historically studied on two-dimensional (2D) tissue culture surfaces, a powerful and simple paradigm to thoroughly characterize the mechanics of cell locomotion. However, cells navigating though tissues are often surrounded by a 3D ECM, sometimes encountering topographical cues absent in flat 2D substrates, including steric confinement, fibers or bundles that may serve as contact guidance cues, and adhesions in all directions [54]. Cells also display more migration modes in 3D, while in 2D cells often but not exclusively utilize flat, fan-shaped F-actin-based protrusions termed lamellipodia [1,7]. Much of what is known about the role of the actin turnover machinery in 3D migration comes from fibrillar matrices, including collagen and fibrin. In these matrix environments, the mechanisms of cellular migration, particularly of actin organization and turnover, are highly dependent on dimensionality and the biophysical properties of the matrix [99–101]. The morphological linearity imposed by adhesion to fibers often induces alignment of the focal adhesions and the actin cytoskeleton, which depends on the tight regulation of actin polymerization dynamics [81,102–104]. For example, in one study with fibrillar cell-derived matrices and Matrigel, inhibition of LIMK did not affect the 2D motility of breast cancer cells. Conversely, the attenuated LIMK activity impaired 3D invasion by reducing invadopodia, impairing the invadopodial maturation and matrix degradation [105]. Invadopodia have also been robustly induced by high density fibrillar collagen, whereas cell-derived fibronectin, gelatin, and low density collagen induced invadopodia to a much lesser extent [106]. In a similar vein, in collagen matrices, fibroblast motility is associated with the development of either 2D-like lamellipodia or lobopodia, which are

driven by hydrostatic pressure rather actin polymerization-driven protrusions. The type of protrusion depends on the degree to which the matrix exhibits nonlinear elasticity [1,2]. Collectively, these examples demonstrate the need to examine cell migration in a physiological context, as both actin organization and the associated intracellular signaling vary widely between each mode of migration.

While the studies discussed above have lent tremendous insight into mechanisms of 3D migration, comparatively little is known about the mechanisms of cell migration through defined, non-fibrillar, tissue-mimetic matrices, such as hyaluronic acid (HA). HA is major component of the brain parenchymal ECM, which is generally devoid of collagen, fibronectin, and laminin and lacks the fibrillar contact guidance cues presented by those proteins [107]. We have previously characterized a mode of migration utilized by GBM cells to navigate through 3D HA-rich matrices that involves long, thin actin/microtubule-based protrusions termed microtentacles (McTNs). McTNs adhere to HA via CD44 and are laden and stabilized by both actin and microtubules, both of which distinguish these structures from filopodia or lamellipodia [108]. Our and others' findings therefore suggest non-canonical roles for the actin turnover machinery in non-fibrillar 3D matrices, inviting deeper investigation [81,109–112].

In this study, we explore contributions of the actin turnover machinery to 3D motility in the context of GBM invasion through HA matrices. By applying a targeted CRISPR knockout (KO) screen to a panel of core actin turnover proteins, we find that CFL suppression results in faster 3D invasion, whereas suppression of other targets slows invasion. Protrusions formed by CFL KO cells are longer and more abundant than those of control cells, suggesting that CFL suppression increases invasion in 3D HA through actin stabilization. Our results collectively support a mechanism in which CFL suppression promotes protrusion function through F-actin stabilization, thereby enhancing penetration through 3D HA matrices and facilitating invasion.

3.2 Results

3.2.1 CFL is unique among actin-disassembly factors in driving 3D migration through HA matrices

To examine how the systems that govern actin turnover machinery on 2D substrates translate to 3D contexts, we conducted a limited CRISPR-Cas9 KO screen to systematically assess contributions of actin-binding proteins to 2D and 3D motility. Based on our previous work that supported a model in which cell front-back polarity is driven in part by CFL activity and actin turnover, we focused on targets that are part of the core actin disassembly-promoting machinery. These factors mediate actin turnover to reorganize the actin cytoskeleton as the cell navigates the ECM [12–14]. For proteins with more than one isoform, we chose to knock out the most abundantly expressed isoform in human

cells; the abbreviations for each protein hereafter denote that isoform. Our resulting targets were cofilin-1 (CFL), profilin-1 (PFN), twinfilin-1 (TWF), gelsolin (GSN), Srv2/cyclase-associated protein 1 (CAP), and actin-interacting protein 1 /WD repeat protein 1 (WDR). To create the KO cell lines, we sequentially delivered via lentivirus Cas9 cDNA and sgRNAs targeting the gene of interest, generating cell lines that stably expressed Cas9 along with sgRNAs and producing a mixture of indels. Control cell lines were created by using sgRNAs that targeted non-coding (NC) regions of the genome or were non-targeting (NT).

To compare 2D and 3D motility within a non-fibrillar matrix, we cultured U251 glioblastoma cells [82,113] in or on engineered HA hydrogels, which mimic brain ECM and have been used in our previous work to dissect molecular mechanisms of GBM invasion [40,108,114–116]. HA hydrogels may be fabricated with brain-like elastic moduli (10 Pa – 1 kPa) and functionalized with RGD-based peptides to allow integrin engagement [108,114]. The HA matrix is crosslinked with matrix metalloprotease-degradable peptide sequences, and the matrix backbone itself may be degraded via cell-derived hyaluronidases [114].

We first examined 2D random, single-cell motility of our KO cell lines on HA conjugated with RGD (HA-RGD) to establish baseline migratory phenotypes. Cells were allowed to spread and adhere on the gels for 4 hours before prior to timelapse imaging. CFL, TWF, and WDR KO cells displayed significantly reduced cell speed during a timelapse of 7.5 hours compared to NT control, indicating that loss of these actin-binding proteins hampered the cells' ability to migrate in 2D (Figure 3.1A). These results match previous studies of the role of these proteins (CFL, TWF, and WDR) in 2D migration, consistent with their established role in lamellipodial extension [12]. CAP, GSN, and PFN KO cells had increased persistence relative to controls (Figure 3.1B).

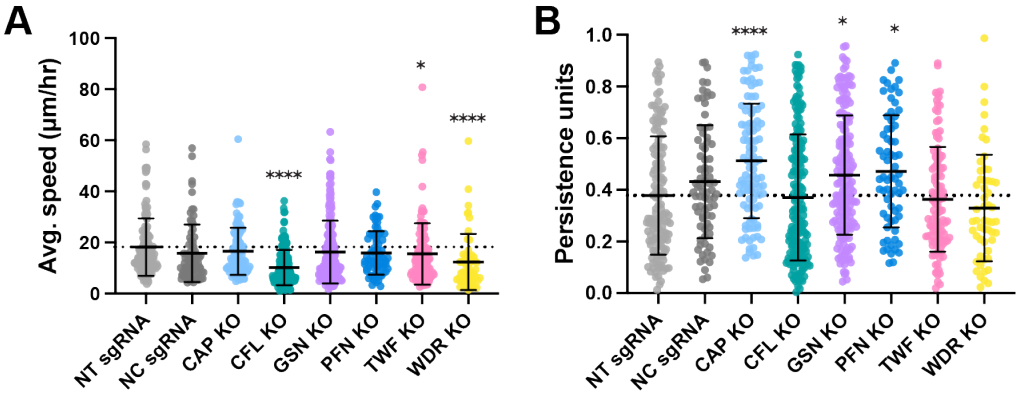


Figure 3.1. Random single cell motility of CRISPR KO cells on 2D HA-RGD gels.
Cells were tracked for 46 points over a period of 7.75 hours, with 10 minutes between each point. (A) When compared to NT control cells, CFL KO, TWF KO, and WDR KO cells have significantly slower average speeds. (B) CAP KO, GSN KO, and PFN KO have significantly higher persistence compared to NT control. For both graphs, the dashed lines denotes the mean value of NT sgRNA control and error bars represent mean with SD. *P < 0.05 , **P < 0.01, ****P < 0.0001 by Kruskal-Wallis test followed Dunn's multiple comparisons test.

To examine the effects of depletion of these proteins on 3D motility, we conducted 3D spheroid invasion assays in HA-RGD gels crosslinked with protease-degradable linkers. We hypothesized that CFL, GSN, TWF, and WDR KO would diminish 3D motility based on the results of the 2D motility assay. After 4 days of invasion in HA-RGD gels (Figure 3.2A), CFL KO cells surprisingly displayed the highest migration speed of all cell lines, including controls, as measured by area change (Figure 3.2B) and maximum cell distance from the core spheroid (Figure 3.2C). This result was the opposite from 2D, where CFL KO led to slower cell migration (Figure 3.1A). The other KO cell lines did not show significant increases in 3D area change in the HA-RGD matrix compared to NT control, while PFN KO and WDR KO had significant decreases (Figure 3.2B). Of note, CAP KO showed both increased area change (Figure 3.2B) and significantly increased maximum cell distance (Figure 3.2C), albeit at a lower magnitude that CFL KO. Considering that CAP is a cofactor of CFL, this result in tandem with the CFL KO results indicate that attenuating CFL activity increases 3D motility in HA-RGD matrices.

We next asked if CRISPR KO of these same targets would modulate 3D migration through "bare" HA gels lacking pendant RGD peptides (HA-only), where cells presumably rely on non-integrin-based adhesion receptors to navigate the matrix. In an HA matrix, cells can interact with the polysaccharide backbone with membrane receptors such as CD44 and `Receptor for HA-Mediated Motility (RHAMM) [117,118]. In the HA-only gels, CFL KO spheres notably were the only ones to invade after 11 days, while all other cells lines displayed minimal protrusion and infiltration into the surrounding matrix (Figure 3.2D). CFL KO cells had both significantly increased area change and maximum cell distance compared to NT control (Figure 3.2E-F). In our past work bare HA matrices have frequently been restrictive of GBM cell invasion relative to HA-RGD matrices [116,119], so it was remarkable to observe CFL KO cells robustly invading the HA-only gels. Mirroring the HA-RGD results, PFN KO and WDR KO cells had both significantly decreased area change and maximum cell distance compared to control (Figure 3.2E-F). Taken together, the result of our 3D invasion studies suggests that the loss of PFN and WDR expression inhibit 3D migration and suppression of CFL activity speeds up 3D migration through HA matrices. Only CFL KO produced appreciable 3D invasion in migration-restrictive HA-only matrices, highlighting a special role for CFL in migration through 3D HA.

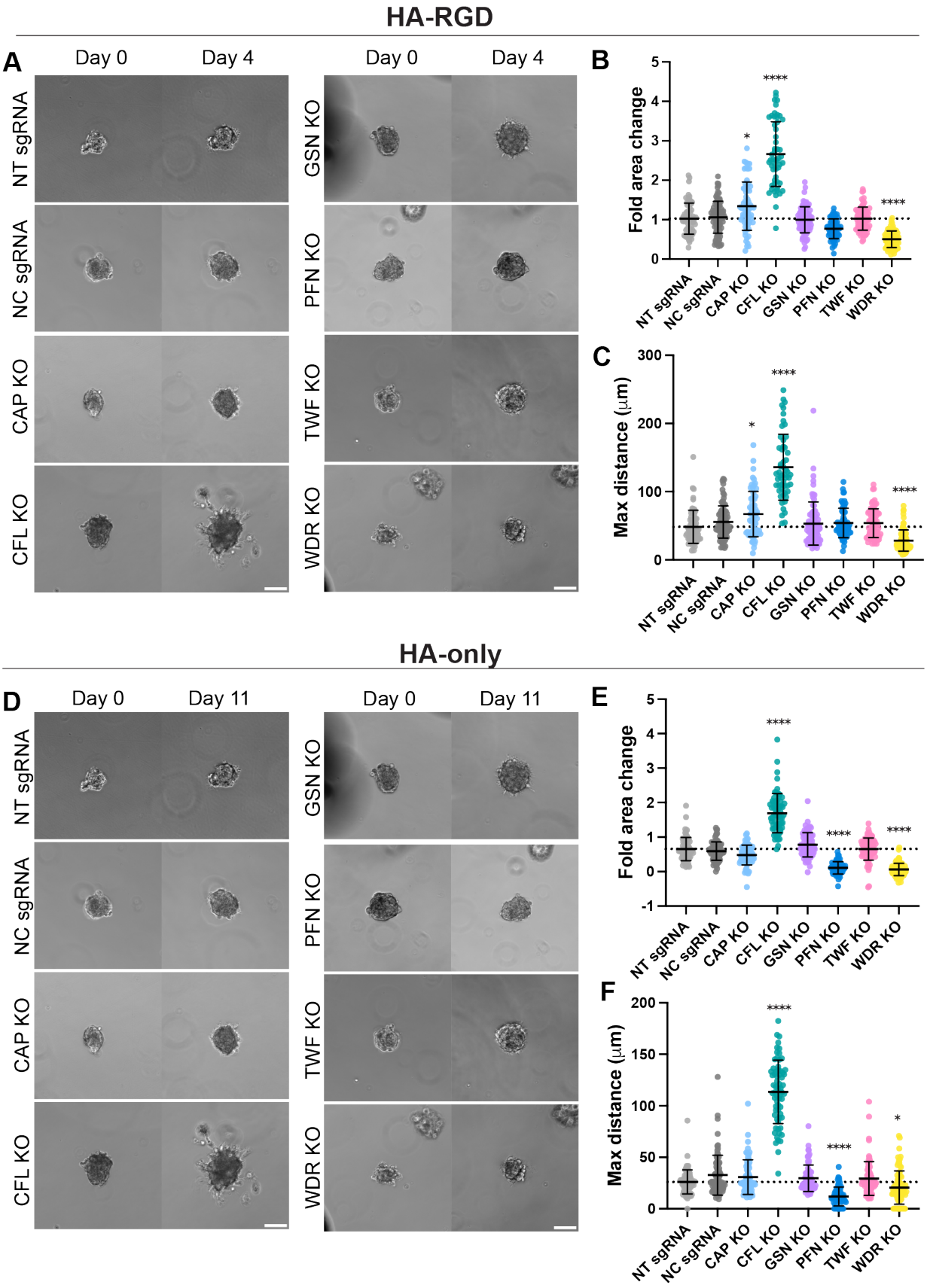

HA-RGD
A
Day 0
Day 4
Day 0
Day 4
NT sgRNA
NC sgRNA
CAP KO
CFL KO
GSN KO
PFN KO
TWF KO
WDR KO
B
Fold area change
C
Max distance (μm)
HA-only
D
Day 0
Day 11
Day 0
Day 11
E
Fold area change
F
Max distance (μm)

Figure 3.2. 3D spheroid invasion assay of CRISPR KO cells in 3D HA gels.
(A) Representative brightfield images of spheroids at day 0 and day 4 for each cell line in HA-RGD gels. (B) Calculated fold area change of day 4 normalized to day 0 area of spheroids. CFL KO shows significant increase compared NT control, while WDR KO significantly decreases area change. (C) Maximum cell distance from the sphere edge. CFL KO shows significant increase compared NT control, while WDR KO significantly decreases maximum cell distance. (D) Representative brightfield images of spheroids at day 0 and day 11 for each cell line in HA-only gels. (E) Calculated fold area change of day 11 normalized to day 0 area of spheroids. CFL KO shows significant increase compared NT control, while PFN KO and WDR KO significantly decreases area change. (F) Maximum cell distance from the sphere edge. CFL KO shows significant increase compared NT control, while PFN KO and WDR KO significantly decreases maximum cell distance. In all graphs, the dashed lines denotes the mean value of NT sgRNA control and error bars represent mean with SD. *P <0.05, ****P < 0.0001 by Kruskal-Wallis test followed Dunn's multiple comparisons test. Scale bar: 100 μm.

3.2.2 CFL KO drives 3D motility by favoring greater actin polymerization and stability in cellular protrusions.

Extension of cellular protrusions is one of the key steps in the classical cell motility cycle. Whereas in 2D cells frequently but not exclusively extend lamellipodia to advance the leading edge, cells in 3D cells utilize a large diversity of protrusive mechanisms to advance through the ECM, which vary in their actin-dependence and can change to adapt to the features of a given matrix [1,120,121]. As discussed in the introduction, we previously identified a mechanism through which GBM cells interact with and migrate through 3D HA-matrices using actin- and tubulin-based McTNs [108]. In other work, highly metastatic and invasive cancer cell lines had more protrusions per cell and longer protrusion lifetime than less invasive cell lines, shown to be dependent on the LIMK/CFL pathway [105,110]. During invasion through the ECM, actin polymerization provides the necessary force for these cellular protrusions to extend through the matrix and overcome the surrounding steric hindrance [4]. As the proteins in our CRISPR screen have key roles in actin turnover, we asked whether KO of our target proteins would affect cell protrusion phenotype and were especially interested in determining if CFL KO, which sped up 3D invasion, would also induce positive changes in protrusions. To quantify and compare protrusion phenotype across the cell lines, we employed a protrusion formation assay developed in our previous study [108]. We seeded single cells into 3D HA-only and -RGD gels and let the cells form protrusions for 4 days before fixing and staining with phalloidin. Using z-stack maximum projections of F-actin-stained cells, we quantified the number and maximum length of protrusions per cell (Figure 3.3A, D). In both HA-only and -RGD gels, CFL KO cells had the longest and most protrusions per cell, implying that CFL suppression most strongly favored actin polymerization and stability in the protrusions (Figure 3.3C-B, E-F). Collectively with our 3D invasion data, this finding suggests that the loss of CFL stabilizes actin-based protrusions, which in turn promote faster migration through the HA matrix.

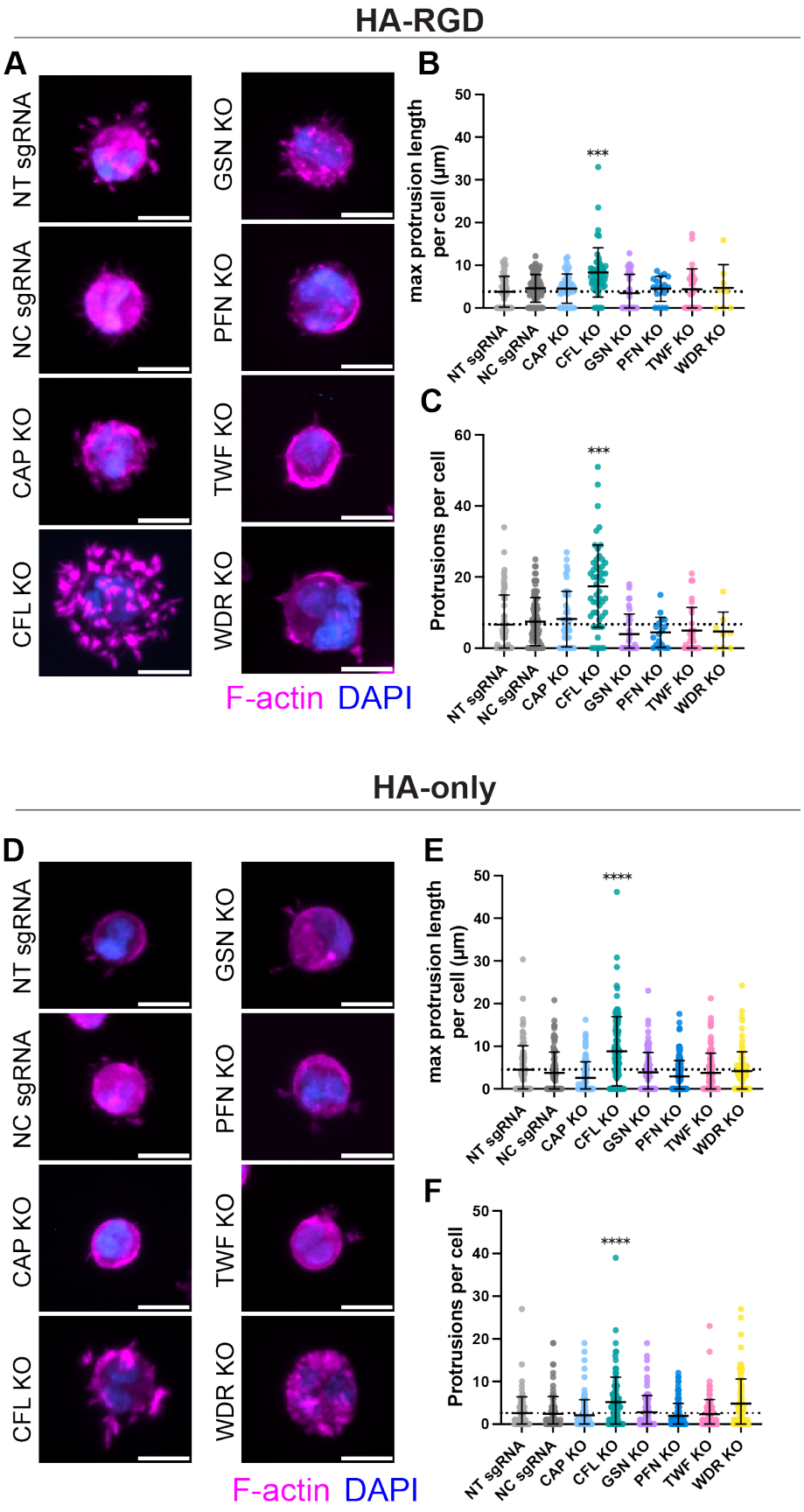

HA-RGD
A
NT sgRNA
NC sgRNA
CAP KO
CFL KO
GSN KO
PFN KO
TWF KO
WDR KO
F-actin DAPI
B
max protrusion length per cell (µm)
***
C
Protrusions per cell
***
NT sgRNA
NC sgRNA
CAP KO
CFL KO
GSN KO
PFN KO
TWF KO
WDR KO
HA-only
D
E
max protrusion length per cell (µm)
****
F
Protrusions per cell
****

Figure 3.3. 3D protrusion formation assay of CRISPR KO cells in HA gels.
Cells were allowed to form protrusions for 4 days before fixation and analysis. (A) Representative images of cells in HA-RGD gels. Magenta is F-actin, blue is DAPI. (B) Number of protrusions per cell. CFL KO has significantly increased protrusion numbers while PFN KO significantly decreased protrusion numbers compared to NT control. (C) Maximum protrusion length per cell. GSN KO shows significantly shorter protrusions than NT control. (D) Representative images of cells in HA-only gels. Magenta is F-actin, blue is DAPI. (E) Number of protrusions per cell. CFL KO has significantly increased protrusion numbers compared to NT control. (F) Maximum protrusion length per cell. CFL KO shows significantly longer protrusions than NT control. In all graphs, error bars represent mean with SD. ****P < 0.0001 by Kruskal-Wallis test followed Dunn's multiple comparisons test. Scale bar: 20 μm.

3.3 Discussion and conclusions

It is unclear how the systems the regulate actin turnover that have been broadly characterized in 2D operate in 3D migration [1,101], particularly in defined, non-fibrillar matrices such as hyaluronic acid (HA). In this study, we investigated contributions of the actin turnover machinery to 3D invasion of GBM cells through HA. Our CRISPR KO screen of core actin turnover proteins revealed that only CFL suppression produced differential effects in 2D and 3D motility, slowing motility in 2D and increasing it in 3D. Additionally, CFL KO cells were distinct among screened candidates in forming longer and more actin-based protrusions per cell, hinting at a role of actin stabilization in improved 3D migration. Our data supports a model in which attenuated CFL activity stabilizes actin within protrusions, allowing for enhanced penetration and invasion through the surrounding matrix.

Previous work has shown that actin-rich protrusions in a 3D matrix have been used for adhesion to and penetration through the matrix [108,110,120,122]. These studies share a common mechanism in which F-actin stability supports protrusion formation and extension through the ECM [120]. In one study, highly metastatic tumor cells produced more and longer-lived filopodial protrusions than less aggressive tumor cells. This phenotype depended on LIMK-mediated CFL inactivation, with diminished CFL activity stabilizing F-actin within the protrusions [110], consistent with our results. The LIMK/CFL signaling pathway has also been implicated in the maturation of invadopodia for matrix degradation. Increased CFL activity decreased F-actin stability within the invadopodia, thereby inhibiting matrix degradation via matrix-metalloproteinases (MMPs) and decreasing 3D motility [105,123,124]. While we did not probe the molecular structure of the protrusions in this chapter, it is highly likely that the protrusions we observed are involved in degradation of the surrounding ECM.

Although all the proteins screened in this study are important regulators of actin turnover, CFL KO was the only condition to significantly increase 3D motility and did so to a much larger degree than control cells. We attribute this result to the special role of CFL in actin

severing [125–127], a function not shared by other proteins in the screen [11,127–129]. Loss of the function of the other proteins, such as filament capping, monomer recycling, and depolymerization at filament ends, may be more adverse than CFL KO and mask any phenotype changes. It would be fruitful to repeat these studies in other cell types and matrix conditions that support 3D migration through actin-dependent but non-filopodial/microtentacle-based mechanisms to query whether the proteins in the screen have similar contributions to those modes of motility.

Using a defined and engineered hydrogel platform, we were able to characterize the contributions of actin turnover proteins to GBM cell motility through 3D HA matrices. We demonstrated that suppression of CFL increased both the length and number of protrusions to speed up 3D motility. In future studies, it would be valuable to capture the dynamics of the protrusions to directly quantify the temporal stability of the protrusions. While we found that CFL KO uniquely increased 3D motility and protrusion stability in our 3D HA matrix platform, this may not be the case other matrix conditions. Other studies have implicated the proteins in the panel in cancer progression, where 3D motility is a major mechanism, so it would be likely that suppression of other proteins would affect 3D motility in other biomimetic matrices. Our work provides insight into the contributions of actin turnover within protrusions and 3D motility and how the mechanisms from 2D motility translate to 3D.

3.4 Methods

All key resources are listed in Supp. Table A1.

Cell culture

U-251 MG human GBM (U251) cells were obtained from the University of California, Berkeley Tissue Culture Facility. The cells were cultured in Dulbecco's modified Eagle's medium (DMEM, Gibco) supplemented with 10% (v/v) fetal bovine serum (FBS; JR Scientific), 1% (v/v) non-essential amino acids (Gibco), 1% (v/v) sodium pyruvate (Thermo Fisher Scientific), and 1% (v/v) penicillin/streptomycin (Gibco). Cells were passaged every ~7 days with media changes every other day and harvested using 0.25% trypsin-EDTA (Thermo Fisher Scientific). Cells were passaged less than 30 times and were screened every three months for myocoplasma. All U251 cells transduced with sgRNA expression plasmids were maintained in 1 μg/ml puromycin (Clontech). U251 cells transduced with Cas9 and sgRNA expression plasmids were additionally maintained in 10 μg/ml blasticidin (Invivogen).

CRISPR KO cell line generation

Cas9 and sgRNA expression vectors were stably introduced to U251 cells using methods previously described [130]. Briefly, the lentiCas9-blast plasmid (Addgene 52962) was

transfected into HEK 293T cells (provided by the David Schaffer laboratory at UC Berkeley, originally sourced from ATCC Cat# CRL-11268, CVCL_1926) using 3rd generation lentiviral packaging plasmids (pMD2.G, Addgene 12259; pMDLg/pRRE, Addgene 12251; pRSV-Rev, Addgene 12253) using PolyJet reagent (SignaGen) [131,132]. The supernatant was harvested at 48 h and 72 h post-transfection and syringe filtered through a 0.45 µm pore-sized filter (Millipore) and then pooled. The filtered supernatant was used to transduce U251 cells at a multiplicity of infection (MOI) of 1 with 10 µg/ml polybrene. After 48 h post-transduction, cells were selected using 10 µg/ml blasticidin for 2 weeks for Cas9 integration.

For each protein target in the KO array, three separate guides targeting the gene was generated using CRISPick (Broad Institute). Three non-coding (NC) and non-targeting (NT) guides were used as controls and have been previously published [133]. Oligos for each guide sequence (Elim Biopharma) with the appropriate overhangs were annealed and ligated into pMCB320 (Addgene 89359) digested with BstXI and BlpI (New England Biolabs) using T4 DNA ligase (New England Biolabs) [134]. All sgRNA sequences used in this study are listed in Supp Table A2. The sgRNA plasmids for the same genetic target were pooled together in proportional amounts and transfected with 3rd generation lentiviral packaging plasmids into HEK293Ts using PolyJet. At 48 and 72 post-transfection, the supernatant was harvested and filtered and pooled together. The filtered supernatant was used to transduce Cas9 U251 cells at a multiplicity of infection (MOI) of 2 with 10 µg/ml polybrene. Cells were maintained in 10 µg/ml blasticidin and 2 µg/ml puromycin starting at 48 h post-transduction to select for sgRNA integration and expanded 7 days post-transduction. pMD2.G, pMDLg/pRRE, pRSV-Rev, pMCB320, and lentiCas9-Blast were provided by the Britt Glaunsinger laboratory at UC Berkeley and were originally sourced from Addgene. pMCB320 was a gift from Michael Bassik. lentiCas9-Blast was a gift from Feng Zhang. Lentiviral packaging plasmids were a gift from Didier Trono.

Generation of spheroids

U251 cell spheroids were generated using AggreWell 400 plates (STEMCELL Technologies). Briefly, the wells of the AggreWell plate were incubated with an anti-adherence rinsing solution (STEMCELL Technologies) then washed with fresh media. U251 cells were seeded as single cells at a density of ~3 x 10^5 cells per well. Cells were allowed to grow and aggregate into spheres for 4 days. The spheres were then harvested and used for assays.

HA synthesis and RGD conjugation

HA hydrogels were fabricated as described previously [108,114]. Briefly, sodium hyaluronate (Lifecore Biomedical, Research Grade, 66 kDa - 99 kDa) was functionalized with methacrylic anhydride (Sigma-Aldrich, 94%) to synthesize methacrylated HA (HA-

Me). The extent of methacrylation per disaccharide was quantified with ^{1}H NMR as described previously and calculated to be approximately 85% for the HA-Me used in this study [114]. To add integrin-binding motifs, HA-Me was conjugated with RGD peptide Ac-GCGYGRGDSPG-NH2 (Anaspec) at a concentration of 0.5 mmol/L via Michael Addition. Crosslinker details are described in the 2D gel fabrication and 3D spheroid encapsulation sections below.

2D gel fabrication

Prior to gel fabrication, glass-bottom plates were coated with 1mg/ml poly-d-lysine solution (Sigma-Aldrich) and rinsed with 1x PBS (Fisher BioReagent) to enable gel adsorption to the glass. Phenol-free DMEM (Thermo Fisher Scientific) and HA-RGD solution at 6% (w/w) stock were mixed to generate a final concentration of HA-RGD of 5% (w/w). Bifunctional thiol dithiothreitol at 5% (w/w) stock (DTT, Thermo Fisher Scientific) was then added at thiol:HA monomer repeat (T:M) ratio of ~0.4 to achieve an shear modulus of ~6.5 kPa. The solution was plated at 6 µl per gel into the treated glass-bottom plates, then flattened with a plasma-treated glass coverslip, creating flat gels of ~120 µm in height. The flattened gels were incubated for 1 h in a humidified 37 °C chamber. Once the gels were cross-linked, the coverslips were removed and the gels were soaked in room temperature PBS overnight before cell seeding.

2D migration assay

Prior to seeding, U251 cells were incubated with SPY555-DNA (Cytoskeleton) at a final concentration of 1:1000 dilution for 24 h to visualize the nucleus. For single cell migration, cells were seeded onto tissue culture plate wells or HA-RGD gels at a density of 1000 cells/cm^2. Cells were allowed to spread and attach for 4 h. After, the cells were imaged every 10 minutes for 6 hours in brightfield and TRITC using a 10x phase objective on an Eclipse TE2000 Nikon microscope and NIS-Elements Software in a humidified 37°C, 5% CO_2 chamber. The ImageJ/FIJI plugin TrackMate was used to track cell movements between each frame and calculate average cell speed and persistence [135–137].

Spheroid encapsulation in HA

Spheroids were harvested from AggreWell plates and suspended into an HA-RGD or HA-only solution of a final concentration of 1.5% (w/w) with a final density of ~625 spheres/ml. Protease-degradable peptide crosslinker with a bifunctional cystine peptide at 10% (w/w) stock (KKCGGPQGIWGQGCKK, Genscript) was then added at a T:M ratio of ~0.24 to generate a shear modulus or ~300 Pa. The mixture was plated as 8 µl droplets into a non-tissue culture-treated plate. The plate was incubated for a total of 1 h in a humidified 37 °C with 5% CO_2 chamber with rotation during the first 10 min to ensure that the spheres would stay in the center of the gels, then left upside-down for the remainder

of the hour. After gelation, fresh cell culture media was added to the wells to fully submerge the gels. Over the duration of the assay, the media was changed every 2-3 days.

Invasion assay imaging and quantification

Spheroids were tracked for 4 days in HA-RGD, 11 days in HA-only, and 24h in collagen using a Plan Fluor Ph1 10x objective on an Eclipse TE2000 Nikon microscope. Spheres within the gel were randomly selected for imaging, with spheres adhered to the bottom of the plate or near the outer edge or surface of the gel excluded from analysis. NIS-Elements Software was used to acquire images. Invasion was quantified using ImageJ by tracing the outermost edge of the spheroid, including any single cells, on day 0 and the corresponding assay end day (day 4 for HA-RGD, day 11 for in HA-only, and day 1/24h for collagen) and calculating the area. The difference between the area of the assay end day and day 0 was then normalized to the day 0 area and reported as relative change in spheroid area. The distance of the farthest cell from the core of the sphere on the assay end day was measured using ImageJ and reported as farthest cell from core sphere edge.

Immunostaining

All steps were performed at room temperature unless otherwise noted. For 3D samples, before the immunostaining and between each step, cells were rinsed 3 times with 5 mins of shaking in PBS. All incubation steps were performed with shaking. The cells were fixed with 4% (v/v) paraformaldehyde for 15 min. Following, the cells were permeabilized and blocked in a solution of 0.1% (v/v) Triton-X and in PBS with 5% (v/v) goat serum for 40 min. The cells were incubated with primary antibodies for 2-3 days at 4°C and then incubated with secondary antibodies, phalloidin, and DAPI for 16 h at 4°C. Stained samples were stored and imaged in 1x PBS. Samples were imaged within a week of staining. Alexa Fluor 546 phalloidin (1:300, Thermo Fisher Scientific) and Alexa Fluor 647 phalloidin (1:30, Cell Signaling Technology), and DAPI (1ng/µl, Sigma Aldrich) were used to visualize the cells.

Imaging

For 3D samples, a Nikon W1 spinning disk confocal with a 10x/0.3NA objective was used for confocal imaging. NIS-Elements software was used to acquire the images.

Protrusion quantification assay

A z-stack of 250 µm thickness with slices 5 µm apart was acquired in the center of each gel. Each z-stack was then collapsed with a maximum intensity projection for analysis. The Image J plug-in SNT was used to trace and measure the length and number of protrusion for each cell in the field of view [138]. Cells that were blurry, too dim, at the edges of the field of view, or were multicellular clumps were excluded from analysis.

Statistical analysis

All graphical representation and statical analyses of the data in this study were performed in GraphPad Prism 10. Unless otherwise noted, data was presented at mean ± SD. The statical comparisons and details of replicates are described in the figure legends.

3.5 Acknowledgements

Some of the experiments and data analysis presented in this chapter was performed by Kwasi Amofa and Miles Duong. Specifically, Kwasi analyzed the data in Figure 3.1 and Miles helped with validation for some of the CRISPR cell lines. Their thoughtful discussion was helpful in analyzing the implications of the results.

Chapter 4: Suppression of cofilin-1 increases migration speed of GBM cells through 3D HA matrices

Vivien D. Tran, Kwasi Y. Amofa, Miles Duong, Sanjay Kumar (2024). Manuscript in preparation.

4.1 Introduction

CFL has been extensively studied and shown to play crucial roles in directing 2D migration. CFL activity status has also been noted as a phenotypic marker of cancer cell invasiveness ([139–141]. We have shown previously that cofilin-1 (CFL), an actin severing protein phospho-inactivated by LIM kinase (LIMK), a downstream effector of the Rho GTPases, is required for front-back polarization of stress fiber networks and formation of organized lamellipodia in 2D motility over rigid surfaces [142]. Our work was motivated in part by studies from Lappalainen and colleagues, who showed that CFL may "prune" low-tension actin bundles from the leading edge, thereby de-selecting these bundles from incorporation into highly contractile stress fibers [143]. In our study, U2OS cells with suppressed CFL expression accumulated low-tension actomyosin filaments (as measured by femtosecond laser ablation) and failed to establish a unified leading edge, implicating CFL in establishing the front-back polarity needed for directional 2D migration [142]. In separate work, we demonstrated that suppression of LIMK 1 and 2 in GBM cells disrupted actin organization and lamellipodia protrusion and dynamics on 2D surfaces, which ultimately also disrupted cell polarization. LIMK1/2 KD cell-based tumors were also less invasive in vivo and produced longer survival times compared to control tumors. This observation was attributed to an overabundance of unphosphorylated CFL and thus increased CFL activity and a deficiency of actin filaments with the cell body [40]. Taken together, the results support the notion that tight regulation of actin turnover is critical for effective 2D migration. However, it is unclear how these mechanisms and more broadly the systems that control cell front-back polarity in 2D govern motility in environments that are not permissive of formation of lamellipodia, i.e. in confined substrates or in 3D ECM [99,120]. As described below, the picture is particularly unclear in 3D matrices that lack directional contact guidance cues, such as fibers.

In this chapter, we sought to confirm and deconstruct the contributions of CFL to 3D GBM invasion to support the results of the CRISPR screen from the previous chapter. Some experiments shown are preliminary, as they require additional replicates, while others have been validated with independent replicates. Studies with targeted shRNA-mediated CFL suppression independently corroborate the 2D and 3D motility observations from the CRISPR and further reveal the effect to be HA-specific, with no increase in motility in 3D collagen or transwell paradigms. Additionally, the effect is also shown to be 3D-specific,

with minimal differences in motility observed in 2D scatter assays. Molecular characterization reveals both filopodial and McTN markers in subsets of protrusions. Together, these results strengthen our proposed model that CFL suppression facilitates invasion by promoting protrusive stabilization through F-actin, which enhances penetration through 3D matrices.

4.2 Results

4.2.1 CFL KD confirms 2D motility phenotype from CRISPR screen

We sought to gain additional mechanistic insight into the role of CFL KO in driving faster 3D motility. While the CRISPR KO system allowed us to efficiently screen multiple targets in parallel, we did not perform clonal selection and therefore were working with a heterogeneous population of edited cells. To introduce a more homogeneous and completely independent system for CFL suppression, we transduced U251 cells with two short hairpin RNAs (shRNAs) (Figure 4.1), both of which reduced CFL expression by >90% relative to controls (Figure 4.1A-B). CFL KD cells had aberrant morphologies compared to NT controls on both fibronectin-coated glass and 2D HA-RGD substrates (Figure 4.1C). CFL KD cells also exhibited less pronounced front-back polarity marked by multiple small lamellipodia (Figure 4.1C-D, G) matching the morphological changes described in our previous study [142]. Furthermore, CFL KD cells migrated less persistently than NT controls in 2D single cell random migration assays on 2D tissue culture plastic and 2D HA-RGD gels (Figure 4.1F, I). Throughout the migration assay, CFL KD cells produced multiple lamellipodia but failed to establish a dominant leading edge or migrate persistently (Figure 4.1D, G), consistent with previous work [142,144]. While neither CFL KD1 nor KD2 showed significantly reduced cell speed on tissue culture plastic (Figure 4.1E), CFL KD1 did show a significant decrease in cell speed compared to NT control on HA-RGD (Figure 4.1H).

4.2.2 CFL KD accelerates 3D motility through HA matrices

To validate our findings from the CRISPR screen of the effects of cofilin depletion on 3D motility, we conducted 3D spheroid invasion assays in HA-only and -RGD gels as described previously. Consistent with CFL KO results from our initial screen, CFL KD cells had significantly increased area change and maximum cell distance after 4 days of invasion in HA-RGD gels compared to NT control cells (Figure 4.2A-C). Likewise, after 11 days in the HA-only gels, CFL KD cells readily migrated through the matrix, with increased area change and maximum cell distance relative to control, signifying that loss of CFL activity through CRISPR-Cas9 KO or shRNA phenocopied one another (Figure 4.2D-F). The NT control cells in the HA-only gels behaved similarly to the NT and NC sgRNA control cells in that they displayed little to no penetration of the surrounding matrix and only exhibited short protrusions at the end of the assay (Figure 4.2D).

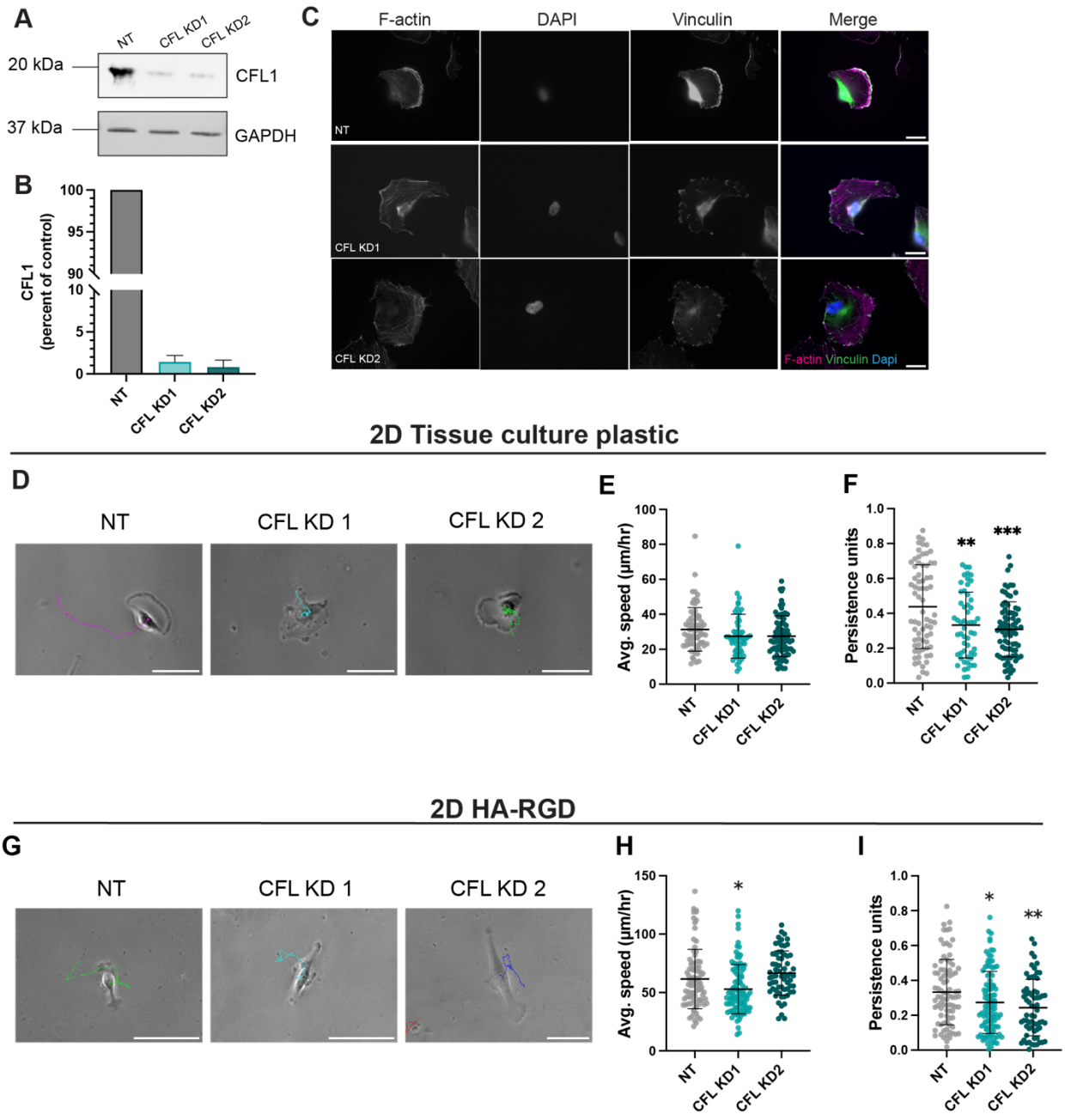

A
NT
CFL KD1
CFL KD2
20 kDa
CFL1
37 kDa
GAPDH
B
CFL1 (percent of control)
100
95
90
10
5
0
NT
CFL KD1
CFL KD2
C
F-actin
DAPI
Vinculin
Merge
NT
CFL KD1
CFL KD2
F-actin Vinculin Dapi
2D Tissue culture plastic
D
NT
CFL KD 1
CFL KD 2
E
Avg. speed (µm/hr)
100
80
60
40
20
0
NT
CFL KD1
CFL KD2
F
Persistence units
1.0
0.8
0.6
0.4
0.2
0.0
**
***
NT
CFL KD1
CFL KD2
2D HA-RGD
G
NT
CFL KD 1
CFL KD 2
H
Avg. speed (µm/hr)
150
100
50
0
*
NT
CFL KD1
CFL KD2
I
Persistence units
1.0
0.8
0.6
0.4
0.2
0.0
*
**
NT
CFL KD1
CFL KD2

Figure 4.1. Validation of CFL KO results with shRNA KD in 2D.
(A) Representative Western Blot showing of CFL expression with NT and CFL KD cell lines, where efficient reduction of CFL expression was achieved with shRNA KD. CFL KD1 and CFL KD2 were cell lines transfected with different shRNA constructs, while NT was transfected with a non-targeting shRNA. (B) Quantification of 3 independent blots with densitometry. Both CFL KD1 and KD2 express <5% of CFL1 protein level of NT control. (C) Representative images of cells cultured on fibronectin-coated glass, stained via IF for F-actin and vinculin. CFL KD results in disorganized lamellipodia and an accumulation of actin filaments. Scale bar: 20 μm. (D) Representative brightfield images of cells during random single migration assays on tissue culture plastic. The colored line represent the migration track of the cell over 25 points and 4.2 hours, with 10 minutes between each point. CFL KD cells had little directional migration and displayed multiple lamellipodia. Scale bar: 40 μm. (E) CFL KD did not decrease cell speed compared to NT control. (F) CFL KD cells migrated with significantly less persistence than NT control. (G) Representative brightfield images of cells during random single migration assays on 2D HA-RGD gels. The colored lines represent the migration track of the cell over 25 points and 4.2 hours, with 10 minutes between each point. CFL KD cells had little directional migration and displayed multiple lamellipodia. Scale bar: 40 μm. (H) Only CFL KD1 showed significantly decreased cell speed compared to NT control. (I) CFL KD cells migrated with significantly less persistence than NT control. In all graphs, error bars represent mean with SD. *P <0.05, **P <0.01, ***P < 0.001 by Kruskal-Wallis test followed Dunn's multiple comparisons test.

We next investigated if the effects of CFL suppression also increased cell motility in stiffer HA matrices. We increased the thiol: monomer ratio of the crosslinker to fabricate gels with higher shear modulus than the previous experiment. After 7 days of invasion in the HA-RGD gels, CFL KD cells had significantly increased area change relative to NT control (Figure 4.3H). Similarly, in the HA-only gels, after 14 days of invasion the CFL KD cells also had significantly increased area change (Figure 4.3J). Although the stiffer matrices resulted in globally slower cell motility, CFL suppression still increased invasion relative to NT control (Figure 4.3G, I).

4.2.3 Deconstruction of CFL contributions to 3D invasion.

While the preceding results demonstrate that CFL suppression enhances 3D motility, there are multiple hypothetical explanations for how this might occur. In the previous chapter, we showed that CFL KO stabilized actin protrusions and potentially enhances 3D motility by allowing better penetration into the surrounding matrix. We queried whether other mechanisms of 3D motility were also enhanced by CFL depletion by employing *in vitro* assays that isolated parts of the 3D motility cycle.

In a previous study, we demonstrated that KD of LIMK1/2 – which increases CFL activation – reduced invasion by impairing the ability of GBM cells to navigate confined

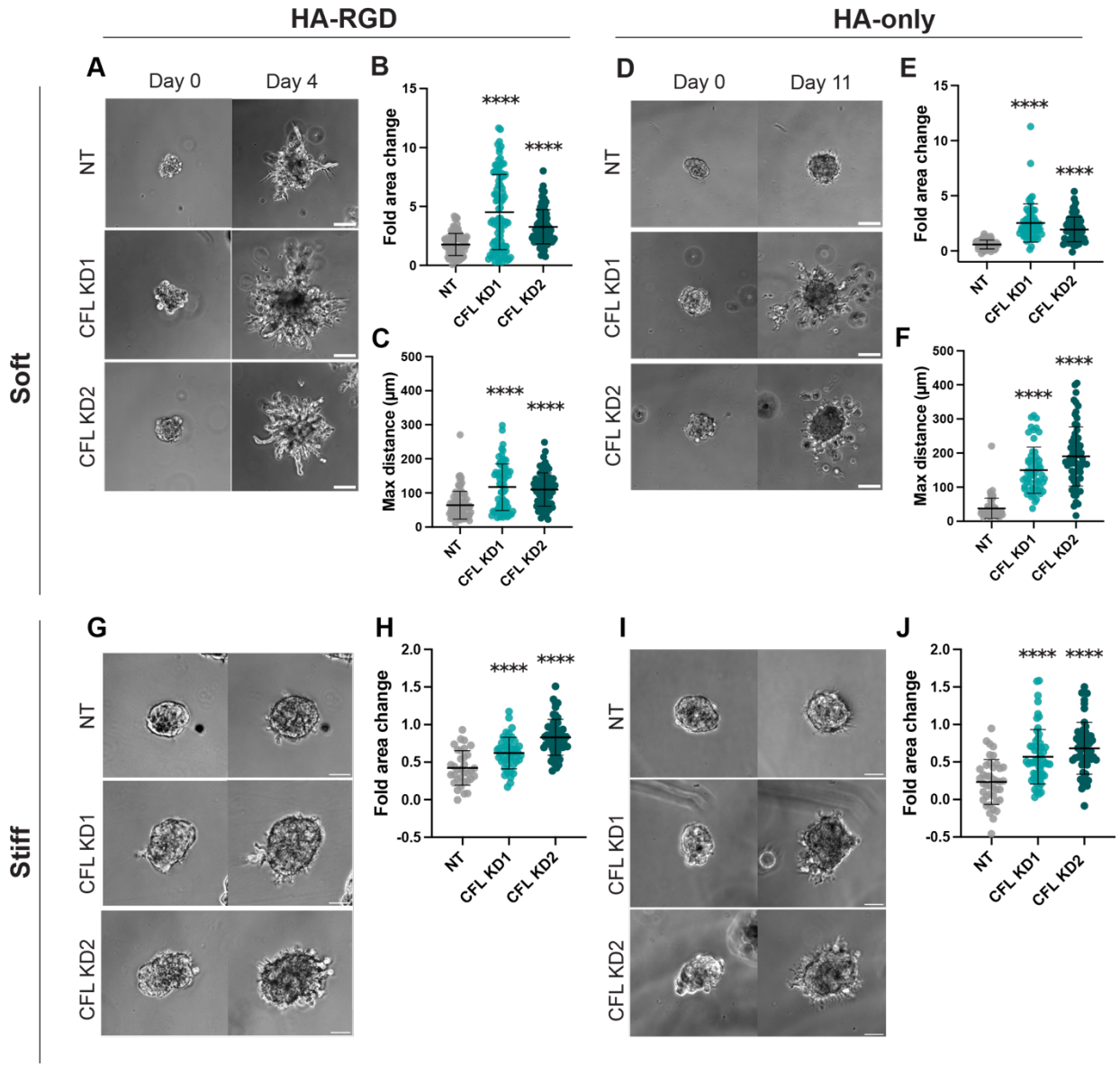


Figure 4.2. Validation of CFL KO results with shRNA KD in 3D.
(A) Representative brightfield images of spheroids at day 0 and day 4 for each cell line in soft HA-RGD gels. (B) Calculated fold area change of day 4 normalized to day 0 area of spheroids. CFL KD1 and KD2 show significant increase compared NT control. (C) Maximum cell distance from the sphere edge. Both CFL KD lines shows significant increase compared NT control. (D) Representative brightfield images of spheroids at day 0 and day 11 for each cell line in HA-only gels. (E) Calculated fold area change of day 11 normalized to day 0 area of spheroids. Both CFL KD cell lines show significantly increased area change compared NT control. (F) Maximum cell distance from the sphere edge. Both CFL KD cell lines show a significant increase compared NT control. (G) Representative brightfield images of spheroids at day 0 and day 7 for each cell line in stiff HA-RGD gels. (H) Both CFL KD cell lines show significantly increased fold area change compared to NT control. (I) Representative brightfield images of spheroids at day 0 and day 14 for each cell line in stiff HA-only gels. (J) Both CFL KD cell lines show significantly increased fold area change compared to NT control. In all graphs, error bars represent mean with SD. ****P < 0.0001 by Kruskal-Wallis test followed Dunn's multiple comparisons test. Scale bar: 100 μm.

environments [40]. This raises the possibility that CFL suppression boosts motility by enhancing the ability to traverse confined spaces inherent in 3D ECMs. To address this possibility in a way that isolates confinement, we conducted Boyden chamber invasion assays using well inserts with 8 μm diameter pores and coated with HA-only. After 4 hours of invasion, there was no significant difference in percentage of cells that migrated through the membrane of the well inserts between NT and CFL KD1 and 2, perhaps indicating that this mechanism is not a key driver in the increase in 3D motility (Figure 4.3A). To further investigate the effects of CFL suppression on confined migration, we also cultured cells on microchannel devices and quantified their morphology (Figure 4.3B). Microchannels have been used previously by us and other labs to model confined migration and measure the elongation factor, or aspect ratio, to determine how well cells navigated the confined topography [40,84,145]. After being cultured overnight in polydimethylsiloxane (PDMS) microdevices with ECM-functionalized channels [84], there appeared to be no noticeable differences between NT and CFL KD cells in aspect ratio and cell area in both 10μm- and 20μm-wide channels (Figure 4.3C-D). While this experiment was only performed with one biological replicate, the preliminary results support that CFL suppression does not enhance confined migration.

Next, we queried if directional migration cues from cell-cell contacts or chemotactic gradients also played a role in the phenotype we observed. To address this possibility in an isolated way, we conducted 2D "scatter" assays in which we deposited cell spheroids onto 2D glass and HA-RGD surfaces and tracked cell trajectories as the cells migrated out and escaped from the spheroid. On 2D glass surfaces, CFL KD did not affect cell speed but did increase persistence for CFL KD1 (Figure 4.3E-F). Similarly, the persistence of the both CFL KD cells were significantly higher than of NT control on the HA-RGD gels, but CFL KD1 displayed significantly lower cell speeds (Figure 4.3I-J). To compare to the 3D migration studies, we also analyzed the scatter assays using similar metrics of relative area change (Figure 4.3G, K) and farthest cell from sphere core (Figure 4.3H, L). For both metrics, CFL KD cells were not significantly different than NT control (Figure 4.3 G-H, ,K-J). As there were minimal differences between NT and CFL KD cells in these isolated studies, the results suggest that CFL suppression majorly increases motility within 3D HA matrices through stabilization of protrusive structures, rather than through other additional mechanisms.

We next queried if CFL suppression would also increase motility in another 3D matrix. The Boyden chamber, scatter, and microchannel assays did not present the same degree of steric barriers to migrating cells as the 3D HA matrices since they are not full 3D matrices. To answer this, we conducted a similar spheroid invasion assay in collagen I gels (Figure 4.3M). After 24 hours, only CFL KD1 had significantly increased area change compared to

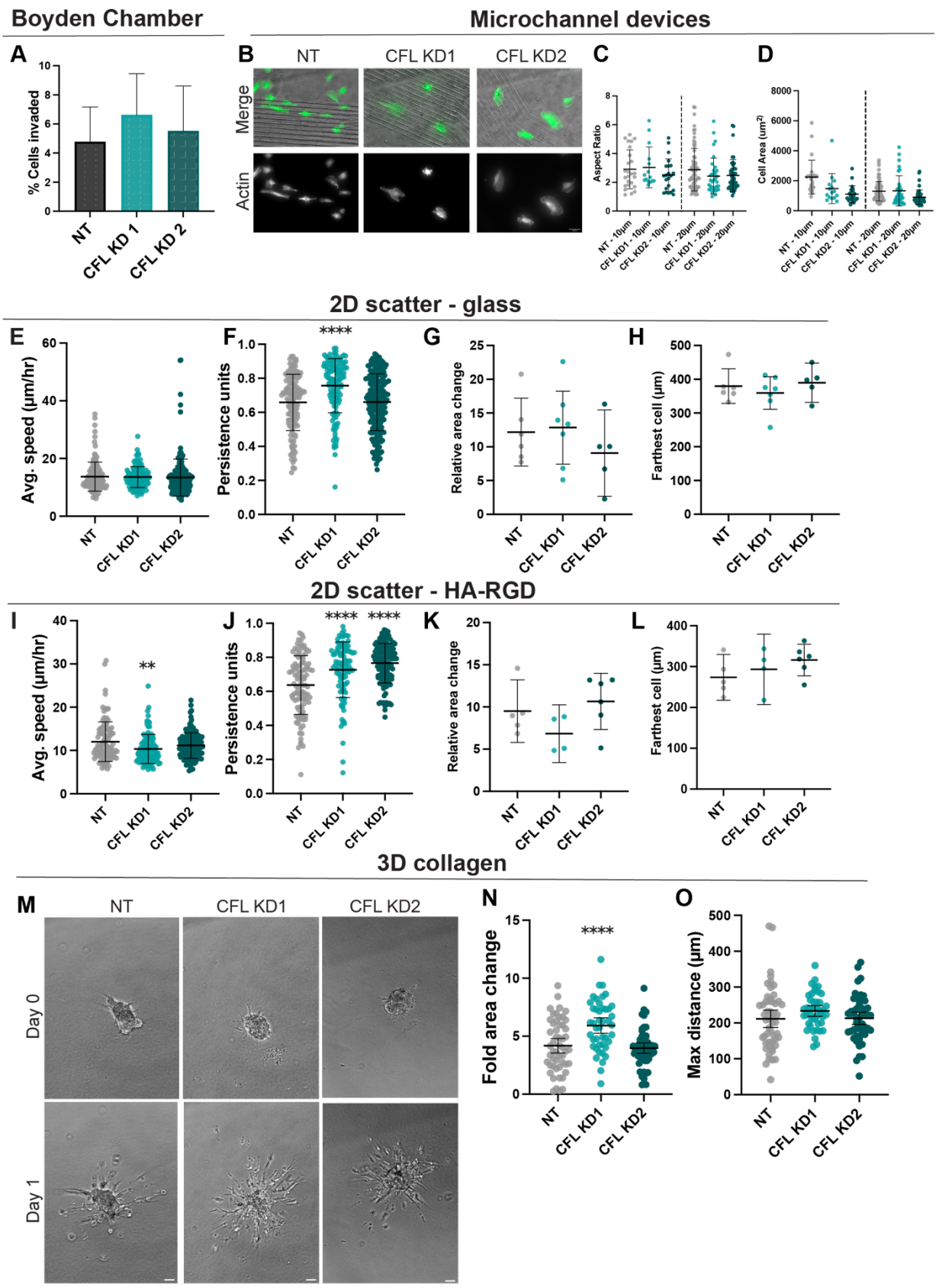

Boyden Chamber
Microchannel devices
A
% Cells invaded
NT
CFL KD 1
CFL KD 2
B
NT
CFL KD1
CFL KD2
Merge
Actin
C
Aspect Ratio
NT - 10µm
CFL KD1 - 10µm
CFL KD2 - 10µm
NT - 20µm
CFL KD1 - 20µm
CFL KD2 - 20µm
D
Cell Area (um²)
2D scatter - glass
E
Avg. speed (µm/hr)
F
Persistence units
****
G
Relative area change
H
Farthest cell (µm)
2D scatter - HA-RGD
I
Avg. speed (µm/hr)
**
J
Persistence units
****
****
K
Relative area change
L
Farthest cell (µm)
3D collagen
M
NT
CFL KD1
CFL KD2
Day 0
Day 1
N
Fold area change
****
O
Max distance (µm)

Figure 4.3. Contextualizing the effects of CFL KD on aspects of 3D motility.
(A) Percent of cells invaded through an 8μm-pore Boyden chamber membrane coated with HA. CFL KD cells did not show a significant increase compared to NT control. Data represents the average of N=5 for each condition. (B-D) Microchannel cell morphology assay. (B) Representative images of cells cultured on the devices. The cells were stained with phalloidin to visualize their morphology Top row is merge of brightfield (gray) and epifluorescent images (green) to show the overlap of cells in the channels. Bottom row is epifluorescent only. Scale bar: 50 μm. (E-L) 2D spheroid scattering assay. Cells were tracked for 46 points over a period of 7.75 hours, with 10 minutes between each point. E-F and I-J represent individual cell measurements from 4-6 spheres, with each sphere being an independent biological replicate. G-H and K-L represent the measurements of each sphere at the end of the assay. (E-F) On glass, when compared to NT control cells, CFL KD cells did not show significantly different speeds, but CFL KD1 exhibited significantly higher persistence. (G-H) The relative area change and farthest cell were not significantly different between CFL KD cells and NT control. (I-J) On 2D HA-RGD, only CFL KD1 cells significantly lowered speeds but had significantly increased persistence compared to NT control. (K-L) The relative area change and farthest cell were not significantly different between CFL KD cells and NT control. (M) Representative brightfield images of spheroids at day 0 and day 1 for each cell line in collagen gels. (N) Calculated fold area change of day 1 normalized to day 0 area of spheroids. Only CFL KD1 spheres show significant increase compared to NT control. Scale bar: 100 μm. (O) Maximum cell distance from the sphere edge. CFL KD cells did not show a significant increase compared to NT control. In all graphs, error bars represent mean with SD. **P <0.01, ***P < 0.001 by Kruskal-Wallis test followed Dunn's multiple comparisons test.

NT control (Figure 4.3N) and both CFL KD1 and KD2 did not have significantly increased maximum distance (Figure 4.3O). Since the cell invasion through collagen (24 hours) is much faster than through the HA matrices (4-11 days), contributions from CFL KD to invasion through the collagen matrix could be obscured and explain the heterogeneity between the CFL KD cell lines. Additionally, collagen matrices contain larger pore sizes than HA matrices, so the contributions of protrusive structures to navigate the steric barriers of the matrix may be limited in comparison. Considering the mixed results from the 3D collagen invasion assay, we concluded that CFL KD only enhances migration speed through HA-based matrices.

4.2.4 Protrusions contain markers of microtentacles and filopodia irrespective of CFL status
In our initial screen (Figure 3.1), we showed that CFL KO increased the number and length of cellular protrusions. We next asked if these increased protrusions also showed molecular composition differences compared to NT. To characterize the protrusions, we used immunofluorescence to probe for McTN and filopodia markers [108,122,146]. We applied a similar protrusion formation assay as in the CRISPR screen, seeding the cells as single cells into HA-only and HA-RGD gels. For this assay, we allowed the cells to form protrusions for 7 days to ease characterization. In both matrix conditions, we observed that protrusions in both NT and CFL KD cells were all positive for CD44 and HYAL2 (a hyaluronidase ubiquitously expressed by GBM cells) (Figure 4.4A-B, D-E), indicating that the protrusions could adhere to and degrade the HA matrix, like our previous description of McTNs and reminiscent of invadopodia. When probing for the filopodial marker myosin

10 (MyoX), both NT and CFL KD protrusions in the HA-only matrix displayed minimal expression, indicating that they are closer to McTNs than filopodia (Figure 4.4C). In the HA-RGD matrix, all cells displayed heterogeneous expression of MyoX in protrusions (Figure 4.4F). Cells that had shorter or less protrusions displayed little to no MyoX-protrusions, while cells that had longer and or more protrusions had many MyoX-positive protrusions. This observation indicates that in the 3D HA-RGD matrix, the protrusions display a mix of McTN and filopodial characteristics. Thus, while CFL KD increases protrusion number and length, it does not appear to fundamentally change protrusion composition.

4.3 Discussion and conclusions

While the role of CFL in 2D motility has been extensively studied, how CFL contributes to 3D motility, especially in non-fibrillar matrices such as HA, is not well known. In this chapter, we investigated the role of CFL to 3D invasion of GBM cells through HA. We independently confirmed our results from the CRISPR screen in the previous chapter with targeted shRNA KD but could not recapitulate the result in 3D collagen or Boyden chamber invasion assays, pointing to the specificity of this result to migration through a 3D nanoporous matrix. Mechanistic studies revealed that protrusions seen in the setting of CFL suppression include F-actin along with both McTN and filopodial markers. Our data supports a model in which attenuated CFL activity stabilizes actin within a variety of protrusions and enhances the ability of GBM cells to migrate through HA. The protrusions express HYAL2, implicating that these protrusions are also involved in HA degradation and thus permit GBM cell invasion, mirroring the role of invadopodia and matrix-metalloproteinases in 3D motility.

How the components involved in actin turnover, including the LIMK/CFL pathway, contribute mechanistically to cell motility varies with matrix context [120]. In 2D, attenuating CFL expression and activity, either directly or through LIMK overexpression, altered lamellipodial actin networks and decreased directional motility [139,142,144,147–149]. Reciprocally, overexpression of WT CFL and constitutively active CFL mutants enhanced the motility of GBM cells [149,150]. However, diminishing LIMK expression or activity and increasing the amount of activated CFL was shown to negatively affect 2D motility in chemokine-stimulated migration [151–153]. This dichotomy is also seen in 3D cell motility and cancer invasion, in that CFL and its regulators are seen as both positive and negative factors in migration. Diminished CFL expression reduced motility of T cells in collagen and Matrigel [154,155] and invasion of tumor cells in Boyden chamber assays [149,153]. In our study, attenuating CFL activity increases motility speed through 3D HA.

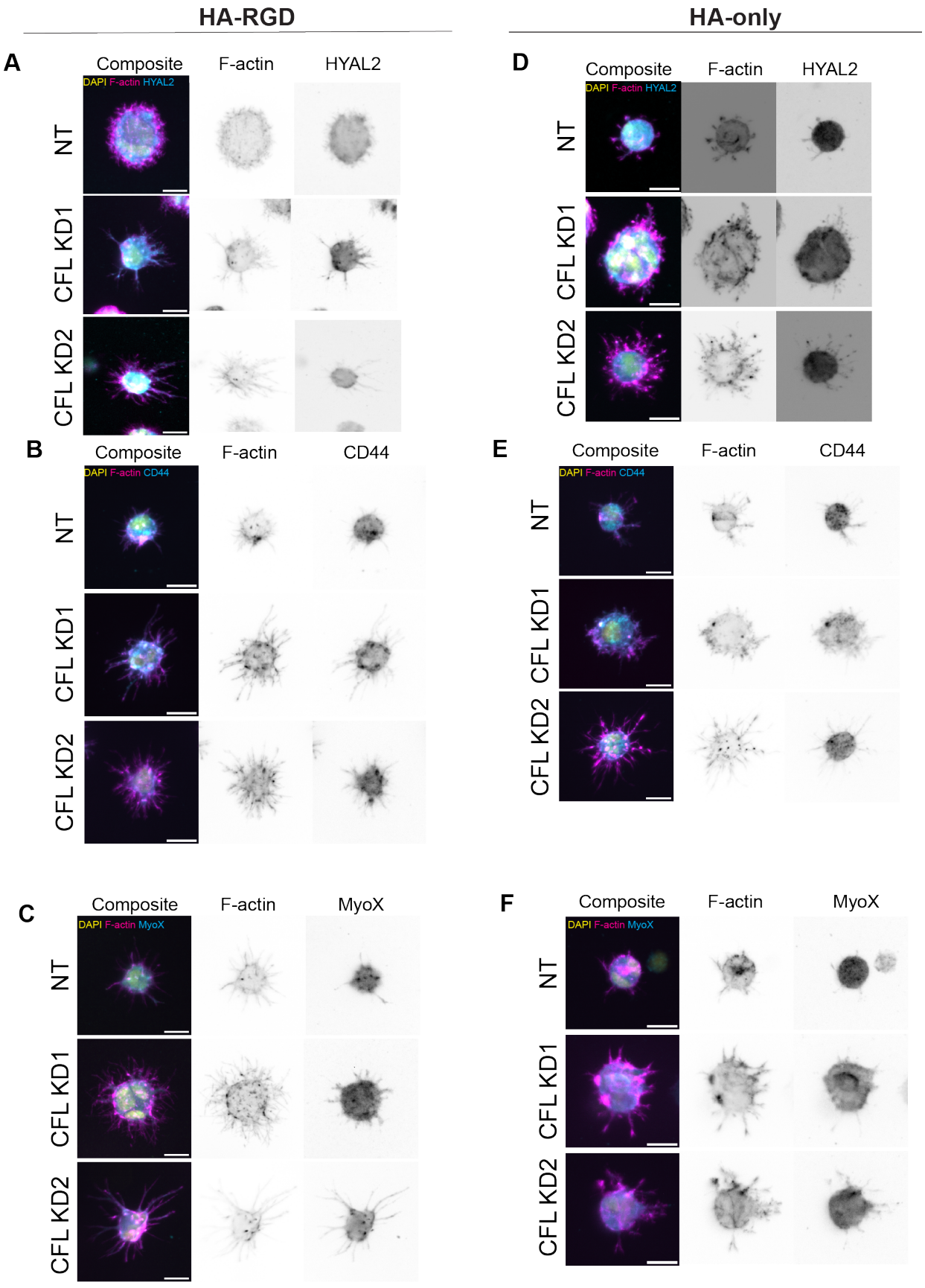

HA-RGD
HA-only
A
Composite
F-actin
HYAL2
DAPI F-actin HYAL2
NT
CFL KD1
CFL KD2
D
Composite
F-actin
HYAL2
DAPI F-actin HYAL2
NT
CFL KD1
CFL KD2
B
Composite
F-actin
CD44
DAPI F-actin CD44
NT
CFL KD1
CFL KD2
E
Composite
F-actin
CD44
DAPI F-actin CD44
NT
CFL KD1
CFL KD2
C
Composite
F-actin
MyoX
DAPI F-actin MyoX
NT
CFL KD1
CFL KD2
F
Composite
F-actin
MyoX
DAPI F-actin MyoX
NT
CFL KD1
CFL KD2

Figure 4.4. Cells in the HA matrices display F-actin-based protrusions with both McTN and filopodial markers.

(A,D) Most protrusions are positive for HYAL2, indicating HA matrix-degradation capabilities. (B,E) Most protrusions are also CD44-positive and thus can interact with the surrounding matrix. (C,F) Protrusions show heterogeneous expression of MyoX, with cells in HA-RGD having more MyoX-positive protrusions than in HA-only. In all composite images, yellow is DAPI, magenta is F-actin, and cyan represented the marker being probed for. Scale bar: 20μm.

The relationship between CFL activity and 3D migration has proven surprisingly complex, with the end effect depending on the biological system and method of perturbation. Suppression of CFL activators chronophin (CIN) and slingshot 1 and 2 (SSH) is expected to decrease CFL activation but appears to impact migration in different ways. SSH KD decreased the invasive capability of T cells and hepatoma cells [151,153], while CIN KD increased the in vitro invasive capability of GBM cells [156]. LIMK inhibition has been shown to slow cancer cell migration and invasion in both *in vitro* and *in vivo* studies by disinhibiting CFL [40,105,157–159]. It is possible that CFL activity is tuned to some optimum whose value depends strongly on the context [139,140]. This idea is consistent with the observation that LIMK/CFL pathway expression and activity varies with cell type [160,161] and the fact that 3D migratory mode is strongly regulated by matrix properties [2,99,162]. If an optimum indeed exists, the differential effect of CFL suppression on 2D vs. 3D migration suggests that this value depends strongly on matrix dimensionality, with greater actin stability needed to overcome steric barriers inherent to nanoporous 3D matrices. In future work, it would be fruitful to repeat the studies with other routes of CFL activity modulation, such as using SSH or CIN KD cells or using a phospho-null mutant CFL. Since this study directly decreased expression of CFL, it would increase our understanding of the CFL activity pathway to see if attenuating CFL activity rather than expression would yield similar phenotypes.

Using an engineered HA hydrogel platform, we examine the contributions of CFL to GBM cell motility in 3D HA matrices. We confirmed through targeted KD that CFL suppression speeds up 3D motility. We further dissect the mechanism of the enhanced 3D motility and find that CFL suppression only facilitates 3D motility through stabilization of the protrusions and not through other mechanisms. In future studies, it would also be valuable to capture the dynamics of the protrusions observed in this study at high spatial and temporal resolution during 3D migration, ideally taking advantage of superresolution tools and new reagents for localized modulation of CFL in subcellular compartments [163]. While we showed that the differential effect of CFL suppression holds in HA but not collagen I, it will be important in the future to explore a much wider range of matrix types exhibiting a diversity of adhesive, microstructural, and mechanical properties. Additional studies in organotypic models (e.g. brain slice culture) should also complement and lend

new mechanistic insight into the wealth of studies focused on the role of CFL in migration *in vivo*, especially those focused on the role of CFL in motility within tissue [110,139,141,149,164]. Our work provides insight into the contributions of CFL within protrusions and 3D motility and opens new mechanistic questions to explore.

4.4 Methods

All key resources are listed in Supp. Table A1.

Cell culture

U251 cells were obtained from the University of California, Berkeley Tissue Culture Facility. The cells were cultured in Dulbecco's modified Eagle's medium (DMEM, Gibco) supplemented with 10% (v/v) fetal bovine serum (FBS; JR Scientific), 1% (v/v) non-essential amino acids (Gibco), 1% (v/v) sodium pyruvate (Thermo Fisher Scientific), and 1% (v/v) penicillin/streptomycin (Gibco). Cells were passaged every ~7 days with media changes every other day and harvested using 0.25% trypsin-EDTA (Thermo Fisher Scientific). Cells were passaged less than 30 times and were screened every three months for myocoplasma. All U251 cells transduced with shRNA expression plasmids were maintained in 1 µg/ml puromycin (Clontech).

CFL shRNA KD cell line generation

U251 CFL shRNA KD cells were generated using methods as previously described [142]. Briefly, shRNA constructs targeting the human cofilin-1 isoform (CFL KD1: 5′-ACGACATGAGGTGCGTAAGT-3′, CFL KD2: 5′-AAGGAGGATCTGGTGTTTATC-3′) and a non-targeting sequence (NT: 5′-GCTTCTAGCCAGTTACGTACA-3′) were cloned into the pLKO.1-TRC cloning vector (Addgene 10878) using AgeI and EcoRI [165]. pLKO.1-TRC was a gift from David Root. Lentivirus particles were produced using HEK 293T cells using second generation packaging plasmids (pMD2.G; psPAX2, Addgene 12260) for each construct. U251 cells were transduced with shRNA viral particles at a MOI of 1. After 48 h post-transduction, cells were selected using 2 µg/ml puromycin for 1 week for shRNA integration. Knockdown efficiency was assessed via Western Blot.

Generation of spheroids

U251 cell spheroids were generated using AggreWell 400 plates (STEMCELL Technologies). Briefly, the wells of the AggreWell plate were incubated with an anti-adherence rinsing solution (STEMCELL Technologies) then washed with fresh media. U251 cells were seeded as single cells at a density of ~3 x 10^5 cells per well. Cells were allowed to grow and aggregate into spheres for 4 days. The spheres were then harvested and used for assays.

HA synthesis and RGD conjugation

HA hydrogels were fabricated as described previously [108,114]. Briefly, sodium hyaluronate (Lifecore Biomedical, Research Grade, 66 kDa - 99 kDa) was functionalized with methacrylic anhydride (Sigma-Aldrich, 94%) to synthesize methacrylated HA (HA-Me). The extent of methacrylation per disaccharide was quantified with ^{1}H NMR as described previously and calculated to be approximately 85% for the HA-Me used in this study [114]. To add integrin-binding motifs, HA-Me was conjugated with RGD peptide Ac-GCGYGRGDSPG-NH2 (Anaspec) at a concentration of 0.5 mmol/L via Michael Addition. Crosslinker details are described in the 2D gel fabrication and 3D spheroid encapsulation sections below.

2D gel fabrication

Prior to gel fabrication, glass-bottom plates were coated with 1mg/ml poly-d-lysine solution (Sigma-Aldrich) and rinsed with 1x PBS (Fisher BioReagent) to enable gel adsorption to the glass. Phenol-free DMEM (Thermo Fisher Scientific) and HA-RGD solution at 6% (w/w) stock were mixed to generate a final concentration of HA-RGD of 5% (w/w). Bifunctional thiol dithiothreitol at 5% (w/w) stock (DTT, Thermo Fisher Scientific) was then added at thiol:HA monomer repeat (T:M) ratio of ~0.4 to achieve an shear modulus of ~6.5 kPa. The solution was plated at 6 µl per gel into the treated glass-bottom plates, then flattened with a plasma-treated glass coverslip, creating flat gels of ~120 µm in height. The flattened gels were incubated for 1 h in a humidified 37 °C chamber. Once the gels were cross-linked, the coverslips were removed and the gels were soaked in room temperature PBS overnight before cell seeding.

2D migration assay

Prior to seeding, U251 cells were incubated with SPY555-DNA (Cytoskeleton) at a final concentration of 1:1000 dilution for 24 h to visualize the nucleus. For single cell migration, cells were seeded onto tissue culture plate wells or HA-RGD gels at a density of 1000 cells/cm^2. For spheroid scattering assay, spheres were collected and seeded onto HA-Me-coated glass or HA gels at a density of 1-2 spheres per 12 mm-diameter well. Cells were allowed to spread and attach for 4 h. After, the cells were imaged every 10 minutes for 6 hours in brightfield and TRITC using a 10x phase objective on an Eclipse TE2000 Nikon microscope and NIS-Elements Software in a humidified 37°C, 5% CO_2 chamber. The ImageJ/FIJI plugin TrackMate was used to track cell movements between each frame and calculate average cell speed and persistence [135–137].

Spheroid encapsulation in HA

Spheroids were harvested from AggreWell plates and suspended into an HA-RGD or HA-only solution of a final concentration of 1.5% (w/w) with a final density of ~625 spheres/ml. Protease-degradable peptide crosslinker with a bifunctional cystine peptide

at 10% (w/w) stock (KKCGGPQGIWGQGCKK, Genscript) was then added at a T:M ratio of ~0.24 to generate a shear modulus or ~300 Pa. For the stiffer gels, the peptide crosslinker was added at a T:M ratio of ~0.275 to generate a shear modulus of ~700 Pa. The mixture was plated as 8 µl droplets into a non-tissue culture-treated plate. The plate was incubated for a total of 1 h in a humidified 37 °C with 5% CO_2 chamber with rotation during the first 10 min to ensure that the spheres would stay in the center of the gels, then left upside-down for the remainder of the hour. After gelation, fresh cell culture media was added to the wells to fully submerge the gels. Over the duration of the assay, the media was changed every 2-3 days.

Spheroid encapsulation in collagen

Spheroids were harvested from AggreWell plates and suspended into a gel precursor solution comprised of bovine collagen type I solution (Advanced Biomatrix), 1N NaOH (Fisher Scientific), and 1 N HEPES (Life Technologies) to generate a 2 mg/ml final collagen concentration with a density of ~625 spheres/ml. The mixture was then plated as 5 µl droplets into a non-tissue culture-treated plate that was treated with 1mg/ml poly-d-lysine solution. The plate was incubated for a total of 1 h in a humidified 37 °C chamber with 5% CO_2, with rotation during the first 10 min to ensure that the spheres would stay in the center of the gels, then left upside-down for the remainder of the hour. After gelation, fresh cell culture media was added to the wells to fully submerge the gels.

Invasion assay imaging and quantification

Spheroids were tracked for 4 days in HA-RGD, 11 days in HA-only, and 24h in collagen using a Plan Fluor Ph1 10x objective on an Eclipse TE2000 Nikon microscope. Spheres within the gel were randomly selected for imaging, with spheres adhered to the bottom of the plate or near the outer edge or surface of the gel excluded from analysis. NIS-Elements Software was used to acquire images. Invasion was quantified using ImageJ by tracing the outermost edge of the spheroid, including any single cells, on day 0 and the corresponding assay end day (day 4 for HA-RGD, day 11 for in HA-only, and day 1/24h for collagen) and calculating the area. The difference between the area of the assay end day and day 0 was then normalized to the day 0 area and reported as relative change in spheroid area. The distance of the farthest cell from the core of the sphere on the assay end day was measured using ImageJ and reported as farthest cell from core sphere edge.

Boyden chamber assay

Boyden chamber inserts with pore sizes of 8 µm (Sterlitech), were incubated with 1.5% (w/w) HA-me diluted in PBS overnight at 4°C, then rinsed 3 times with PBS. Cells were seeded into the top of each insert at a density of 28k cells/cm^2 in media containing 1% FBS. The bottom chamber was filled with media containing 10% FBS to create a chemotactic gradient. Cells were allowed to migrate for 4 h, then fixed with 4%

paraformaldehyde for 10 min and washed 3 times with PBS. The cells were permeabilized with 0.5% Triton-X for 10 min and then stained with DAPI (Sigma-Aldrich) for 10 min. The inserts were imaged with an Eclipse TE2000 Nikon microscope and NIS-Elements software. Cell nuclei were counted using a Python-based custom code modified from a previous study [166].

Microchannel assay

Silicon masters used in this study were previously fabricated using established lithography methods [40]. PDMS microchannel devices were fabricated as previously described [40,84]. Briefly, Sylgard 184 base and curing agent (Krayden Inc) were added together in a 10:1 ratio then thoroughly mixed by stirring. The solution was degassed for 1 h and poured over the silicon master at a thickness of ~ 2 mm. The PDMS devices were cured at 80°C for 3 hours, then cut out using a razor blade. The cut devices were then affixed to tissue culture dishes with sterile vacuum grease.

Cells were seeded onto the devices and allowed to adhere overnight. The devices were then fixed with 4% (v/v) paraformaldehyde for 15 min and stained with phalloidin to visualize the cell morphology (detailed methods found in the following Immunostaining section).

Immunostaining

All steps were performed at room temperature unless otherwise noted. For 2D samples, before the immunostaining process and between each step, cells were rinsed briefly with PBS. The cells were fixed with 4% (v/v) paraformaldehyde (Alfa-Aesar) for 10 min. Following, the cells were permeabilized with 0.3% (v/v) Triton-X (Sigma-Aldrich) in PBS for 10 min, then blocked with 5% (v/v) goat serum (Thermo-Fisher) in PBS for 1 h. The cells were incubated with primary antibodies for 16 h at 4°C, then incubated with secondary antibodies, phalloidin (647- Cell Signaling Technology, 546 - Thermo Fisher Scientific), and DAPI (Sigma-Aldrich) for 1h. The cells were then mounted using Fluoromount-G (Fisher Scientific). Samples were imaged within a week of staining.

For 3D samples, before the immunostaining and between each step, cells were rinsed 3 times with 5 mins of shaking in PBS. All incubation steps were performed with shaking. The cells were fixed with 4% (v/v) paraformaldehyde for 15 min. Following, the cells were permeabilized and blocked in a solution of 0.1% (v/v) Triton-X and in PBS with 5% (v/v) goat serum for 40 min. The cells were incubated with primary antibodies for 2-3 days at 4°C and then incubated with secondary antibodies, phalloidin, and DAPI for 16 h at 4°C. Stained samples were stored and imaged in 1x PBS. Samples were imaged within a week of staining.

The following primary antibodies were used for immunostaining at a dilution of 1:200: rabbit anti-cofilin (Cell Signaling Technologies), mouse anti-vinculin (Sigma-Aldrich), rabbit anti-myosinX (Sigma-Aldrich), rabbit anti-CD44 (Invitrogen), and rabbit anti-HYAL2 (Abcam). The following secondary antibodies were used: Alexa Fluor 488 anti-mouse and Alexa Fluor 647 anti-rabbit, both used at a dilution of 1:500 and from Thermo Fisher Scientific, along with Alexa Fluor 546 phalloidin (1:300, Thermo Fisher Scientific) and DAPI (1ng/µl, Sigma Aldrich).

Imaging

For 2D samples, an Eclipse TE2000 Nikon microscope with a 60x objective and a LED lamp were used for epifluorescence imaging. NIS-Elements software was used to acquire the images.

For 3D samples, a Nikon W1 spinning disk confocal with a 10x/0.3NA objective was used for confocal imaging. NIS-Elements software was used to acquire the images.

Western Blot analysis

Cells grown on tissue culture plates were lysed using RIPA buffer (Sigma-Aldrich) supplemented with Halt protease and phosphatase inhibitor cocktail (Thermo Fisher Scientific). Samples were run on a 4-12% Bis-Tris gel (Life Technologies), with equal amounts of protein loaded into each lane (~20 µg), then transferred to a nitrocellulose membrane (Licor). Membranes were probed with rabbit anti-cofilin antibody (Cell Signaling Technology) and mouse anti-GAPDH (Sigma-Aldrich). Blots were then probed with the secondary antibodies Alexa Fluor 488 goat anti-mouse (Thermo Fisher Scientific) or Alexa Fluor 647 goat anti-rabbit (Thermo Fisher Scientific) for visualization. Primary antibodies were used at a dilution of 1:1000 and secondary antibodies were used at a dilution of 1:10,000. Membranes were imaged using the iBright imaging system (Invitrogen).

Statistical analysis

All graphical representation and statical analyses of the data in this study were performed in GraphPad Prism 10. Unless otherwise noted, data was presented at mean ± SD. The statical comparisons and details of replicates are described in the figure legends.

4.5 Acknowledgements

Some of the data analysis in this chapter were conducted by Kwasi Amofa. Specifically, he analyzed the data shown in Figure 4.2. His thoughtful discussions were helpful for interpreting the data and implications of the work.

Chapter 5: Conclusions

5.1 Summary

Cell migration is a central part of many biological processes and has mostly been studied in the context of flat, 2D matrices. While studies performed on 2D have given foundational and tremendous insight into the mechanisms of cell migration, how those mechanisms translate to a 3D biomimetic context has not been fully characterized. This works focuses on the role of actin regulation in 3D motility and how changes in dimensionality and geometry may affect actin regulation. First, through a CRISPR screen of core actin turnover proteins, we identified that CFL suppression uniquely enhances migration speed through 3D HA matrices by increasing both the number and length of actin-based protrusions. We hypothesized that the loss of CFL activity stabilizes the actin filaments within protrusions, boosting the penetration and invasion of the surrounding matrix. Secondly, we confirm the observations through targeted CFL KD and find that this result is specific to 3D nanoporous matrices, and that CFL suppression does not enhance confined migration or chemotaxis. Additionally, loss of CFL seemingly only stabilizes protrusions and does not change protrusion architecture. Taken together, this work increases understanding of the CFL pathway to cell motility in tissue-like geometries and provide insight into the molecular mechanisms of the CFL pathway in GBM invasion.

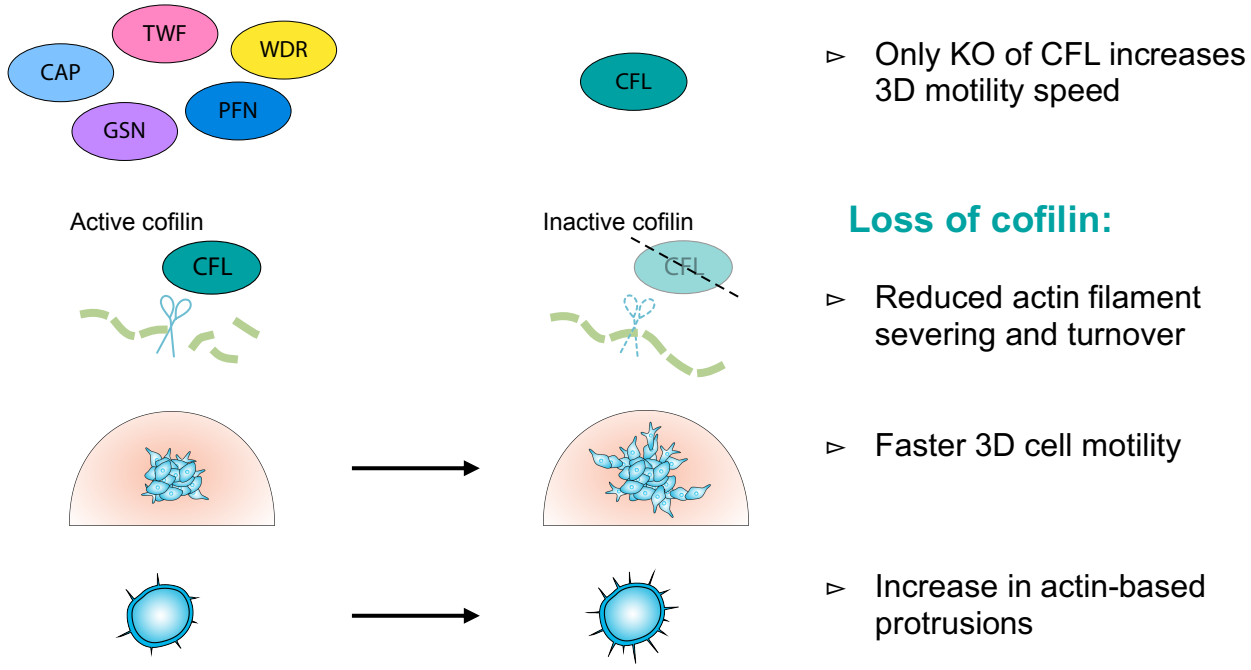


Figure 5.1. What role does actin turnover play in 3D (GBM) motility?

A summary of the key findings from this work.

5.2 How do the actin turnover proteins contribute to 3D migration in HA matrices?

The first part of this work sought to characterize the contributions of actin turnover proteins to cell migration through non-fibrillar, tissue-mimetic matrices, specifically using a model of GBM invasion through engineered HA matrices. We surprisingly found that CFL suppression uniquely augmented 3D motility speed and increased both the length and number of protrusions. Additionally, we showed that CFL suppression had opposing effects on 2D and 3D migration. This opens new mechanistic questions regarding CFL activity and actin regulation in 3D compared to 2D migration. Since CFL activity seems to be not as necessary for or impeding 3D motility, it would be fruitful to investigate if CFL activity is downregulated in 3D motility versus 2D motility by quantifying the phospho-CFL levels between the two migration modes.

Another insight from this work is that the specific loss of CFL, rather than of cofactors, is necessary to significantly increase 3D cell motility. Suppression of CAP and WDR, proteins that both have roles in promoting CFL-driven actin filament turnover, did not show significant increases in 3D motility compared to NT control, highlighting the specificity of the CFL KO [167,168]. While previous work has shown that CAP suppression reduces actin filament turnover, similar to CFL suppression, the degree to which actin turnover is decreased is perhaps not enough to increase 3D motility speed [168]. Follow-up work with suppression of other proteins that modulate CFL activity, like CFL activators SSH and CIN, could clarify if diminished CFL dephosphorylation would attenuate actin turnover enough to increase 3D motility.

Another open question from this work is why CFL is the only target to show a such a large difference from the control and a stark difference between 2D and 3D motility. While some of the other target KOs showed a significant decrease in 2D cell speed (PFN, TWF, WDR) or 3D motility metrics (TWF, WDR), only CFL KO showed a significant decrease in 2D cell speed and increase in 3D motility metrics. We hypothesized that this may be due to the unique role that CFL plays in actin severing [125–127]. Future work could shed insight on this question by investigating the effects of each target protein KO on actin turnover and protrusion dynamics. Most of the proteins in the screen are known to have roles in the formation (CAP, PFN) or disassembly (CFL, GSN, TWF) of well characterized actin-based protrusions like filopodia and invadopodia [124,169–171]. While the protrusions in our study are not well characterized and defined, their mechanisms of assembly and disassembly are likely similar to those of other actin-based protrusions. Future work could take advantage of live actin and tubulin dyes to capture the dynamics within protrusions and also quantify the temporal stability of the protrusions in each cell line. It would also be fruitful to further characterize the protrusions in our study by tracking

the localization of each target within the protrusions, ideally taking advantage of constructs for localized modulation of protein activity like z-lock CFL [163].

Another area of possible follow-up experiments would be to characterize the effects of suppression of the proteins in the screen on protrusion function and composition. In this assay, we only quantified the length and number of protrusions per cell; in future work it would be helpful to also observe if suppression of the protein targets also affects the molecular composition of the protrusions. Similar to the immunofluorescence assay performed in Chapter 4 of this work, future work could stain for filopodial and microtentacle markers. Additionally, matrix degrading assays like gelatin-degration invadopodia assays or HA staining post-invasion could assess the effects of suppression of the protein targets on protrusion function. Further assays to characterize the function of the protrusions are discussed in the next section.

Additional future work could investigate the proteins in more physiological models of cancer invasion that would present additional cues which may affect motility. For example, our lab has designed an in vitro platform, known as the microchannel device, to model the parenchymal to perivascular transition of GBM invasion, and it has been used to screen for genetic drivers of GBM invasion [119,172]. The device consists of a bulk HA gel section, modeling the dense parenchyma, and a basal media-filled channel that represents the perivascular niche. In regard to this study, the microchannel device is of interest because of the ability to isolate the parenchymal to perivascular invasion mode transition and model another mode of 3D motility. The transition requires coordinated morphology changes from the invading cells, so it would be logical to assume that the actin cytoskeleton and actin-regulating proteins would play a major role. This platform can be used in future work to screen the targets from this study with CRISPR KO to investigate their contributions to the transition. The platform has two places for quantification: 1) how well or how fast does each cell line transition between the parenchyma to the perivascular space, and 2) how fast does each cell line invade along the perivascular channel. If suppression of a target results in an inability to transition between the invasion modes, this might signal that the target protein plays an integral role in cells' plasticity and ability to adapt to different geometries. Similarly, if a target protein KO results in slower or lack of perivascular invasion, this would suggest that the protein is integral to the perivascular invasion mode. On the other hand, if suppression of a target results in faster invasion mode transition or perivascular invasion, then this would imply that the target protein somehow hinders either process.

Lastly, examining the target proteins in matrices with differing physical properties or composition would inform how the results from this matrix could translate to other matrices. For example, future work could measure the invasion of the KO cell lines in high

molecular weight HA (HMW-HA) gels or collagen gels. The gels used in this study utilize low molecular weight HA (LMW-HA). Using HMW-HA would change the degree of viscoelasticity of the matrix and allow for examination of the contributions of the target proteins to motility through a 3D viscoelastic matrix. With collagen gels, future work would test how our results would translate to a matrix with a microporous structure and no CD44 interaction.

5.3 What are the contributions of CFL to 3D GBM motility?

The CRISPR screen from the first part of our work revealed that CFL suppression uniquely enhanced 3D but not 2D motility in HA matrices. While the CRISPR-Cas9 system was used for efficient inhibition of multiple targets in parallel, it did produce a heterogeneous pool of KO cells for each target, including CFL. Our follow-up study in the second part of our work aimed to validate the results from the screen and further explore the mechanistic contributions of CFL suppression to 3D GBM motility. This work represents one of the first studies to examine the role of actin turnover and CFL in motility through a non-fibrillar and defined matrix. While this work utilized biomimetic HA gels, as proposed previously, it would be valuable to confirm this phenotype in more physiological conditions (e.g. *ex vivo* brain tissue slices or xenograft models). The results from these assays would give insight into how well findings from simplified *in vitro* models translate to *in vivo* settings.

One of the findings to emerge from this work is that this effect is seemingly HA-specific and mainly acts through the stabilization of protrusions. This may point to an HA-specific mechanism, perhaps acting through CD44. Using CD44 KO cells or CD44 inhibition would reveal if this mechanism is CD44-dependent. CD44 is known to bind to the actin cytoskeleton via the ERM family proteins and IQGAP1, and previous work from our lab has shown that IQGAP1 is essential for cell adhesion and McTN formation on HA matrices [108,173–175]. Considering the links between CD44 and the actin cytoskeleton, it would be fruitful to investigate if stabilization of actin filaments from CFL suppression affects CD44 adhesion, quantified via a centrifugal adhesion assay [108,115]. If adhesion is increased, it would imply that the protrusions also promote invasion via heightened adhesion to the matrix.

In this work, we proposed that CFL suppression enhanced 3D motility through stabilization of actin filaments within protrusions. To further understand how CFL suppression stabilizes the filaments, as discussed previously, it would be fruitful to observe the dynamics of the protrusions and localization of cofilin within the protrusions using live cell imaging. For example, utilizing recently developed tools for localized modulation of CFL activity, future work could probe the temporal effects of local activation or deactivation of CFL on protrusion dynamics [163]. Previous work has shown that CFL activity defines the leading edge of cells migrating in 2D; it would valuable to dissect the

mechanisms of CFL localization in 3D motility to contribute to a better understanding of leading edge dynamics in 3D [141,142].

While we postulated that the enhancement from stabilized actin filaments is a result of increased penetration through the surrounding steric barriers of the ECM, there could also be other changes within the protrusions that bolster 3D motility. Namely, we did not investigate if CFL suppression affected the matrix digesting capabilities or traction forces of the protrusions. Since our results have shown the protrusions to have a combination of filopodial and microtentacle markers, it is reasonable to assume that they have matrix-digesting capabilities. To confirm this, future work could visualize the surrounding HA matrix and quantify if CFL suppression also enhances the HA matrix digestion. Should there be a difference in the degree of HA digestion around the protrusions of CFL KD versus NT control, then it would imply that attenuating CFL activity also bolsters hyaluronidase activity. Another way to investigate the effects of CFL suppression on HA digestion would be to directly measure hyaluronidase expression and activity via Western blot, qPCR, or ELISA. As discussed previously, increased CFL activity has been show to destabilize the F-actin filaments within invadopodia and inhibit matrix degradation via MMPs [3,105,124]. A gelatin-based invadopodia assay to quantify protein matrix digestion or using non-MMP-degradable crosslinkers could test the effects of CFL suppression specifically on MMP activity within the protrusions. Like with the assays targeting HA digestion, if there is a difference in the degree of gelatin digestion around the protrusions of CFL KD versus NT control, then it is likely that CFL suppression enhances MMP activity in some way.

To probe the differences in actin fiber tensions and traction forces between CFL KD and NT cells, future work could measure actin fiber retraction dynamics with laser nanosurgery and traction forces with traction force microscopy. While performing either assay in 3D could involve significant technical difficulties, it would answer if the protrusions are tension-bearing and if the tension or traction forces differ between CFL KD and NT cells. In our previous work, we showed that CFL KD resulted in accumulation of low-tension actin stress fibers and higher traction forces within osteosarcoma cells on 2D [142]. It would be interesting to probe if CFL KD resulted in similarly low-tension actin fibers and increased traction forces, since the number of protrusions and thus actin fibers is also elevated.

Chapter 6: References

1. Petrie, R.J., and Yamada, K.M. (2012). At the leading ed of three-dimensional cell migration. J. Cell Sci. *125*, 5917–5926. https://doi.org/10.1242/jcs.093732.

2. Friedl, P., Sahai, E., Weiss, S., and Yamada, K.M. (2012). New dimensions in cell migration. Nat. Rev. Mol. Cell Biol. *13*, 743–747. 10.1038/nrm3459.

3. Yamaguchi, H., and Condeelis, J. (2007). Regulation of the actin cytoskeleton in cancer cell migration and invasion. Biochim. Biophys. Acta - Mol. Cell Res. *1773*, 642–652. 10.1016/j.bbamcr.2006.07.001.

4. Wyckoff, J.B., Pinner, S.E., Gschmeissner, S., Condeelis, J.S., and Sahai, E. (2006). ROCK- and Myosin-Dependent Matrix Deformation Enables Protease-Independent Tumor-Cell Invasion In Vivo. Curr. Biol. *16*, 1515–1523. 10.1016/j.cub.2006.05.065.

5. Lehtimäki, J., Hakala, M., and Lappalainen, P. (2017). Actin Filament Structures in Migrating Cells. In The Actin Cytoskeleton, B. M. Jockusch, ed. (Cham: Springer International Publishing), pp. 123–152. 10.1007/164_2016_28.

6. Maekawa, M., Ishizaki, T., Boku, S., Watanabe, N., Fujita, A., Iwamatsu, A., Obinata, T., Ohashi, K., Mizuno, K., and Narumiya, S. (1999). Signaling from Rho to the Actin Cytoskeleton Through Protein Kinases ROCK and LIM-kinase. Science *285*, 895–898. 10.1126/science.285.5429.895.

7. Ridley, A.J., Schwartz, M.A., Burridge, K., Firtel, R.A., Ginsberg, M.H., Borisy, G., Parsons, J.T., and Horwitz, A.R. (2003). Cell Migration: Integrating Signals from Front to Back. Science *302*, 1704–1709. 10.1126/science.1092053.

8. Blanchoin, L., Boujemaa-Paterski, R., Sykes, C., and Plastino, J. (2014). Actin Dynamics, Architecture, and Mechanics in Cell Motility. Physiol. Rev. *94*, 235–263. 10.1152/physrev.00018.2013.

9. Parsons, J.T., Horwitz, A.R., and Schwartz, M.A. (2010). Cell adhesion: integrating cytoskeletal dynamics and cellular tension. Nat. Rev. Mol. Cell Biol. *11*, 633–643. 10.1038/nrm2957.

10. Yamada, K.M., and Sixt, M. (2019). Mechanisms of 3D cell migration. Nat. Rev. Mol. Cell Biol. *20*, 738–752. 10.1038/s41580-019-0172-9.

11. Colin, A., Kotila, T., Guérin, C., Orhant-Prioux, M., Vianay, B., Mogilner, A., Lappalainen, P., Théry, M., and Blanchoin, L. (2023). Recycling of the actin monomer pool limits the lifetime of network turnover. EMBO J. *42*, e112717. 10.15252/embj.2022112717.

12. Goode, B.L., Eskin, J., and Shekhar, S. (2023). Mechanisms of actin disassembly and turnover. J. Cell Biol. *222*, e202309021. 10.1083/jcb.202309021.

13. Balcer, H.I., Goodman, A.L., Rodal, A.A., Smith, E., Kugler, J., Heuser, J.E., and Goode, B.L. (2003). Coordinated Regulation of Actin Filament Turnover by a High-Molecular-Weight Srv2/CAP Complex, Cofilin, Profilin, and Aip1. Curr. Biol. *13*, 2159–2169. 10.1016/j.cub.2003.11.051.

14. Pollard, T.D., and Borisy, G.G. (2003). Cellular Motility Driven by Assembly and Disassembly of Actin Filaments. Cell *112*, 453–465. 10.1016/S0092-8674(03)00120-X.

15. Lappalainen, P., and Drubin, D.G. (1997). Cofilin promotes rapid actin filament turnover in vivo. Nature *388*, 78–82. 10.1038/40418.

16. Bertling, E., Hotulainen, P., Mattila, P.K., Matilainen, T., Salminen, M., and Lappalainen, P. (2004). Cyclase-associated Protein 1 (CAP1) Promotes Cofilin-induced Actin Dynamics in Mammalian Nonmuscle Cells. Mol. Biol. Cell *15*, 2324–2334. 10.1091/mbc.e04-01-0048.

17. Kato, A., Kurita, S., Hayashi, A., Kaji, N., Ohashi, K., and Mizuno, K. (2008). Critical roles of actin-interacting protein 1 in cytokinesis and chemotactic migration of mammalian cells. Biochem. J. *414*, 261–270. 10.1042/BJ20071655.

18. Arora, P.D., and McCulloch, C.A.G. (1996). Dependence of Fibroblast Migration on Actin Severing Activity of Gelsolin*. J. Biol. Chem. *271*, 20516–20523. 10.1074/jbc.271.34.20516.

19. Vartiainen, M.K., Sarkkinen, E.M., Matilainen, T., Salminen, M., and Lappalainen, P. (2003). Mammals Have Two Twinfilin Isoforms Whose Subcellular Localizations and Tissue Distributions Are Differentially Regulated *. J. Biol. Chem. *278*, 34347–34355. 10.1074/jbc.M303642200.

20. Bravo-Cordero, J.J., Magalhaes, M.A.O., Eddy, R.J., Hodgson, L., and Condeelis, J. (2013). Functions of cofilin in cell locomotion and invasion. Nat. Rev. Mol. Cell Biol. *14*, 405–417. 10.1038/nrm3609.

21. Arber, S., Barbayannis, F.A., Hanser, H., Schnelder, C., Stanyon, C.A., Bernards, O., and Caroni, P. (1998). Regulation of actin dynamics through phosphorylation of cofilin by LIM- kinase. Nature *393*, 805–809. 10.1038/31729.

22. Ghosh, M., Song, X., Mouneimne, G., Sidani, M., Lawrence, D.S., and Condeelis, J.S. (2004). Cofilin Promotes Actin Polymerization and Defines the Direction of Cell Motility. Science *304*, 743–746. 10.1126/science.1094561.

23. Wioland, H., Guichard, B., Senju, Y., Myram, S., Lappalainen, P., Jégou, A., and Romet-Lemonne, G. (2017). ADF/Cofilin Accelerates Actin Dynamics by Severing Filaments and Promoting Their Depolymerization at Both Ends. Curr. Biol. *27*, 1956-1967.e7. 10.1016/j.cub.2017.05.048.

24. Oser, M., and Condeelis, J. (2009). The cofilin activity cycle in lamellipodia and invadopodia. J. Cell. Biochem. *108*, 1252–1262. 10.1002/jcb.22372.

25. Scott, R.W., Hooper, S., Crighton, D., Li, A., König, I., Munro, J., Trivier, E., Wickman, G., Morin, P., Croft, D.R., *et al.* (2010). LIM kinases are required for invasive path generation by tumor and tumor-associated stromal cells. J. Cell Biol. *191*, 169–185. 10.1083/jcb.201002041.

26. Toshima, J., Toshima, J.Y., Amano, T., Yang, N., Narumiya, S., and Mizuno, K. (2001). Cofilin Phosphorylation by Protein Kinase Testicular Protein Kinase 1 and Its Role in Integrin-mediated Actin Reorganization and Focal Adhesion Formation. Mol. Biol. Cell *12*, 1131–1145. 10.1091/mbc.12.4.1131.

27. Gohla, A., Birkenfeld, J., and Bokoch, G.M. (2005). Chronophin, a novel HAD-type serine protein phosphatase, regulates cofilin-dependent actin dynamics. Nat. Cell Biol. *7*, 21–29. 10.1038/ncb1201.

28. Niwa, R., Nagata-Ohashi, K., Takeichi, M., Mizuno, K., and Uemura, T. (2002). Control of actin reorganization by slingshot, a family of phosphatases that dephosphorylate ADF/cofilin. Cell *108*, 233–246. 10.1016/S0092-8674(01)00638-9.

29. Koshy, M., Villano, J.L., Dolecek, T.A., Howard, A., Mahmood, U., Chmura, S.J., Weichselbaum, R.R., and McCarthy, B.J. (2012). Improved survival time trends for glioblastoma using the SEER 17 population-based registries. J. Neurooncol. *107*, 207–212. 10.1007/s11060-011-0738-7.

30. Ostrom, Q.T., Gittleman, H., Truitt, G., Boscia, A., Kruchko, C., and Barnholtz-Sloan, J.S. (2018). CBTRUS statistical report: Primary brain and other central nervous system tumors diagnosed in the United States in 2011-2015. Neuro-Oncol. *20*, iv1–iv86. 10.1093/neuonc/noy131.

31. Watanabe, M., Tanaka, R., and Takeda, N. (1992). Magnetic resonance imaging and histopathology of cerebral gliomas. Neuroradiology *34*, 463–469. 10.1007/BF00598951.

32. De Bonis, P., Anile, C., Pompucci, A., Fiorentino, A., Balducci, M., Chiesa, S., Lauriola, L., Maira, G., and Mangiola, A. (2013). The influence of surgery on recurrence pattern of glioblastoma. Clin. Neurol. Neurosurg. *115*, 37–43. 10.1016/j.clineuro.2012.04.005.

33. Young, R.M., Jamshidi, A., Davis, G., and Sherman, J.H. (2015). Current trends in the surgical management and treatment of adult glioblastoma. Ann. Transl. Med. *3*, 121. 10.3978/j.issn.2305-5839.2015.05.10.

34. Nakada, M., Nakada, S., Demuth, T., Tran, N.L., Hoelzinger, D.B., and Berens, M.E. (2007). Molecular targets of glioma invasion. Cell. Mol. Life Sci. *64*, 458–478. 10.1007/s00018-007-6342-5.

35. Portela, M., and Casas-Tintó, S. (2020). New Cellular Dimensions on Glioblastoma Progression. Neurosci. Insights *15*. 10.1177/2633105520923076.

36. Chen, J.W.E., Pedron, S., Shyu, P., Hu, Y., Sarkaria, J.N., and Harley, B.A.C. (2018). Influence of hyaluronic acid transitions in tumor microenvironment on glioblastoma malignancy and invasive behavior. Front. Mater. *5*. 10.3389/fmats.2018.00039.

37. Wolf, K.J., Chen, J., Coombes, J.D., Aghi, M.K., and Kumar, S. (2019). Dissecting and rebuilding the glioblastoma microenvironment with engineered materials. Nat. Rev. Mater. *4*, 651–668. 10.1038/s41578-019-0135-y.

38. de Gooijer, M.C., Guillén Navarro, M., Bernards, R., Wurdinger, T., and van Tellingen, O. (2018). An Experimenter's Guide to Glioblastoma Invasion Pathways. Trends Mol. Med. *24*, 763–780. 10.1016/j.molmed.2018.07.003.

39. Chen, J., and Kumar, S. (2017). Biophysical regulation of cancer stem/initiating cells: Implications for disease mechanisms and translation. Curr. Opin. Biomed. Eng. *1*, 87–95. 10.1016/j.cobme.2017.02.006.

40. Chen, J., Ananthanarayanan, B., Springer, K.S., Wolf, K.J., Sheyman, S.M., Tran, V.D., and Kumar, S. (2020). Suppression of LIM kinase 1 and LIM kinase 2 limits glioblastoma invasion. Cancer Res. *80*, 69–78. 10.1158/0008-5472.CAN-19-1237.

41. Carter, S.B. (1967). Haptotactic islands. Exp. Cell Res. *48*, 189–193. 10.1016/0014-4827(67)90298-4.

42. Thery, M. (2010). Micropatterning as a tool to decipher cell morphogenesis and functions. J. Cell Sci. *123*, 4201–4213. 10.1242/jcs.075150.

43. Harris, A. (1973). Behavior of cultured cells on substrata of variable adhesiveness. Exp. Cell Res. *77*, 285–297. 10.1016/0014-4827(73)90579-X.

44. Watt, F.M., Jordan, P.W., and O'Neill, C.H. (1988). Cell shape controls terminal differentiation of human epidermal keratinocytes. Proc. Natl. Acad. Sci. U. S. A. *85*, 5576–5580. 10.1073/pnas.85.15.5576.

45. Roskelley, C.D., Desprez, P.Y., and Bissell, M.J. (1994). Extracellular matrix-dependent tissue-specific gene expression in mammary epithelial cells requires both physical and biochemical signal transduction. Proc. Natl. Acad. Sci. U. S. A. *91*, 12378–12382. 10.1073/pnas.91.26.12378.

46. Chen, C.S., Mrksich, M., Huang, S., Whitesides, G.M., and Ingber, D.E. (1997). Geometric Control of Cell Life and Death. Science *276*, 1425–1428. 10.1126/science.276.5317.1425.

47. Paszek, M.J., and Weaver, V.M. (2004). The Tension Mounts: Mechanics Meets Morphogenesis and Malignancy. J. Mammary Gland Biol. Neoplasia *9*. 10.1007/s10911-004-1404-x.

48. Paluch, E., and Heisenberg, C.P. (2009). Biology and Physics of Cell Shape Changes in Development. Curr. Biol. *19*, R790–R799. 10.1016/j.cub.2009.07.029.

49. Ladoux, B., and Mège, R.M. (2017). Mechanobiology of collective cell behaviours. Nat. Rev. Mol. Cell Biol. *18*, 743–757. 10.1038/nrm.2017.98.

50. McBeath, R., Pirone, D.M., Nelson, C.M., Bhadriraju, K., and Chen, C.S. (2004). Cell Shape, Cytoskeletal Tension, and RhoA Regulate Stem Cell Lineage Commitment. Dev. Cell *6*, 483–495. 10.1016/S1534-5807(04)00075-9.

51. Wang, N., Ostuni, E., Whitesides, G.M., and Ingber, D.E. (2002). Micropatterning tractional forces in living cells. Cell Motil. Cytoskeleton *52*, 97–106. 10.1002/cm.10037.

52. Parker, K.K., Brock, A.L., Brangwynne, C., Mannix, R.J., Wang, N., Ostuni, E., Geisse, N.A., Adams, J.C., Whitesides, G.M., and Ingber, D.E. (2002). Directional control of lamellipodia extension by constraining cell shape and orienting cell tractional forces. FASEB J. *16*, 1195–1204. 10.1096/fj.02-0038com.

53. Gomez, E.W., Chen, Q.K., Gjorevski, N., and Nelson, C.M. (2010). Tissue geometry patterns epithelial-mesenchymal transition via intercellular mechanotransduction. J. Cell. Biochem. *110*, 44–51. 10.1002/jcb.22545.

54. Baker, B.M., and Chen, C.S. (2012). Deconstructing the third dimension – how 3D culture microenvironments alter cellular cues. J. Cell Sci. *125*, 3015–3024. 10.1242/jcs.079509.

55. Li, Y., and Kilian, K.A. (2015). Bridging the Gap: From 2D Cell Culture to 3D Microengineered Extracellular Matrices. Adv. Healthc. Mater. *4*, 2780–2796. 10.1002/adhm.201500427.

56. Liu, A.P., Chaudhuri, O., and Parekh, S.H. (2017). New advances in probing cell-extracellular matrix interactions. Integr. Biol. U. K. *9*, 383–405. 10.1039/c6ib00251j.

57. Singhvi, R., Kumar, A., Lopez, G., Stephanopoulos, G., Wang, D., Whitesides, G., and Ingber, D. (1994). Engineering cell shape and function. Science *264*, 696–698. 10.1126/science.8171320.

58. Kilian, K.A., Bugarija, B., Lahn, B.T., and Mrksich, M. (2010). Geometric cues for directing the differentiation of mesenchymal stem cells. Proc. Natl. Acad. Sci. *107*, 4872–4877. 10.1073/pnas.0903269107.

59. Bray, M.-A.P., Adams, W.J., Geisse, N.A., Feinberg, A.W., Sheehy, S.P., and Parker, K.K. (2010). Nuclear morphology and deformation in engineered cardiac myocytes and tissues. Biomaterials *31*, 5143–5150. 10.1016/j.biomaterials.2010.03.028.

60. Kassianidou, E., Brand, C.A., Schwarz, U.S., and Kumar, S. (2017). Geometry and network connectivity govern the mechanics of stress fibers. Proc. Natl. Acad. Sci. *114*, 2622–2627. 10.1073/pnas.1606649114.

61. Lee, S., Kassianidou, E., and Kumar, S. (2018). Actomyosin stress fiber subtypes have unique viscoelastic properties and roles in tension generation. Mol. Biol. Cell *29*, 1992–2004. 10.1091/mbc.E18-02-0106.

62. Grasso, S., Hernández, J.A., and Chifflet, S. (2007). Roles of wound geometry, wound size, and extracellular matrix in the healing response of bovine corneal endothelial cells in culture. Am. J. Physiol. - Cell Physiol. *293*. 10.1152/ajpcell.00001.2007.

63. Ravasio, A., Le, A.P., Saw, T.B., Tarle, V., Ong, H.T., Bertocchi, C., Mège, R.M., Lim, C.T., Gov, N.S., and Ladoux, B. (2015). Regulation of epithelial cell organization by tuning cell-substrate adhesion. Integr. Biol. U. K. *7*, 1228–1241. 10.1039/c5ib00196j.

64. Vedula, S.R.K., Peyret, G., Cheddadi, I., Chen, T., Brugués, A., Hirata, H., Lopez-Menendez, H., Toyama, Y., Neves de Almeida, L., Trepat, X., *et al.* (2015). Mechanics of epithelial closure over non-adherent environments. Nat. Commun. *6*, 6111–6111. 10.1038/ncomms7111.

65. Chen, T., Callan-Jones, A., Fedorov, E., Ravasio, A., Brugués, A., Ong, H.T., Toyama, Y., Low, B.C., Trepat, X., Shemesh, T., *et al.* (2019). Large-scale curvature sensing by directional actin flow drives cellular migration mode switching. Nat. Phys. *15*, 393–402. 10.1038/s41567-018-0383-6.

66. Kassianidou, E., Probst, D., Jäger, J., Lee, S., Roguet, A.L., Schwarz, U.S., and Kumar, S. (2019). Extracellular Matrix Geometry and Initial Adhesive Position Determine Stress Fiber Network Organization during Cell Spreading. Cell Rep. *27*, 1897–1909. 10.1016/j.celrep.2019.04.035.

67. Goodman, S.L., Sims, P.A., and Albrecht, R.M. (1996). Three-dimensional extracellular matrix textured biomaterials. Biomaterials *17*, 2087–2095. 10.1016/0142-9612(96)00016-6.

68. Bettinger, C.J., Langer, R., and Borenstein, J.T. (2009). Engineering substrate topography at the Micro- and nanoscale to control cell function. Angew. Chem. - Int. Ed. *48*, 5406–5415. 10.1002/anie.200805179.

69. Raghunathan, V., McKee, C., Cheung, W., Naik, R., Nealey, P.F., Russell, P., and Murphy, C.J. (2013). Influence of extracellular matrix proteins and substratum topography on corneal epithelial cell alignment and migration. Tissue Eng. - Part A *19*, 1713–1722. 10.1089/ten.tea.2012.0584.

70. Teixeira, A.I., Abrams, G.A., Bertics, P.J., Murphy, C.J., and Nealey, P.F. (2003). Epithelial contact guidance on well-defined micro- and nanostructured substrates. J. Cell Sci. *116*, 1881–1892. 10.1242/jcs.00383.

71. Gerecht, S., Bettinger, C.J., Zhang, Z., Borenstein, J.T., Vunjak-Novakovic, G., and Langer, R. (2007). The effect of actin disrupting agents on contact guidance of human embryonic stem cells. Biomaterials *28*, 4068–4077. 10.1016/j.biomaterials.2007.05.027.

72. Curtis, A.S.G., Gadegaard, N., Dalby, M.J., Riehle, M.O., Wilkinson, C.D.W., and Aitchison, G. (2004). Cells React to Nanoscale Order and Symmetry in Their Surroundings. IEEE Trans. Nanobioscience *3*, 61–65. 10.1109/TNB.2004.824276.

73. Choi, C.H., Hagvall, S.H., Wu, B.M., Dunn, J.C.Y., Beygui, R.E., and CJ Kim, C.J. (2007). Cell interaction with three-dimensional sharp-tip nanotopography. Biomaterials *28*, 1672–1679. 10.1016/j.biomaterials.2006.11.031.

74. Chen, W., Shao, Y., Li, X., Zhao, G., and Fu, J. (2014). Nanotopographical surfaces for stem cell fate control: Engineering mechanobiology from the bottom. Nano Today *9*, 759–784. 10.1016/j.nantod.2014.12.002.

75. Puliafito, A., Ricciardi, S., Pirani, F., Čermochová, V., Boarino, L., De Leo, N., Primo, L., and Descrovi, E. (2019). Driving Cells with Light-Controlled Topographies. Adv. Sci. *6*, 1801826–1801826. 10.1002/advs.201801826.

76. Kshitiz, Afzal, J., Kim, S.Y., and Kim, D.H. (2015). A nanotopography approach for studying the structure-function relationships of cells and tissues. Cell Adhes. Migr. *9*, 300–307. 10.4161/cam.29359.

77. Buch-Månson, N., Kang, D.H., Kim, D., Lee, K.E., Yoon, M.H., and Martinez, K.L. (2017). Mapping cell behavior across a wide range of vertical silicon nanocolumn densities. Nanoscale *9*, 5517–5527. 10.1039/c6nr09700f.

78. Lou, H.Y., Zhao, W., Li, X., Duan, L., Powers, A., Akamatsu, M., Santoro, F., McGuire, A.F., Cui, Y., Drubin, D.G., *et al.* (2019). Membrane curvature underlies actin reorganization in response to nanoscale surface topography. Proc. Natl. Acad. Sci. U. S. A. *116*, 23143–23151. 10.1073/pnas.1910166116.

79. Di Cio, S., Iskratsch, T., Connelly, J.T., and Gautrot, J.E. (2020). Contractile myosin rings and cofilin-mediated actin disassembly orchestrate ECM nanotopography sensing. Biomaterials. 10.1016/j.biomaterials.2019.119683.

80. Rolli, C.G., Seufferlein, T., Kemkemer, R., and Spatz, J.P. (2010). Impact of Tumor Cell Cytoskeleton Organization on Invasiveness and Migration: A Microchannel-Based Approach. PLoS ONE *5*, e8726–e8726. 10.1371/journal.pone.0008726.

81. Balzer, E.M., Tong, Z., Paul, C.D., Hung, W., Stroka, K.M., Boggs, A.E., Martin, S.S., and Konstantopoulos, K. (2012). Physical confinement alters tumor cell adhesion and migration phenotypes. FASEB J. *26*, 4045–4056. 10.1096/fj.12-211441.

82. Pathak, A., and Kumar, S. (2012). Independent regulation of tumor cell migration by matrix stiffness and confinement. Proc. Natl. Acad. Sci. *109*, 10334–10339. 10.1073/pnas.1118073109.

83. Kraning-Rush, C.M., Carey, S.P., Lampi, M.C., and Reinhart-King, C.A. (2013). Microfabricated collagen tracks facilitate single cell metastatic invasion in 3D. Integr. Biol. *5*, 606–606. 10.1039/c3ib20196a.

84. Rianna, C., Radmacher, M., and Kumar, S. (2020). Direct evidence that tumor cells soften when navigating confined spaces. Mol. Biol. Cell *31*, 1726–1734. 10.1091/mbc.E19-10-0588.

85. Wullkopf, L., West, A.-K.V., Leijnse, N., Cox, T.R., Madsen, C.D., Oddershede, L.B., and Erler, J.T. (2018). Cancer cells' ability to mechanically adjust to extracellular matrix stiffness correlates with their invasive potential. Mol. Biol. Cell *29*, 2378–2385. 10.1091/mbc.E18-05-0319.

86. Mosier, J.A., Rahman-Zaman, A., Zanotelli, M.R., VanderBurgh, J.A., Bordeleau, F., Hoffman, B.D., and Reinhart-King, C.A. (2019). Extent of Cell Confinement in Microtracks Affects Speed and Results in Differential Matrix Strains. Biophys. J. *117*, 1692–1701. 10.1016/j.bpj.2019.09.024.

87. Holle, A.W., Govindan Kutty Devi, N., Clar, K., Fan, A., Saif, T., Kemkemer, R., and Spatz, J.P. (2019). Cancer Cells Invade Confined Microchannels via a Self-Directed Mesenchymal-to-Amoeboid Transition. Nano Lett. *19*, 2280–2290. 10.1021/acs.nanolett.8b04720.

88. Mistriotis, P., Wisniewski, E.O., Bera, K., Keys, J., Li, Y., Tuntithavornwat, S., Law, R.A., Perez-Gonzalez, N.A., Erdogmus, E., Zhang, Y., *et al.* (2019). Confinement hinders motility by inducing RhoA-mediated nuclear influx, volume expansion, and blebbing. J. Cell Biol. *218*, 4093–4111. 10.1083/jcb.201902057.

89. Srivastava, N., Traynor, D., Piel, M., Kabla, A.J., and Kay, R.R. (2020). Pressure sensing through Piezo channels controls whether cells migrate with blebs or pseudopods. Proc. Natl. Acad. Sci. U. S. A. *117*, 2506–2512. 10.1073/pnas.1905730117.

90. Caliari, S.R., and Burdick, J.A. (2016). A practical guide to hydrogels for cell culture. Nat. Methods *13*, 405–414. 10.1038/nmeth.3839.

91. Bao, M., Xie, J., Piruska, A., and Huck, W.T.S. (2017). 3D microniches reveal the importance of cell size and shape. Nat. Commun. *8*. 10.1038/s41467-017-02163-2.

92. Bao, M., Xie, J., Katoele, N., Hu, X., Wang, B., Piruska, A., and Huck, W.T.S. (2019). Cellular Volume and Matrix Stiffness Direct Stem Cell Behavior in a 3D Microniche. ACS Appl. Mater. Interfaces *11*, 1754–1759. 10.1021/acsami.8b19396.

93. Pathak, A., and Kumar, S. (2011). Biophysical regulation of tumor cell invasion: moving beyond matrix stiffness. Integr. Biol. *3*, 267–267. 10.1039/c0ib00095g.

94. De France, K.J., Yager, K.G., Chan, K.J.W., Corbett, B., Cranston, E.D., and Hoare, T. (2017). Injectable Anisotropic Nanocomposite Hydrogels Direct in Situ Growth and Alignment of Myotubes. Nano Lett. *17*, 6487–6495. 10.1021/acs.nanolett.7b03600.

95. Paul, C.D., Hruska, A., Staunton, J.R., Burr, H.A., Daly, K.M., Kim, J., Jiang, N., and Tanner, K. (2019). Probing cellular response to topography in three dimensions. Biomaterials *197*, 101–118. 10.1016/j.biomaterials.2019.01.009.

96. Molley, T.G., Wang, X., Hung, T., Jayathilaka, P.B., Yang, J., and Kilian, K.A. (2020). Geometrically Structured Microtumors in 3D Hydrogel Matrices. Adv. Biosyst. *4*, 2000056–2000056. 10.1002/adbi.202000056.

97. Hughes, A.J., Miyazaki, H., Coyle, M.C., Zhang, J., Laurie, M.T., Chu, D., Vavrušová, Z., Schneider, R.A., Klein, O.D., and Gartner, Z.J. (2018). Engineered Tissue Folding by Mechanical Compaction of the Mesenchyme. Dev. Cell *44*, 165-178.e6. 10.1016/j.devcel.2017.12.004.

98. Sunyer, R., Conte, V., Escribano, J., Elosegui-Artola, A., Labernadie, A., Valon, L., Navajas, D., Garcia-Aznar, J.M., Munoz, J.J., Roca-Cusachs, P., *et al.* (2016). Collective cell durotaxis emerges from long-range intercellular force transmission. Science *353*, 1157–1161. 10.1126/science.aaf7119.

99. Yamada, K.M., and Sixt, M. (2019). Mechanisms of 3D cell migration. Nat. Rev. Mol. Cell Biol. *20*, 738–752. 10.1038/s41580-019-0172-9.

100. Sanz-Moreno, V., and Marshall, C.J. (2010). The plasticity of cytoskeletal dynamics underlying neoplastic cell migration. Curr. Opin. Cell Biol. *22*, 690–696. 10.1016/j.ceb.2010.08.020.

101. Doyle, A.D., Petrie, R.J., Kutys, M.L., and Yamada, K.M. (2013). Dimensions in cell migration. Curr. Opin. Cell Biol. *25*, 642–649. 10.1016/j.ceb.2013.06.004.

102. Carey, S.P., Rahman, A., Kraning-Rush, C.M., Romero, B., Somasegar, S., Torre, O.M., Williams, R.M., and Reinhart-King, C.A. (2015). Comparative mechanisms of cancer cell migration through 3D matrix and physiological microtracks. APSselect *2*, C436–C447. 10.1152/ajpcell.00225.2014@apsselect.2015.2.issue-4.

103. Guetta-Terrier, C., Monzo, P., Zhu, J., Long, H., Venkatraman, L., Zhou, Y., Wang, P., Chew, S.Y., Mogilner, A., Ladoux, B., *et al.* (2015). Protrusive waves guide 3D cell migration along nanofibers. J. Cell Biol. *211*, 683–701. 10.1083/jcb.201501106.

104. Monzo, P., Chong, Y.K., Guetta-Terrier, C., Krishnasamy, A., Sathe, S.R., Yim, E.K.F., Ng, W.H., Ang, B.T., Tang, C., Ladoux, B., *et al.* (2016). Mechanical confinement triggers glioma linear migration dependent on formin FHOD3. Mol. Biol. Cell *27*, 1246–1261. 10.1091/mbc.E15-08-0565.

105. Scott, R.W., Hooper, S., Crighton, D., Li, A., König, I., Munro, J., Trivier, E., Wickman, G., Morin, P., Croft, D.R., *et al.* (2010). LIM kinases are required for invasive path generation by tumor and tumor-associated stromal cells. J. Cell Biol. *191*, 169–185. 10.1083/jcb.201002041.

106. Artym, V.V., Swatkoski, S., Matsumoto, K., Campbell, C.B., Petrie, R.J., Dimitriadis, E.K., Li, X., Mueller, S.C., Bugge, T.H., Gucek, M., *et al.* (2015). Dense fibrillar collagen is a potent inducer of invadopodia via a specific signaling network. J. Cell Biol. *208*, 331–350. 10.1083/jcb.201405099.

107. Bellail, A.C., Hunter, S.B., Brat, D.J., Tan, C., and Van Meir, E.G. (2004). Microregional extracellular matrix heterogeneity in brain modulates glioma cell invasion. Int. J. Biochem. Cell Biol. *36*, 1046–1069. 10.1016/j.biocel.2004.01.013.

108. Wolf, K.J., Shukla, P., Springer, K., Lee, S., Coombes, J.D., Choy, C.J., Kenny, S.J., Xu, K., and Kumar, S. (2020). A mode of cell adhesion and migration facilitated by CD44-dependent microtentacles. Proc. Natl. Acad. Sci. *117*, 11432–11443. 10.1073/pnas.1914294117.

109. Poincloux, R., Collin, O., Lizárraga, F., Romao, M., Debray, M., Piel, M., and Chavrier, P. (2011). Contractility of the cell rear drives invasion of breast tumor cells in 3D Matrigel. Proc. Natl. Acad. Sci. *108*, 1943–1948. 10.1073/pnas.1010396108.

110. Shibue, T., Brooks, M.W., and Weinberg, R.A. (2013). An Integrin-Linked Machinery of Cytoskeletal Regulation that Enables Experimental Tumor Initiation and Metastatic Colonization. Cancer Cell *24*, 481–498. 10.1016/j.ccr.2013.08.012.

111. Djuzenova, C.S., Fiedler, V., Memmel, S., Katzer, A., Hartmann, S., Krohne, G., Zimmermann, H., Scholz, C.J., Polat, B., Flentje, M., *et al.* (2015). Actin cytoskeleton organization, cell surface modification and invasion rate of 5 glioblastoma cell lines differing in PTEN and p53 status. Exp. Cell Res. *330*, 346–357. 10.1016/j.yexcr.2014.08.013.

112. Carmona, G., Perera, U., Gillett, C., Naba, A., Law, A.-L., Sharma, V.P., Wang, J., Wyckoff, J., Balsamo, M., Mosis, F., *et al.* (2016). Lamellipodin promotes invasive 3D cancer cell migration via regulated interactions with Ena/VASP and SCAR/WAVE. Oncogene *35*, 5155–5169. 10.1038/onc.2016.47.

113. Bangasser, B.L., Shamsan, G.A., Chan, C.E., Opoku, K.N., Tüzel, E., Schlichtmann, B.W., Kasim, J.A., Fuller, B.J., McCullough, B.R., Rosenfeld, S.S., *et al.* (2017). Shifting the optimal stiffness for cell migration. Nat. Commun. *8*, 15313. 10.1038/ncomms15313.

114. Ananthanarayanan, B., Kim, Y., and Kumar, S. (2011). Elucidating the mechanobiology of malignant brain tumors using a brain matrix-mimetic hyaluronic acid hydrogel platform. Biomaterials *32*, 7913–7923. 10.1016/J.BIOMATERIALS.2011.07.005.

115. Kim, Y., and Kumar, S. (2014). CD44-mediated adhesion to hyaluronic acid contributes to mechanosensing and invasive motility. Mol. Cancer Res. *12*, 1416–1429. 10.1158/1541-7786.MCR-13-0629.

116. Amofa, K.Y., Patterson, K.M., Ortiz, J., and Kumar, S. (2024). Dissecting TGF-β-induced glioblastoma invasion with engineered hyaluronic acid hydrogels. APL Bioeng. *8*, 026125. 10.1063/5.0203213.

117. Toole, B.P. (1990). Hyaluronan and its binding proteins, the hyaladherins. Curr. Opin. Cell Biol. *2*, 839–844. 10.1016/0955-0674(90)90081-o.

118. Ponta, H., Sherman, L., and Herrlich, P.A. (2003). CD44: From adhesion molecules to signalling regulators. Nat. Rev. Mol. Cell Biol. *4*, 33–45. 10.1038/nrm1004.

119. Wolf, K.J., Lee, S., and Kumar, S. (2018). A 3D topographical model of parenchymal infiltration and perivascular invasion in glioblastoma. APL Bioeng. *2*, 31903–31903. 10.1063/1.5021059.

120. Caswell, P.T., and Zech, T. (2018). Actin-Based Cell Protrusion in a 3D Matrix. Trends Cell Biol. *28*, 823–834. 10.1016/j.tcb.2018.06.003.

121. Belian, S., Korenkova, O., and Zurzolo, C. (2023). Actin-based protrusions at a glance. J. Cell Sci. *136*, jcs261156. 10.1242/jcs.261156.

122. Jacquemet, G., Hamidi, H., and Ivaska, J. (2015). Filopodia in cell adhesion, 3D migration and cancer cell invasion. Curr. Opin. Cell Biol. *36*, 23–31. 10.1016/J.CEB.2015.06.007.

123. Yamaguchi, H., Lorenz, M., Kempiak, S., Sarmiento, C., Coniglio, S., Symons, M., Segall, J., Eddy, R., Miki, H., Takenawa, T., *et al.* (2005). Molecular mechanisms of invadopodium formation. J. Cell Biol. *168*, 441–452. 10.1083/jcb.200407076.

124. Oser, M., Yamaguchi, H., Mader, C.C., Bravo-Cordero, J.J., Arias, M., Chen, X., DesMarais, V., van Rheenen, J., Koleske, A.J., and Condeelis, J. (2009). Cortactin

regulates cofilin and N-WASp activities to control the stages of invadopodium assembly and maturation. J. Cell Biol. *186*, 571–587. 10.1083/jcb.200812176.

125. Bamburg, J.R. (1999). Proteins of the ADF/Cofilin Family: Essential Regulators of Actin Dynamics. Annu. Rev. Cell Dev. Biol. *15*, 185–230. 10.1146/annurev.cellbio.15.1.185.

126. McGrath, J.L., Osborn, E.A., Tardy, Y.S., Dewey, C.F., and Hartwig, J.H. (2000). Regulation of the actin cycle in vivo by actin filament severing. Proc. Natl. Acad. Sci. *97*, 6532–6537. 10.1073/pnas.100023397.

127. Southwick, F.S. (2000). Gelsolin and ADF/cofilin enhance the actin dynamics of motile cells. Proc. Natl. Acad. Sci. *97*, 6936–6938. 10.1073/pnas.97.13.6936.

128. Hilton, D.M., Aguilar, R.M., Johnston, A.B., and Goode, B.L. (2018). Species-Specific Functions of Twinfilin in Actin Filament Depolymerization. J. Mol. Biol. *430*, 3323–3336. 10.1016/j.jmb.2018.06.025.

129. Kotila, T., Wioland, H., Enkavi, G., Kogan, K., Vattulainen, I., Jégou, A., Romet-Lemonne, G., and Lappalainen, P. (2019). Mechanism of synergistic actin filament pointed end depolymerization by cyclase-associated protein and cofilin. Nat. Commun. 10.1038/s41467-019-13213-2.

130. McCollum, C.O., Didychuk, A.L., Liu, D., Murray-Nerger, L.A., Cristea, I.M., and Glaunsinger, B.A. (2023). The viral packaging motor potentiates Kaposi's sarcoma-associated herpesvirus gene expression late in infection. PLOS Pathog. *19*, e1011163. 10.1371/journal.ppat.1011163.

131. Dull, T., Zufferey, R., Kelly, M., Mandel, R.J., Nguyen, M., Trono, D., and Naldini, L. (1998). A Third-Generation Lentivirus Vector with a Conditional Packaging System. J. Virol. *72*, 8463–8471. 10.1128/jvi.72.11.8463-8471.1998.

132. Sanjana, N.E., Shalem, O., and Zhang, F. (2014). Improved vectors and genome-wide libraries for CRISPR screening. Nat. Methods *11*, 783–784. 10.1038/nmeth.3047.

133. Morgens, D.W., Wainberg, M., Boyle, E.A., Ursu, O., Araya, C.L., Tsui, C.K., Haney, M.S., Hess, G.T., Han, K., Jeng, E.E., *et al.* (2017). Genome-scale measurement of off-target activity using Cas9 toxicity in high-throughput screens. Nat. Commun. *8*, 15178. 10.1038/ncomms15178.

134. Han, K., Jeng, E.E., Hess, G.T., Morgens, D.W., Li, A., and Bassik, M.C. (2017). Synergistic drug combinations for cancer identified in a CRISPR screen for pairwise genetic interactions. Nat. Biotechnol. *35*, 463–474. 10.1038/nbt.3834.

135. Schindelin, J., Arganda-Carreras, I., Frise, E., Kaynig, V., Longair, M., Pietzsch, T., Preibisch, S., Rueden, C., Saalfeld, S., Schmid, B., *et al.* (2012). Fiji: an open-source platform for biological-image analysis. Nat. Methods *9*, 676–682. 10.1038/nmeth.2019.

136. Tinevez, J.-Y., Perry, N., Schindelin, J., Hoopes, G.M., Reynolds, G.D., Laplantine, E., Bednarek, S.Y., Shorte, S.L., and Eliceiri, K.W. (2017). TrackMate: An open and extensible platform for single-particle tracking. Methods *115*, 80–90. 10.1016/j.ymeth.2016.09.016.

137. Ershov, D., Phan, M.-S., Pylvänäinen, J.W., Rigaud, S.U., Le Blanc, L., Charles-Orszag, A., Conway, J.R.W., Laine, R.F., Roy, N.H., Bonazzi, D., *et al.* (2022). TrackMate 7: integrating state-of-the-art segmentation algorithms into tracking pipelines. Nat. Methods *19*, 829–832. 10.1038/s41592-022-01507-1.

138. Arshadi, C., Günther, U., Eddison, M., Harrington, K.I.S., and Ferreira, T.A. (2021). SNT: a unifying toolbox for quantification of neuronal anatomy. Nat. Methods *18*, 374–377. 10.1038/s41592-021-01105-7.

139. Wang, W., Mouneimne, G., Sidani, M., Wyckoff, J., Chen, X., Makris, A., Goswami, S., Bresnick, A.R., and Condeelis, J.S. (2006). The activity status of cofilin is directly related to invasion, intravasation, and metastasis of mammary tumors. J. Cell Biol. *173*, 395–404. 10.1083/jcb.200510115.

140. Wang, W., Eddy, R., and Condeelis, J. (2007). The cofilin pathway in breast cancer invasion and metastasis. Nat. Rev. Cancer *7*, 429–440. 10.1038/nrc2148.

141. Bravo-Cordero, J.J., Magalhaes, M.A.O., Eddy, R.J., Hodgson, L., and Condeelis, J. (2013). Functions of cofilin in cell locomotion and invasion. Nat. Rev. Mol. Cell Biol. *14*, 405–417. 10.1038/nrm3609.

142. Lee, S., and Kumar, S. (2020). Cofilin is required for polarization of tension in stress fiber networks during migration. J. Cell Sci. https://doi.org/10.1242/jcs.243873.

143. Tojkander, S., Gateva, G., Husain, A., Krishnan, R., and Lappalainen, P. (2015). Generation of contractile actomyosin bundles depends on mechanosensitive actin filament assembly and disassembly. eLife *4*. 10.7554/eLife.06126.001.

144. Hotulainen, P., Paunola, E., Vartiainen, M.K., and Lappalainen, P. (2005). Actin-depolymerizing Factor and Cofilin-1 Play Overlapping Roles in Promoting Rapid F-Actin Depolymerization in Mammalian Nonmuscle Cells. Mol. Biol. Cell *16*, 649–664. 10.1091/mbc.E04-07-0555.

145. Cha, J., Koh, I., Choi, Y., Lee, J., Choi, C., and Kim, P. (2015). Tapered Microtract Array Platform for Antimigratory Drug Screening of Human Glioblastoma Multiforme. Adv. Healthc. Mater. *4*, 405–411. 10.1002/adhm.201400384.

146. Bohil, A.B., Robertson, B.W., and Cheney, R.E. (2006). Myosin-X is a molecular motor that functions in filopodia formation. Proc. Natl. Acad. Sci. *103*, 12411–12416. 10.1073/pnas.0602443103.

147. Zebda, N., Bernard, O., Bailly, M., Welti, S., Lawrence, D.S., and Condeelis, J.S. (2000). Phosphorylation of Adf/Cofilin Abolishes Egf-Induced Actin Nucleation at the Leading Edge and Subsequent Lamellipod Extension. J. Cell Biol. *151*, 1119–1128.

148. Sahai, E., Olson, M.F., and Marshall, C.J. (2001). Cross-talk between Ras and Rho signalling pathways in transformation favours proliferation and increased motility. EMBO J. *20*, 755–766. 10.1093/emboj/20.4.755.

149. Nagai, S., Moreno, O., Smith, C.A., Ivanchuk, S., Romagnuolo, R., Golbourn, B., Weeks, A., Seol, H.J., and Rutka, J.T. (2011). Role of the Cofilin Activity Cycle in Astrocytoma Migration and Invasion. Genes Cancer *2*, 859–869. 10.1177/1947601911431839.

150. Yap, C.T., Simpson, T.I., Pratt, T., Price, D.J., and Maciver, S.K. (2005). The motility of glioblastoma tumour cells is modulated by intracellular cofilin expression in a concentration-dependent manner. Cell Motil. *60*, 153–165. 10.1002/cm.20053.

151. Nishita, M., Tomizawa, C., Yamamoto, M., Horita, Y., Ohashi, K., and Mizuno, K. (2005). Spatial and temporal regulation of cofilin activity by LIM kinase and Slingshot is critical for directional cell migration. J. Cell Biol. *171*, 349–359. 10.1083/jcb.200504029.

152. Kobayashi, M., Nishita, M., Mishima, T., Ohashi, K., and Mizuno, K. (2006). MAPKAPK-2-mediated LIM-kinase activation is critical for VEGF-induced actin remodeling and cell migration. EMBO J. *25*, 713–726. 10.1038/sj.emboj.7600973.

153. Horita, Y., Ohashi, K., Mukai, M., Inoue, M., and Mizuno, K. (2008). Suppression of the Invasive Capacity of Rat Ascites Hepatoma Cells by Knockdown of Slingshot or LIM Kinase * □ S Downloaded from. J. Biol. Chem. *283*, 6013–6021. 10.1074/jbc.M706538200.

154. Klemke, M., Kramer, E., Konstandin, M.H., Wabnitz, G.H., and Samstag, Y. (2010). An MEK-cofilin signalling module controls migration of human T cells in 3D but not 2D environments. EMBO J. *29*, 2915–2929. 10.1038/emboj.2010.153.

155. Salz, A., Gurniak, C., Jönsson, F., and Witke, W. (2020). Cofilin1-driven actin dynamics controls migration of thymocytes and is essential for positive selection in the thymus. J. Cell Sci. *133*. 10.1242/jcs.238048.

156. Schulze, M., Fedorchenko, O., Zink, T.G., Knobbe-Thomsen, C.B., Kraus, S., Schwinn, S., Beilhack, A., Reifenberger, G., Monoranu, C.M., Sirén, A.-L., *et al.* (2016). Chronophin is a glial tumor modifier involved in the regulation of glioblastoma growth and invasiveness. Oncogene *35*, 3163–3177. 10.1038/onc.2015.376.

157. Yoshioka, K., Foletta, V., Bernard, O., and Itoh, K. (2003). A role for LIM kinase in cancer invasion. Proc. Natl. Acad. Sci. U. S. A. *100*, 7247–7252. 10.1073/pnas.1232344100.

158. Ding, Y., Milosavljevic, T., and Alahari, S.K. (2008). Nischarin Inhibits LIM Kinase To Regulate Cofilin Phosphorylation and Cell Invasion. Mol. Cell. Biol. *28*, 3742–3756. 10.1128/MCB.01832-07.

159. Wang, X., Zou, S., Ren, T., Zhao, L.-J., Yu, L.-F., Li, X.-Y., Yan, X., and Zhang, L.-J. (2021). Alantolactone suppresses the metastatic phenotype and induces the apoptosis of glioblastoma cells by targeting LIMK kinase activity and activating the cofilin/G-actin signaling cascade. Int. J. Mol. Med. *47*, 68. 10.3892/ijmm.2021.4901.

160. Shishkin, S., Eremina, L., Pashintseva, N., Kovalev, L., and Kovaleva, M. (2016). Cofilin-1 and Other ADF/Cofilin Superfamily Members in Human Malignant Cells. Int. J. Mol. Sci. *18*, 10–10. 10.3390/ijms18010010.

161. Coumans, J.V.F., Davey, R.J., and Moens, P.D.J. (2018). Cofilin and profilin: partners in cancer aggressiveness. Biophys. Rev. *10*, 1323–1335. 10.1007/s12551-018-0445-0.

162. Tran, V.D., and Kumar, S. (2021). Transduction of cell and matrix geometric cues by the actin cytoskeleton. Curr. Opin. Cell Biol. *68*, 64–71. 10.1016/j.ceb.2020.08.016.

163. Stone, O.J., Pankow, N., Liu, B., Sharma, V.P., Eddy, R.J., Wang, H., Putz, A.T., Teets, F.D., Kuhlman, B., Condeelis, J.S., *et al.* (2019). Optogenetic control of cofilin and αTAT in living cells using Z-lock. Nat. Chem. Biol. *15*, 1183–1190. 10.1038/s41589-019-0405-4.

164. Wang, H., Tao, L., Jin, F., Gu, H., Dai, X., Ni, T., Feng, J., Ding, Y., Xiao, W., Qian, Y., *et al.* (2017). Cofilin 1 induces the epithelial-mesenchymal transition of gastric cancer cells by promoting cytoskeletal rearrangement. Oncotarget *8*, 39131–39142. 10.18632/ONCOTARGET.16608.

165. Moffat, J., Grueneberg, D.A., Yang, X., Kim, S.Y., Kloepfer, A.M., Hinkle, G., Piqani, B., Eisenhaure, T.M., Luo, B., Grenier, J.K., *et al.* (2006). A Lentiviral RNAi Library for Human

and Mouse Genes Applied to an Arrayed Viral High-Content Screen. Cell *124*, 1283–1298. 10.1016/j.cell.2006.01.040.

166. Mohindra, P., Zhong, J.X., Fang, Q., Cuylear, D.L., Huynh, C., Qiu, H., Gao, D., Kharbikar, B.N., Huang, X., Springer, M.L., *et al.* (2023). Local decorin delivery via hyaluronic acid microrods improves cardiac performance, ventricular remodeling after myocardial infarction. Npj Regen. Med. *8*, 1–14. 10.1038/s41536-023-00336-w.

167. Ono, S. (2018). Functions of actin-interacting protein 1 (AIP1)/WD repeat protein 1 (WDR1) in actin filament dynamics and cytoskeletal regulation. Spec. Issue Actin Cytoskelet. Dyn. *506*, 315–322. 10.1016/j.bbrc.2017.10.096.

168. Zhou, G.-L., Zhang, H., and Field, J. (2014). Mammalian CAP (Cyclase-associated protein) in the world of cell migration. Cell Adhes. Migr. *8*, 55–59. 10.4161/cam.27479.

169. Shekhar, S., Hoeprich, G.J., Gelles, J., and Goode, B.L. (2020). Twinfilin bypasses assembly conditions and actin filament aging to drive barbed end depolymerization. J. Cell Biol. *220*, e202006022. 10.1083/jcb.202006022.

170. Svitkina, T.M., Bulanova, E.A., Chaga, O.Y., Vignjevic, D.M., Kojima, S., Vasiliev, J.M., and Borisy, G.G. (2003). Mechanism of filopodia initiation by reorganization of a dendritic network. J. Cell Biol. *160*, 409–421. 10.1083/jcb.200210174.

171. Lu, M., Witke, W., Kwiatkowski, D.J., and Kosik, K.S. (1997). Delayed Retraction of Filopodia in Gelsolin Null Mice. J. Cell Biol. *138*, 1279–1287. 10.1083/jcb.138.6.1279.

172. Garcia, J.H., Akins, E.A., Jain, S., Wolf, K.J., Zhang, J., Choudhary, N., Lad, M., Shukla, P., Rios, J., Seo, K., *et al.* (2024). Multiomic screening of invasive GBM cells reveals targetable transsulfuration pathway alterations. J. Clin. Invest. *134*. 10.1172/JCI170397.

173. Bourguignon, L.Y.W., Gilad, E., Rothman, K., and Peyrollier, K. (2005). Hyaluronan-CD44 Interaction with IQGAP1 Promotes Cdc42 and ERK Signaling, Leading to Actin Binding, Elk-1/Estrogen Receptor Transcriptional Activation, and Ovarian Cancer Progression *. J. Biol. Chem. *280*, 11961–11972. 10.1074/jbc.M411985200.

174. Zhu, D., and Bourguignon, L.Y.W. (1998). The ankyrin-binding domain of CD44s is involved in regulating hyaluronic acid-mediated functions and prostate tumor cell transformation. Cell Motil. *39*, 209–222. 10.1002/(SICI)1097-0169(1998)39:3<209::AID-CM4>3.0.CO;2-#.

175. Clucas, J., and Valderrama, F. (2014). ERM proteins in cancer progression. J. Cell Sci. *127*, 267–275. 10.1242/jcs.133108.

Appendix A – Supplementary Information for Chapter 3 and 4

Supplemental Table A1
A list of key reagents used in this work, with information about source and identifiers for each reagent.

Key Resources Table			
Reagent type	**Designation**	**Source**	**Identifiers**
Antibody	Polyclonal rabbit anti-MYO10	Sigma-Aldrich	Catalog #HPA024223; RRID: AB_1854248
Antibody	Goat anti-Mouse IgG polyclonal Alexa Fluor 647	Thermo Fisher Scientific	Catalog # A-21235
Antibody	Goat anti-Mouse IgG polyclonal Alexa Fluor 488	Thermo Fisher Scientific	Catalog # A-11001
Antibody	Goat anti-Rabbit IgG polyclonal Alexa Fluor 488	Thermo Fisher Scientific	Catalog # A-11008; RRID AB_143165
Antibody	Goat anti-Rabbit IgG polyclonal Alexa Fluor 647	Thermo Fisher Scientific	Catalog #A-21245a
Antibody	Monoclonal mouse anti-GAPDH	Sigma-Aldrich	Catalog #G8795
Antibody	Polyclonal rabbit anti-CD44	Invitrogen	Catalog #PA5-21419
Antibody	Monoclonal mouse anti-vinculin	Sigma-Aldrich	Catalog #V9131
Antibody	Rabbit anti-cofilin-1 (D3F9)	Cell Signaling Technology	Catalog #5175S
Antibody	Polyclonal rabbit anti-HYAL2	Abcam	Catalog #ab68608
Bacterial Strain	Top10 Competent E. coli	Thermo Fisher Scientific	Catalog #C404003
Bacterial Strain	XL1-Blue Competent E. coli	QB3 MacroLab	N/A
Chemicals and peptides	Alexa Fluor 647 Phalloidin	Cell Signaling Technology	Catalog #8940S
Chemicals and peptides	Alexa Fluor 546 Phalloidin	Thermo Fisher Scientific	Catalog #A-22283
Chemicals and peptides	4′,6-Diamidine-2′-phenylindole dihydrochloride (DAPI)	Sigma-Aldrich	Catalog #10236276001
Chemicals and peptides	Methacrylic Anhydride, 94%	Sigma-Aldrich	Catalog #276685
Chemicals and peptides	Poly-D-Lysine Hydrobromide	Sigma-Aldrich	Catalog #P1024-10MG
Chemicals and peptides	Sodium Pyruvate	Thermo Fisher Scientific	Catalog #11360070
Chemicals and peptides	MEM Non-Essential Amino Acids Solution	Thermo Fisher Scientific	Catalog #11140050
Chemicals and peptides	Penicillin/Streptomycin	Thermo Fisher Scientific	Catalog #15140

Chemicals and peptides	Fetal Calf Serum	JR Scientific	Catalog #44709
Chemicals and peptides	Trypsin-EDTA 0.25%, phenol red	Thermo Fisher Scientific	Catalog #25200
Chemicals and peptides	Dulbecco's Modified Eagle Medium (DMEM)	Thermo Fisher Scientific	Catalog #11965118
Chemicals and peptides	Sodium Hyaluronate, 66 kDa - 99 kDa	Lifecore	Catalog #HA60K-5
Chemicals and peptides	RGD Peptide (Ac-GCGYGRGDSPG- NH2)	Anaspec	N/A, custom order
Chemicals and peptides	Goat serum	Thermo Fisher Scientific	Catalog #16210064
Chemicals and peptides	Bovine Serum Albumin, heat shock fraction, pH 7, >=98%	Sigma-Aldrich	Catalog #A9647
Chemicals and peptides	Triton X-100	Sigma-Aldrich	Catalog #X100
Chemicals and peptides	Dithiothreitol (DTT)	Thermo Fisher Scientific	Catalog #FERR0861
Chemicals and peptides	DMEM, high glucose, no glutamine, no phenol red	Thermo Fisher Scientific	Catalog #31053028
Chemicals and peptides	Radioimmunoprecipitation assay buffer (RIPA)	Sigma-Aldrich	Catalog #R0278
Chemicals and peptides	4-12% bis-tris gels	Life Technologies	Catalog #NP0335BOX
Chemicals and peptides	Fluoromount-G	Fisher Scientific	Catalog # OB10001
Chemicals and peptides	Halt protease and phosphatase inhibitor cocktail	Thermo Fisher Scientific	Catalog #78442
Chemicals and peptides	Paraformaldehyde	Alfa-Aesar	Catalog #43368-9M
Chemicals and peptides	Blebbistatin	Sigma-Aldrich	Catalog #B0560
Chemicals and peptides	Cytochalasin D	Sigma-Aldrich	Catalog #C8273
Chemicals and peptides	Nocodazole	Cell Signaling Technology	Catalog #2190
Chemicals and peptides	Puromycin	Clontech	Catalog #631305
Chemicals and peptides	Blasticidin	Invivogen	Catalog #ant-bl-05
Chemicals and peptides	PolyJet transfection reagent	SignaGen	Catalog #SL100688
Chemicals and peptides	Polybrene	Millipore	Catalog #TR-1003-G
Chemicals and peptides	Bovine collagen type I solution	Advanced Biomatrix	Catalog #5010-50ML

Chemicals and peptides	Q5 Hotstart Master Mix	New England Biolabs	Catalog #M0494S
Chemicals and peptides	Human Plasma Fibronectin	Millipore	Catalog # FC010
Chemicals and peptides	SPY555-DNA	Cytoskeleton	Catalog #CY-SC201
Chemicals and peptides	T4 DNA Ligase	New England Biolabs	Catalog #M0202S
Chemicals and peptides	BstXI	New England Biolabs	Catalog #R0113S
Chemicals and peptides	BlpI	New England Biolabs	Catalog #R0585S
Chemicals and peptides	protease-degradable cross-linker (KKCGGPQGIWGQGCKK)	Genscript	N/A, custom order
Chemicals and peptides	Anti-Adherence Rinsing Solution	STEMCELL Technologies	Catalog #07010
Chemicals and peptides	Sodium hydroxide, 10.0 N	Fisher Scientific	Catalog #LC245004
Chemicals and peptides	HEPES (1 M)	Life Technologies	Catalog # 15640-080
Chemicals and peptides	10x phosphate buffered saline	Fisher BioReagent	Catalog #BP3994
Chemicals and peptides	Trizol	Invitrogen	Catalog #15596018
Commercial assay	Qiagen miniprep spin	Qiagen	
Commercial assay	Qiagen genomic DNA	Qiagen	
Commercial assay	Qiagen midi prep	Qiagen	
Commercial assay	Direct-zol RNA miniprep kit	Zymo	Catalog #R2502
Commercial assay	RNA Clean & Concentrator-5	Zymo	Catalog #R1013
Commercial assay	Iscript cDNA synthesis kit	Bio-Rad	Catalog #1708891
Commercial assay	PowerUp Sybr Green master mix	Fisher Scientific	Catalog #A25777
Cell line	Human glioblastoma: U-251 MG (male)	University of California, Berkeley Tissue Culture Facility	RRID: CVCL_0021
Cell line	HEK 293T	David Schaffer laboratory at UC Berkeley	ATCC Catalog # CRL-11268, CVCL_1926
Recombinant DNA	lentiCas9-Blast	Sanjana et al., 2014	Addgene plasmid #52962

Recombinant DNA	pMD2.G	Addgene	Addgene plasmid #12259
Recombinant DNA	pMCB320	Han et al., 2017	Addgene plasmid #89359
Recombinant DNA	pMDLg/pRRE	Dull et al., 1998	Addgene plasmid #12251
Recombinant DNA	pRSV-Rev	Dull et al., 1998	Addgene plasmid #12253
Recombinant DNA	pLKO.1-TRC	Moffat et al., 2006	Addgene plasmid #10878
Recombinant DNA	psPAX2	Addgene	Addgene plasmid #12260
Software and algorithm	Cell and nucleus segmentation	Mohindra et al., this paper	
Software and algorithm	ImageJ	NIH	
Software and algorithm	FIJI	Schindelin et al., 2012	
Software and algorithm	GraphPad Prism Version 10	GraphPad	
Software and algorithm	PyCharm		
Software and algorithm	Juypter Notebook		
Software and algorithm	Matlab		
Software and algorithm	Zen 2010, Zen Blue	Zeiss	
Software and algorithm	NIS-Elements	Nikon	
Software and algorithm	Primer Blast	NIH	
Software and algorithm	CRISPick	Broad Institute	
Software and algorithm	Benchling	Benchling	
Software and algorithm	TrackMate plug-in	Tinevez et al., 2017; Ershov et al., 2022	
Software and algorithm	SNT plug-in, Neuroanatomy package	Arshadi et al., 2021	
Equipment	Eclipse TE2000 Nikon Microscope	Nikon	
Equipment	Nikon W1 spinning disk confocal	Nikon	
Equipment	CFX real-time PCR detection system	Bio-Rad	
Equipment	iBright imaging system	Invitrogen	

Other	CellQART 24-well insert PET	Sterlitech	Catalog #9328012
Other	Aggrewell 400	STEMCELL Technologies	Catalog #34415
Other	Nitrocellulose membrane	Licor	Catalog #926-31092

Supplemental Table A2
A list of the CRISPR sgRNA sequences used in the studies in Chapter 3.

Guide name	**Target gene**	**Guide sequence 5'-3'**
PFN1 - 1	PFN1	CAAGGACTCGCCCTCCGTCT
PFN1 - 2	PFN1	CTACATCGACAACCTCATGG
PFN1 - 3	PFN1	GCAGGATGGGGAATTTAGCA
GSN - 1	GSN	ATTCTGTACAACTACCGCCA
GSN - 2	GSN	TGAGGTCCAGGGCTTCGAGT
GSN - 3	GSN	CAGGTCTCGGTCCTTCCTGA
CAP1 - 1	CAP1	AGGAGCAGCTCCATATGTGC
CAP1 - 2	CAP1	GTTCGCGCAGATTAATCAGG
CAP1 - 3	CAP1	GAACTGAGCGGACTGCCATC
WDR1 - 1	WDR1	GTGGCTCCCAGAGTAAATGT
WDR1 - 2	WDR1	GTGTGCGATTCTCTCCTGAT
WDR1 - 3	WDR1	GAGGCAATGTAGAATCCGCT
TWF1 - 1	TWF1	ACTTAGGTACAGACTGACGT
TWF1 - 2	TWF1	TTACTTACATGAGAATGATC
TWF1 - 3	TWF1	GGAATCATAATCCTTATCCC
CFL1 - 1	CFL1	GCATAGCGGCAGTCCTTATC
CFL1 - 2	CFL1	GGAGAGCAAGAAGGAGGATC
CFL1 - 3	CFL1	GGAGGTGAAGAAGCGCAAGA
NT - 1	NT	GCTCGACGGCCGATGTGAT
NT - 2	NT	GGTGCAACACGTCGGTCGA
NT - 3	NT	GGCGTCTATCGTCGATAG
NC - 1	NC	GTGCACCACATTAACATA
NC - 2	NC	GGAATCTAGATATCACT
NC - 3	NC	GGTCATGATGCCACTGGGAG